



**Utrecht University**

**Faculty of Science**  
Department of Physics  
Department of Mathematics

MASTER THESIS

---

# **Bifurcations in Renormalization Group Flows**

## **A case study of $\text{QCD}_4$**

---

Author:

Folkert Kuipers B.Sc.  
Institute for Theoretical Physics  
Mathematical Institute  
Utrecht University

Supervisors:

Dr. Umut Gürsoy  
Institute for Theoretical Physics  
Utrecht University

Prof. Dr. Yuri Kuznetsov  
Mathematical Institute  
Utrecht University

June 29, 2018



---

## Abstract

In this thesis, we show that renormalization group flows generated by the beta functions in a quantum field theory are examples of generic dynamical systems. Using this connection we argue that phase transitions and/or symmetry breaking within renormalization group flows can be represented by bifurcations of the dynamical system. This allows us to apply analytical and numerical methods that have been developed for bifurcation analysis to quantum field theory. We apply these methods to the QCD<sub>4</sub> model with  $N_c$  colors and  $N_f$  flavors, where we add effective four-fermi interaction to account for non-perturbative terms in the beta functions. We start from the Veneziano limit ( $N_c, N_f \rightarrow \infty$ ), where this model has been studied before and continue to the low  $N_c$  regime. We find that the lower edge of the conformal window is given by a saddle-node bifurcation (or fixed point merger) at constant  $N_f/N_c$  for  $N_c \geq 3$ . In addition, we find new fixed points in the model. We discuss their relevance and discuss the possibility of phase transitions within the conformal window. Finally, we add a scalar field to the model and show that in the presence of this scalar field there exist similar phase transitions, but the ratio,  $N_f/N_c$ , where these transitions occur, changes.

---

## Acknowledgements

I would like to express a word of thanks to my supervisors Umut and Yuri for willing to supervise me on this topic and for their support and feedback during the whole process.

Furthermore, I would like to thank the department of physics and the department of mathematics for the many things I've learned during my seven years of study at Utrecht University. I'm grateful to all staff for guiding me through and raising my interest into many topics within physics and mathematics. Moreover, I would like to thank my fellow students for accompanying me on (parts of) this journey, for the many interesting discussions, and for making my studies such a joyful experience.

Finally, I would like to thank my family and friends for their continuous support.

---

# Contents

<b>Definitions and Notational Conventions</b>	<b>5</b>
<b>1 Introduction</b>	<b>6</b>
1.1 A Short Introduction to Quantum Field Theory . . . . .	6
1.1.1 Regularization and Renormalization . . . . .	7
1.2 The Renormalization Group . . . . .	8
1.2.1 Perturbative Renormalization Group . . . . .	9
1.2.2 Exact Renormalization Group . . . . .	10
1.3 A Short Introduction to Dynamical Systems . . . . .	13
1.4 Bifurcation Analysis . . . . .	15
1.5 Bifurcation Analysis of the Renormalization Group Equations . . . . .	18
<b>2 QCD<sub>4</sub></b>	<b>21</b>
2.1 The Beta Functions . . . . .	23
2.2 The Veneziano Limit . . . . .	25
2.3 The Complete Model . . . . .	32
2.4 Scaling Behavior . . . . .	41
2.5 Bifurcation Points . . . . .	42
2.6 Discussion of the Results . . . . .	44
<b>3 QCD<sub>4</sub> with a Scalar Field</b>	<b>46</b>
3.1 The Veneziano Limit . . . . .	47
3.2 The Complete Model . . . . .	50
3.3 Discussion of the Results . . . . .	55
<b>4 Conclusions and Outlook</b>	<b>56</b>
<b>A Feynman Rules for QCD<sub>4</sub> with a Four-Fermi Interaction</b>	<b>58</b>
<b>B Beta Function for the Gauge Vertex</b>	<b>61</b>
<b>C Beta Functions for the Four-Fermi Interactions</b>	<b>63</b>
<b>D Beta Functions in a Model with a Yukawa Coupling</b>	<b>71</b>
<b>Bibliography</b>	<b>74</b>

---

## Definitions and Notational Conventions

- $\mathbb{N}_0 := \mathbb{N} \cup \{0\}$ ,  $\mathbb{R}^+ := (0, \infty)$ ,  $\mathbb{R}_0^+ := [0, \infty)$ .
- We define  $\{a_i\} := \{a_i | i \in A\}$ , where  $A \subset \mathbb{N}$  is some finite set.
- We use the Minkowski metric  $\eta^{\mu\nu}$  with signature  $(- + + +)$ .
- The Hermitian conjugate (conjugate transpose) of a matrix or operator  $A$  is denoted by  
 $A^\dagger := A^* = \bar{A}^T$ .
- The gamma (Dirac) matrices are defined by the anti-commutation relation  
 $\{\gamma^\mu, \gamma^\nu\} = 2\eta^{\mu\nu} I_4$ .
- The fifth gamma matrix is given by  $\gamma_5 := i\gamma^0\gamma^1\gamma^2\gamma^3 = \frac{i}{4!}\epsilon_{\mu\nu\rho\sigma}\gamma^\mu\gamma^\nu\gamma^\rho\gamma^\sigma$ .
- In Feynman notation, we have  $\not{\partial} = \gamma^\mu\partial_\mu$  and  $\not{p} = \gamma^\mu p_\mu$ .
- For a fermion field we define the conjugate by  $\bar{\psi} := \psi^\dagger\gamma^0$ , which makes  $\bar{\psi}\psi$  and  $\bar{\psi}\not{\partial}\psi$  Lorentz invariant.
- The chiral components of a fermion field are denoted by  
 $L := \psi_L := \frac{1-\gamma^5}{2}\psi$  and  $R := \psi_R := \frac{1+\gamma^5}{2}\psi$ .
- The previous definition implies  $\bar{L} = \bar{\psi}_L = \bar{\psi}\frac{1+\gamma^5}{2}$  and  $\bar{R} = \bar{\psi}_R = \bar{\psi}\frac{1-\gamma^5}{2}$ .

---

# 1 Introduction

## 1.1 A Short Introduction to Quantum Field Theory

In this section a few basic concepts from quantum field theory, which will be needed later on, are introduced.<sup>1.1</sup> Quantum field theory is a combination of classical field theory and quantum mechanics. In classical field theory, one no longer considers individual particles and forces acting between them, but instead one uses a vector field to describe the force on a particle, due to its surroundings, at every point in space-time. This vector field can be an average force due to contact forces from other surrounding particles, as is the case in hydrodynamics, or can be the result of forces that don't involve direct contact with other particles, as is the case of electromagnetic and gravitational fields. Given the field theory, one can calculate the trajectories of any particle throughout space-time, if one knows its properties at a specific time.

In quantum mechanics, one no longer treats particles as well defined points with well defined properties, but as states that indicate the probability for having certain properties, such as a specific position or momentum. As a result, the trajectory of a particle through space-time is not a well defined path anymore. One of the key concepts of quantum field theory is the Feynman path integral. In quantum mechanical language the path integral gives the probability that a particle in state  $q_1$  at time  $t_1$  evolves to  $q_2$  at  $t_2$ . In classical mechanics this probability would always be 1, if the trajectory follows from the equations of motion, that can be derived from the classical field theory, or 0, if it doesn't follow. In quantum mechanics, however, a particle can evolve from one state to another in various ways and each state has a given weight. This leads to

$$W(q_2, t_2; q_1, t_1) = \int_{q(t_1)=q_1}^{q(t_2)=q_2} Dq(t) e^{\frac{i}{\hbar} S[q(t)]}. \quad (1.1)$$

Here the integral is taken in a Hilbert space over the functions (or paths)  $q(t)$ , and every path has a 'probability'  $\exp(\frac{i}{\hbar} S[q(t)])$ , where

$$S[q(t)] = \int_{t_1}^{t_2} dt L(q(t), \dot{q}(t), t) \quad (1.2)$$

is the action, which can be expressed as an integral over time of the Lagrangian. For a quantum field theory the states become fields  $\phi(\vec{x}, t)$  and one can write the action as a space time integral over the Lagrangian density.

$$S[\phi(\mathbf{x})] = \int d^4x \mathcal{L}(\phi(\mathbf{x}), \{\partial_\mu \phi(\mathbf{x})\}, \mathbf{x}), \quad (1.3)$$

where  $\mathbf{x}$  is a four-vector. A quantum field theory is defined by its Lagrangian density, which allows to calculate many physical observables. In general, the solution for functional integrals like (1.1) is not known. In fact, the integral is not necessarily a mathematically well defined object.<sup>1.2</sup> In physics, one is still interested in finding a solution of this intuitive object. In order to compute it, one could discretize the path integral and take a continuum limit in the end. However, for a general path integral the result is not necessarily convergent. Therefore, one may expect to calculate finite results, while the actual path integral diverges or the other way around.

---

<sup>1.1</sup>Quantum field theory is a much richer and more complex theory than this section might suggest. This section only serves as a short introduction for later sections.

<sup>1.2</sup>In specific cases one can make the path integral formulation mathematically well defined, but this is not true in general.

---

In the end, one is interested in measurable quantities, and one naturally expects those to be finite. Typical measurable quantities are expectation values and higher momenta of the quantum field. Those moments are often called Green's functions<sup>1,3</sup> and can be calculated using the moment generating functional

$$W[J] = -\ln \left( \int D\phi e^{-(S[\phi] + \int J\phi)} \right), \quad (1.4)$$

where we switched to Euclidean time,  $\tau = it$ . The moments are given by

$$\langle \phi(\mathbf{x}_1), \dots, \phi(\mathbf{x}_n) \rangle = \prod_{i=1}^n \frac{\delta}{\delta J(\mathbf{x}_i)} W(J) \Big|_{J=0} \quad (1.5)$$

or in terms of Fourier transforms

$$\Gamma^{(n)}(\{p_i\}; g) = \langle \phi(\mathbf{p}_1), \dots, \phi(\mathbf{p}_n) \rangle. \quad (1.6)$$

Calculating these moments involves the calculation of path integrals, which can be done by the discretization procedure. In order to keep track of the calculations, one often translates the calculation to a calculation of Feynman diagrams by defining a set of rules, such that there is a one-to-one correspondence between the moments of the quantum field and a set of diagrams.

### 1.1.1 Regularization and Renormalization

When evaluating moments of a quantum field, one often encounters divergent integrals, such as

$$\int_{-\infty}^{\infty} \frac{d^4 p}{(2\pi)^4} \frac{1}{(p^2 + m^2)^\alpha}, \quad (1.7)$$

which is divergent for  $\alpha \geq 1$ . However, since many of the moments should correspond to measurable quantities, one would expect the final answer to be finite<sup>1,4</sup>. Therefore, one has to find a way to make these integrals finite.<sup>1,5</sup> For a large class of quantum field theories, there exist ways to do this for all diagrams that appear in the theory. These quantum field theories are known as renormalizable theories. Theories for which this is not possible are the non-renormalizable theories. Theories where no divergent integrals arise are finite theories.

The first step in making theories containing integrals like (1.9) finite is known as the regularization of the integral. The key concept of regularization of an integral is the introduction of an extra parameter in which the infinities can be absorbed. The integration then yields an expansion in this parameter, and at the end of the calculation one should take the appropriate limit of this control parameter.

There are many other ways for making this regularization method work. The easiest is usually the introduction of a cut-off parameter in the integration boundaries. However, due to the cut-off parameter symmetries that were present in the Lagrangian might disappear, while symmetries often play a crucial role in physical theories. Therefore, other regularization procedures have been invented. One common regularization procedure is known as

---

<sup>1,3</sup>As the name suggests, these moments often correspond to the kernel of a partial differential equation.

<sup>1,4</sup>Not all mathematical possible moments of a QFT have to be measurable. However, the moments that can be related to a physical observable, should be finite.

<sup>1,5</sup>Here, we assume that the divergence is not physical, but the result of a limiting procedure that was used in the definition of the path integral.



dimensional regularization. The idea of dimensional regularization is to make the space-time dimension a control parameter. I.e. instead of considering a 4-dimensional space-time, one can consider a  $d$ -dimensional space-time, perform the integrals and then take the limit  $d \rightarrow 4$ . Using dimensional regularization in combination with analytical continuation one can derive

$$\int_{-\infty}^{\infty} \frac{d^d p}{(2\pi)^4} \frac{1}{(p^2 + m^2)^\alpha} = i\pi^{\frac{d}{2}} \frac{\Gamma(\alpha - \frac{1}{2}d)}{\Gamma(\alpha)} m^{d-2\alpha}, \quad (1.8)$$

where  $\Gamma$  is the Euler Gamma function. If one takes the dimension  $d = 4 + \epsilon$  and  $\alpha = 2$ , one finds

$$\begin{aligned} \int_{-\infty}^{\infty} \frac{d^d p}{(2\pi)^4} \frac{1}{(p^2 + m^2)^\alpha} &= i\pi^2 \mu^\epsilon \frac{\Gamma(-\frac{1}{2}\epsilon)}{\Gamma(2)} \left( \pi \frac{m^2}{\mu^2} \right)^{\frac{\epsilon}{2}} \\ &= -2i\pi^2 \mu^\epsilon \left[ \frac{1}{\epsilon} + \frac{1}{2}\gamma_E + \frac{1}{2} \ln \left( \frac{\pi m^2}{\mu^2} \right) + \mathcal{O}(\epsilon) \right], \end{aligned} \quad (1.9)$$

where we have introduced the parameter  $\mu \in \mathbb{R}^+$  with mass-dimension 1. The regularization procedure has translated the integral into a series in the control parameter  $\epsilon$ . This series still diverges for the limit  $\epsilon \rightarrow 0$ , but the divergence has been ‘quantified’. The remaining divergent terms can be removed by renormalization of the theory.

Renormalization of a theory boils down to adding terms to the Lagrangian that will cancel the divergences. The new terms, also known as counterterms, can be included into the original Lagrangian by replacing the old fields  $\{\phi_i^0\}$  and the coupling constants  $\{g_i^0\}$  with new fields  $\{\phi_i\}$  and coupling constants  $\{g_i\}$  such that

$$\phi_i^0(\{\bar{g}_j\}, \mu, \epsilon) = \sqrt{Z_{\phi_i}(\{\bar{g}_j\}, \mu, \epsilon)} \phi_i, \quad (1.10)$$

$$g_i^0(\{\bar{g}_j\}, \mu, \epsilon) = Z_{g_i}(\{\bar{g}_j\}, \mu, \epsilon) g_i, \quad (1.11)$$

where  $\bar{g}_j = g_j \mu^{-d_{g_j}}$  is the dimensionless coupling constant. The functions  $Z_{\phi_i}(\{\bar{g}_j\}, \mu, \epsilon)$  and  $Z_{g_i}(\{\bar{g}_j\}, \mu, \epsilon)$  are chosen such that all counterterms are included. If this can be done, we call the theory renormalizable.<sup>1.6</sup> These functions can be expanded as Laurent series in  $\epsilon$ . This leads to

$$g_i^0(\{\bar{g}_j\}, \mu, \epsilon) = \mu^{d_{g_i}(\epsilon)} \left( \bar{g}_i + \sum_{\nu} \frac{a_i^{(\nu)}(\{\bar{g}_j\})}{\epsilon^\nu} \right), \quad (1.12)$$

$$Z_{\phi_i}(\{\bar{g}_j\}, \mu, \epsilon) = 1 + \sum_{\nu} \frac{b^{(\nu)}(\{\bar{g}_j\})}{\epsilon^\nu}, \quad (1.13)$$

where  $d_{g_i}(\epsilon)$  is the mass-dimension of the coupling  $g_i$  and where the functions  $a_\nu$  and  $b_\nu$  are determined by the counterterms. Notice that the old coupling constant is written as  $g^0 = g + \delta g$ . We call  $g^0$  the bare coupling constant,  $g$  the physical coupling constant (this is a physical quantity) and  $\delta g$  contains the divergent counterterms.

Green’s functions should always be independent of the renormalization procedure<sup>1.7</sup>, and hence be independent of  $\mu$ . Also, they have to be finite in the limit  $\epsilon \rightarrow 0$ .

## 1.2 The Renormalization Group

Physical quantities in a quantum field theory are usually expressed in terms of a Green’s function. The renormalization group is a tool which is used in quantum field theories to

<sup>1.6</sup>Notice that these functions are not uniquely defined.

<sup>1.7</sup>They’re not necessarily independent of the regularization procedure. Some regularization schemes may introduce new terms, which are known as anomalies.

---

study changes of these Green's functions, when the energy scales of the process change. The renormalization group was first introduced in the context of particle physics by Stueckelberg and Petermann [1]. Later the renormalization group was also used to study critical phenomena in condensed matter by Wilson [2]. Since then it has been the subject of many other studies. In this section the general idea behind the renormalization group will be discussed.

### 1.2.1 Perturbative Renormalization Group

In order to get acquainted with the renormalization group, let us consider a quantum field theory given by the Lagrangian in  $d$  space-time dimensions with bare bosonic field  $\phi_0$  and bare coupling constant  $g_0$ <sup>1.8</sup>

$$\mathcal{L} = -\frac{1}{2}(\partial_\mu\phi_0(\mu))^2 - \frac{1}{k!}g_0\phi_0^k. \quad (1.14)$$

Here, we assume the Lagrangian to be renormalizable.<sup>1.9</sup> Using the path integral formalism, one can calculate the Green's functions,  $\Gamma^{(n)}(\{p_i\}; g)$ , with the external momenta  $\{p_i\}$ . As we saw in the previous section, we can rewrite the bare Lagrangian to a new Lagrangian with renormalized fields  $Z$  and coupling constants  $g$  via  $\phi_0 = \sqrt{Z_\phi(\bar{g}, \mu, \epsilon)}\phi$  and  $g_0 = g_0(\bar{g}, \mu, \epsilon)$ . From now on, we'll suppress the explicit  $\epsilon$  dependence in the following equations. The results may still be  $\epsilon$  dependent, but at the end the limit  $\epsilon \rightarrow 0$  should give a finite answer. One can solve equation (1.12) perturbatively to find  $\bar{g}(g_0, \mu)$ . Using this solution and equation (1.13) one can write down an expression for  $Z_\phi(g_0, \mu)$ , and find

$$\Gamma^{(n)}(\{p_i\}; \bar{g}(g_0, \mu), \mu) = Z_\phi(g_0, \mu)^{-n/2}\Gamma^{(n)}(\{p_i\}; g_0). \quad (1.15)$$

However, this new parametrization should not change the observables of the theory. In other words the Green's function should be independent of  $\mu$ , therefore

$$\mu \frac{d}{d\mu} \left( Z_\phi(g_0, \mu)^{n/2} \Gamma^{(n)}(\{p_i\}; \bar{g}(g_0, \mu), \mu) \right) = 0. \quad (1.16)$$

Hence,

$$\left( \mu \frac{\partial}{\partial \mu} + \beta_g(\bar{g}, \mu) \frac{\partial}{\partial \bar{g}} + \frac{1}{2} n \gamma_\phi(\bar{g}, \mu) \right) \Gamma^{(n)}(\{p_i\}; \bar{g}(g_0, \mu), \mu) = 0, \quad (1.17)$$

where

$$\beta_g(\bar{g}(g_0, \mu), \mu) = \mu \frac{\partial}{\partial \mu} \bar{g}(g_0, \mu), \quad (1.18)$$

$$\gamma_\phi(\bar{g}(g_0, \mu), \mu) = \mu \frac{\partial}{\partial \mu} \ln Z_\phi(g_0, \mu). \quad (1.19)$$

From now on we'll drop the explicit dependence on the bare parameter  $g_0$  in the function  $\bar{g}$  and  $Z_\phi$ , since it can be kept constant. The beta and gamma functions are very much dependent on the exact form of the Lagrangian and follow from the renormalization of the theory. Equation (1.17) is known as the renormalization group equation or Callan-Symanzik equation. Any Green's function, independent of the parametrization of the theory, should obey this equation. Hence, in order to find Green's functions for the Lagrangian, one has to solve this equation. However, this equation doesn't have an easy closed form solution, so one has to rely on other methods to study the solutions of the equation.

---

<sup>1.8</sup>This example can easily be extended to a more general Lagrangian.

<sup>1.9</sup>For this example, that is not necessarily the case, but we can ignore this for now, since it doesn't affect the derivation.

---

Let us now introduce a new dimensionless parameter  $t \in \mathbb{R}$  such that  $\mu = \mu_0 e^t$ , where  $\mu_0$  has mass-dimension 1. The renormalization group equation (1.17) then reduces to

$$\left( \frac{\partial}{\partial t} + \beta_g(\bar{g}(t), \mu(t)) \frac{\partial}{\partial \bar{g}} + \frac{1}{2} n \gamma_\phi(\bar{g}(t), \mu(t)) \right) \Gamma^{(n)}(\{p_i\}; \bar{g}(t), \mu(t)) = 0 \quad (1.20)$$

with

$$\beta_g(\bar{g}(t), \mu(t)) = \frac{\partial}{\partial t} \bar{g}(t). \quad (1.21)$$

Hence,

$$\left( \frac{d}{dt} + \frac{1}{2} n \gamma_\phi(\bar{g}(t), \mu(t)) \right) \Gamma^{(n)}(\{p_i\}; \bar{g}(t), \mu(t)) = 0. \quad (1.22)$$

The solution to this equation is

$$\Gamma^{(n)}(\{p_i\}; \bar{g}(t), \mu(t)) = e^{-\frac{n}{2} \int_0^t \gamma_\phi(\bar{g}(\tau)) d\tau} \Gamma^{(n)}(\{p_i\}; \bar{g}(0), \mu_0), \quad (1.23)$$

$\{p_i\}$  and  $\mu$  are the only dimensional arguments in the Green's function, and all have mass-dimension 1. A scaling of these arguments with a constant  $e^t$  would lead to a scaling of the Green's function with a constant  $e^{d_\Gamma t}$ . Here  $d_\Gamma$  is the mass-dimension of the Green's function. (If the field  $\phi$  has mass dimension  $d_\phi$ , the Green's function would have mass-dimension  $[\Gamma^{(n)}(\{x_i\}; g)] = n d_\phi$  in position space, and  $d_\Gamma := [\Gamma^{(n)}(\{p_i\}; g)] = n(d_\phi - d)$ , in momentum space.) One now finds

$$\begin{aligned} \Gamma^{(n)}(\{p_i\}; \bar{g}(0), \mu_0) &= e^{-d_\Gamma t} \Gamma^{(n)}(\{e^t p_i\}; \bar{g}(0), e^t \mu_0) \\ &= e^{-d_\Gamma t} \Gamma^{(n)}(\{e^t p_i\}; \bar{g}(0), \mu(t)). \end{aligned} \quad (1.24)$$

Hence,

$$\Gamma^{(n)}(\{e^t p_i\}; \bar{g}(0), \mu(t)) = e^{d_\Gamma t + \frac{n}{2} \int_0^t \gamma_\phi(\bar{g}(\tau)) d\tau} \Gamma^{(n)}(\{p_i\}; \bar{g}(t), \mu(t)), \quad (1.25)$$

and since the Green's functions should be independent of  $\mu$

$$\Gamma^{(n)}(\{e^t p_i\}; g) = e^{d_\Gamma t + \frac{n}{2} \int_0^t \gamma_\phi(\bar{g}(\tau)) d\tau} \Gamma^{(n)}(\{p_i\}; g(t)). \quad (1.26)$$

Given the Green's function, the coupling  $g$  and external momenta  $\{p_i\}$ , one can thus find the Green's function at another energy scale  $\{e^t p_i\}$  by evaluating the Green's function for another coupling  $\bar{g}(t)$  satisfying (1.21), such that  $\bar{g}(0) = \bar{g}$  and multiplying it with a constant  $\exp(d_\Gamma t + \frac{n}{2} \int_0^t \gamma_\phi(\bar{g}(\tau)) d\tau)$ . This expression still involves an integral over the function  $\gamma(\tau)$ , which is easier to solve than the path integral for the Green's function.

It is an easy task to generalize this argument to a theory with multiple coupling constants or multiple bosonic or fermionic fields, since one can replace all coupling constants by a set of coupling constants  $\{g_\alpha\}$  and a set of fields  $\{\phi_i\}$ . The derivation is then the same except for the fact that every coupling constant will give rise to a  $\beta_\alpha$  function and every field give rise to a renormalization factor  $Z_{\phi_i}$ .

### 1.2.2 Exact Renormalization Group

In the previous subsection, it was shown how the calculation of counterterms gives rise to beta functions. The beta functions describe the change of coupling constants when the energy scale of a theory changes. Wilson [3] used this latter idea to find an exact equation for the change of a theory with its energy scale. This led to the derivation of a new renormalization group equation, which is known as the exact renormalization group. Since

---

its introduction various variations have been constructed. The exact renormalization group leads to an exact equation for the beta functions. The most common examples are the Polchinski and the Wetterich equation [4]. Although the exact renormalization group theory uses exact equations, the method is still dependent on approximations. In this section, we derive the Wetterich equation for the effective action, since it will be used later on to calculate beta functions in QCD<sub>4</sub>. Here, we do the derivation for the case of a single scalar field, which can be extended to more complicated models with several fields. The presented derivation is largely based on [4] and [5].

The moment generating functional for the Greens functions is given by

$$e^{-W[J]} = \int D\chi e^{-(S[\chi]+f J\chi)}, \quad (1.27)$$

where all fields are taken as a function of momentum, and the integral in the exponent is an integral over all possible momenta  $q$ . Its Legendre transform is given by<sup>1,10</sup>

$$\tilde{\Gamma}[\phi] = W[J] - \int J\phi, \quad (1.28)$$

where  $\phi = \frac{\delta W}{\delta J} = \langle \chi \rangle$  is the expectation value (or first moment) of the field. This theory may contain divergences in the UV or IR (high or low energy) limit. One can get rid of these divergences by integrating a cutoff function  $\mathcal{R}_\Lambda(q^2)$  in the momentum integrals, such that the high and/or low momenta are suppressed. Here,  $\Lambda = \|\Lambda\| \in \mathbb{R}_{\geq 0}$  is a cutoff momentum. This yields a  $\Lambda$  dependent generating functional

$$e^{-W_\Lambda[J]} = \int D\chi e^{-(S[\chi]+\Delta S_\Lambda[\chi]+f J\chi)}, \quad (1.29)$$

where

$$\Delta S_\Lambda[\chi] = \frac{1}{2} \int \frac{d^d q}{(2\pi)^d} \chi(-q) \mathcal{R}_\Lambda(q^2) \chi(q). \quad (1.30)$$

$\mathcal{R}_\Lambda$  is a real and positive distribution or function depending on a cutoff momentum  $\Lambda$  that regulates the integral and satisfies:

$$\begin{cases} \lim_{\Lambda \rightarrow 0} \mathcal{R}_\Lambda(q^2) = 0, \\ \lim_{\Lambda \rightarrow \infty} \mathcal{R}_\Lambda(q^2) = \infty, \\ \Lambda \frac{\partial}{\partial \Lambda} \mathcal{R}_\Lambda(q^2) = 0, \text{ for } q^2 \ll \Lambda^2 \text{ and } q^2 \gg \Lambda^2, \end{cases}$$

where the last convergence has to go faster than any polynomial.

One can define the Legendre transform of  $W_\Lambda$  by

$$\tilde{\Gamma}_\Lambda[\phi] = W_\Lambda[J] - \int d^d q J\phi, \quad (1.31)$$

where  $J = J[\phi]$ ,  $\phi = \frac{\delta W_\Lambda}{\delta J} = \langle \chi \rangle$ , and the average is taken with respect to the new  $\Lambda$ -dependent measure. We define the effective average action by

$$\Gamma_\Lambda[\phi] \equiv \tilde{\Gamma}_\Lambda[\phi] - \Delta S_\Lambda[\phi], \quad (1.32)$$

and we introduce the new dimensionless variable,  $t$ , such that  $\frac{d}{dt} = -\Lambda \frac{d}{d\Lambda}$ . One then finds

$$\frac{dW_\Lambda[J]}{dt} = \frac{d}{dt} \langle \Delta S_\Lambda[\chi] \rangle = \frac{1}{2} \int \frac{d^d q}{(2\pi)^d} \langle \chi\chi \rangle \frac{d\mathcal{R}_\Lambda}{dt}. \quad (1.33)$$

---

<sup>1,10</sup>We assume  $W$  and  $\Gamma$  to be differentiable functionals.

---

Using the definition of the average effective action (1.32), one finds

$$\begin{aligned}
\frac{d\Gamma_\Lambda[\phi]}{dt} &= \frac{dW_\Lambda[J]}{dt} - \frac{d\Delta S_\Lambda[\phi]}{dt} \\
&= \frac{1}{2} \int \frac{d^d q}{(2\pi)^d} (\langle \chi \chi \rangle - \langle \chi \rangle \langle \chi \rangle) \frac{d\mathcal{R}_\Lambda}{dt} \\
&= -\frac{1}{2} \text{Tr} \left[ \frac{\delta^2 W_\Lambda}{\delta J \delta J} \frac{d\mathcal{R}_\Lambda}{dt} \right], \tag{1.34}
\end{aligned}$$

where we have used  $\phi = \langle \chi \rangle$  and written the momentum integral  $\int \frac{d^d q}{(2\pi)^d}$  as a trace. Notice

$$\frac{\delta^2 W_\Lambda}{\delta J \delta J} = \frac{\delta \phi}{\delta J} = \left( \frac{\delta J}{\delta \phi} \right)^{-1} = - \left( \frac{\delta^2 \tilde{\Gamma}}{\delta \phi \delta \phi} \right)^{-1}. \tag{1.35}$$

Hence,

$$\begin{aligned}
\frac{d\Gamma_\Lambda[\phi]}{dt} &= \frac{1}{2} \text{Tr} \left[ \left( \frac{\delta^2 \tilde{\Gamma}_\Lambda}{\delta \phi \delta \phi} \right)^{-1} \frac{d\mathcal{R}_\Lambda}{dt} \right] \\
&= \frac{1}{2} \text{Tr} \left[ \left( \frac{\delta^2 \Gamma_\Lambda}{\delta \phi \delta \phi} + \frac{\delta^2 \Delta S_\Lambda}{\delta \phi \delta \phi} \right)^{-1} \frac{d\mathcal{R}_\Lambda}{dt} \right] \\
&= \frac{1}{2} \text{Tr} \left[ \left( \frac{\delta^2 \Gamma_\Lambda}{\delta \phi \delta \phi} + \mathcal{R}_\Lambda \right)^{-1} \frac{d\mathcal{R}_\Lambda}{dt} \right]. \tag{1.36}
\end{aligned}$$

This last equation is known as the Wetterich equation. The Wetterich equation is an exact equation for the flow of the average effective action when the energy scale changes, and was first derived by Wetterich [6]. The effective average action,  $\tilde{\Gamma}_\Lambda[\phi]$ , flows between the classical action  $S[\phi]$  at  $t \rightarrow -\infty$  (UV limit) and the effective action  $\Gamma[\phi]$  for  $t \rightarrow +\infty$  (IR limit). The classical action describes the fundamental particles and forces of the system, while the effective action describes the particles and forces as they appear at lower energies, which may differ from the fundamental particles defined at high energies.

One can expand the average effective action as

$$\Gamma_\Lambda[\phi] = \sum_{n=1}^{\infty} g_n(\Lambda) \mathcal{O}_n(\phi), \tag{1.37}$$

where  $\mathcal{O}_n(\phi) = \mathcal{O}_n(\phi, \{\partial_\mu \phi\})$  are polynomial functionals of the fields  $\phi$  and its space-time derivatives, and  $d_{g_n}$  is the dimension of the coupling constant  $g_n$ . This expansion leads to

$$\frac{d}{dt} \Gamma_\Lambda[\phi] = \sum_{n=1}^{\infty} \beta_{g_n}(t) \mathcal{O}_n(\phi), \tag{1.38}$$

so the beta functions now define a flow in an infinite space of coupling constants, known as theory space, and can be read off from the Wetterich equation by expanding the trace in eq. (1.36) in terms of the 1-particle irreducible diagrams. Only certain orbits in theory space will represent the true physical theory. It's expected, that a physical theory has finite coupling constants, so physical theories are usually represented by bounded trajectories. Typically, these bounded orbits are trajectories connecting two fixed points, which represent conformal theories (theories that are invariant under conformal maps). The linearization at the fixed points yields a set of eigenvalues and eigenvectors. The direction with negative eigenvalue

---

correspond to irrelevant operators, the eigenvectors with 0 eigenvalue to marginal operators and the ones with positive eigenvalue to relevant directions. The eigenvalues themselves are the scaling dimensions of the operators. The flow of the renormalized trajectory goes from the UV limit to the IR limit along a relevant direction, and the coupling constants at a certain energy scale are determined by the renormalized trajectory.

Both the perturbative and the exact renormalization group method induce beta functions, which define the renormalization group flow. However, the approaches are different: the perturbative renormalization group method starts from the bare action, which has a finite set of coupling constants and beta functions. However, the beta functions can only be calculated perturbatively. In the limit of infinite order in perturbation, one would obtain the ‘true’ renormalization group functions. The exact renormalization group, on the other hand, starts from the effective action, which contains an infinite set of coupling constants and an infinite set of beta functions, although only a subset of these functions is physically relevant. The beta functions can be calculated exactly and the approximation is made by truncating the higher order interactions. Only when one would consider all possible interactions the ‘true’ renormalization group can be found.

### 1.3 A Short Introduction to Dynamical Systems

This section presents a short overview of relevant terminology in the field of dynamical systems. There exist many more complete introductions, such as [7], into the topic. A *dynamical system* is a tuple  $(T, X, \Phi)$ , where  $X$  is a non-empty set,  $\Phi : X \rightarrow X$  a function defined on this set and either  $T = \mathbb{N}_0$ , in which case we talk about a *discrete dynamical system* or  $T = \mathbb{R}_0^+$ , in the case of a *continuous dynamical system*. When the map  $\Phi$  is invertible, it is natural to extend  $T$  to  $T = \mathbb{Z}$  or  $T = \mathbb{R}$ . Depending on the properties that one wants to study, one often assumes the set  $X$  to have some extra structure that is preserved by the map  $\Phi$ . The tuple  $(X, \Phi)$  could for example be a measurable space with measure preserving map, metric space with an isometry, a topological space with continuous map, or a differentiable manifold with differentiable map. For a point  $x \in X$ , one can define the *orbit*  $\mathcal{O}_\Phi(x) := \{\Phi^t(x) | t \in T\}$ . For an invertible dynamical system one can split this orbit in the *positive semi-orbit*  $\mathcal{O}_\Phi^+(x) := \{\Phi^t(x) | t \in T_0^+\}$  and the *negative semi-orbit*  $\mathcal{O}_\Phi^-(x) := \{\Phi^t(x) | t \in T_0^-\}$ . The collection of all maps  $\{\Phi^t\}_{t \in T}$  is called the *flow* of the dynamical system with time parameter  $t$  and should satisfy

- $\Phi^0 = \text{Id}$
- $\Phi^{s+t}(x) = \Phi^s(\Phi^t(x)), \forall x \in X, s, t \in T$ .

Therefore, the flow forms a group, if  $\Phi$  is invertible, and a semi-group otherwise. Furthermore, one can define the notion of an invariant set of a dynamical system

**Definition.** *Given a dynamical system  $(T, X, \Phi)$ , a forward invariant set is a set  $U \subset X$  such that  $\Phi^t(U) \subseteq U \forall t \geq 0$ ;  
a backward invariant set is a set  $U \subset X$  such that  $\Phi^t(U) \subseteq U \forall t \leq 0$ ;  
a set that is both forward and backward invariant is called an invariant set of the dynamical system.*

If the map  $\Phi^t$  is non-invertible and  $T$  is only defined on positive numbers, every forward invariant set is called an invariant set of the dynamical system.

The most natural way to generate a dynamical system is by a set of ordinary differential equations (continuous-time dynamical system) or a set of difference equations (discrete-time

dynamical system). In this thesis, we consider dynamical systems generated by a set of differential equations, since those can be related to the beta functions of the renormalization group. Given the space  $X = \mathbb{R}^n$ , one can consider the system of autonomous ordinary differential equations

$$\dot{x} = f(x), \quad (1.39)$$

where  $x \in \mathbb{R}^n$  and  $f : \mathbb{R}^n \rightarrow \mathbb{R}^n$ , which is assumed to be (sufficiently) smooth. If one defines the map  $\Phi^t : \mathbb{R}^n \rightarrow \mathbb{R}^n$  s.t.  $\Phi^t(x_0) = x(t, x_0)$ , then the tuple  $(\mathbb{R}, \mathbb{R}^n, \Phi)$  is a continuous-time dynamical system. The solutions for specified initial conditions,  $x(0, x_0) = x_0$ , define the orbits and the visualization of the flow will be called the *phase portrait*. The topology of the phase portrait is characterized by its invariant sets and their stability.

**Definition.** Given a dynamical system  $(\mathbb{R}, X, \Phi)$ , a point  $x \in X$  and an orbit  $\mathcal{O}(x)$ , a point  $y$  is an  $\omega$ -limit point of  $x$ , if there exists a sequence  $\{t_n | n \in \mathbb{N}\} \subset \mathbb{R}$  s.t.

$$\lim_{n \rightarrow \infty} t_n = \infty$$

$$\lim_{n \rightarrow \infty} \Phi(t_n, x) = y;$$

and an  $\alpha$ -limit point of  $x$ , if there exists a sequence  $\{t_n | n \in \mathbb{N}\} \subset \mathbb{R}$  s.t.

$$\lim_{n \rightarrow \infty} t_n = -\infty$$

$$\lim_{n \rightarrow \infty} \Phi(t_n, x) = y;$$

The set of all  $\omega$ -limit points ( $\alpha$ -limit points) is the  $\omega$ -limit set ( $\alpha$ -limit set) of  $x$ .

Typical examples of limit sets are equilibria<sup>1,11</sup>, periodic orbits and chaotic attractors. Limit sets can be stable or unstable. A limit set is asymptotically stable, if all orbits starting in a neighborhood of the limit set stay in this neighborhood and converge towards the limit set if  $t \rightarrow \infty$  and unstable otherwise. For generic equilibria the stability is determined by the eigenvalues of Jacobian matrix at the equilibrium. At the equilibrium, one can define the notions of a stable, unstable and critical eigenspace.

**Definition.** Given a continuous-time dynamical system defined by equation (1.39), with an equilibrium point at  $x_0 \in \mathbb{R}^n$ . Let  $A$  be the Jacobian matrix of  $f$  at  $(x_0)$ ,  $\lambda_1, \lambda_2, \dots, \lambda_n$  its eigenvalues and  $\eta_1, \eta_2, \dots, \eta_n$  the corresponding (generalized) eigenvectors.

Then the stable eigenspace is given by  $T^s = \text{span}\{\eta_1^-, \eta_2^-, \dots, \eta_{n_-}^-\}$ ;

the unstable eigenspace by  $T^u = \text{span}\{\eta_1^+, \eta_2^+, \dots, \eta_{n_+}^+\}$

and the critical eigenspace by  $T^c = \text{span}\{\eta_1^c, \eta_2^c, \dots, \eta_{n_c}^c\}$ ,

where  $\eta_i^+$  label (generalized) eigenvectors that correspond to eigenvalues  $\lambda_i^+$  with positive real part,  $\eta_i^-$  (generalized) eigenvectors corresponding to eigenvalues  $\lambda_i^-$  with negative real part and  $\eta_i^c$  (generalized) eigenvectors corresponding to eigenvalues  $\lambda_i^c$  with zero real part.

Furthermore,  $n_+ + n_- + n_c = n$ .

For a discrete-time dynamical system one can define similar notions, but then stable eigenvalues have  $|\lambda_i| < 1$ , unstable eigenvalues have  $|\lambda_i| > 1$  and critical eigenvalues have  $|\lambda_i| = 1$ . An equilibrium is called *hyperbolic* if  $\dim(T^c) = 0$ , *stable* if  $\dim(T^s) = n$  and *unstable* if  $\dim(T^u) \geq 1$ . Furthermore, an equilibrium with  $\dim(T^s) = n$  or  $\dim(T^u) = n$  is a *node* and an equilibrium with  $\dim(T^s) \geq 1$  and  $\dim(T^u) \geq 1$  is a *saddle*. The classification of non-hyperbolic equilibria not satisfying these conditions is more involved, and won't be discussed further in this section. For a generic equilibrium in a continuous-time dynamical system, one can define the notions of a stable and unstable manifold of the equilibrium.

**Definition.** Given a continuous-time dynamical system  $(\mathbb{R}, X, \Phi)$ , and an equilibrium point  $x \in X$  of  $\Phi$ , then the stable manifold of  $x$  is defined as

<sup>1,11</sup>In the remainder of this thesis, we'll often use the term fixed point instead of equilibrium to adapt to the terminology used in renormalization group theory, while in the terminology of dynamical systems the term fixed point is reserved for the discrete analogue of an equilibrium.

---

$W^s(\Phi, x) = \{y \in X : \lim_{t \rightarrow \infty} \phi^t(y) = x\}$   
 and the unstable manifold as  
 $W^u(\Phi, x) = \{y \in X : \lim_{t \rightarrow -\infty} \phi^t(y) = x\}.$

For a dynamical system defined by (1.39), the stable manifold is at the equilibrium tangent to the stable eigenspace, while the unstable manifold is at the equilibrium tangent to the unstable eigenspace. For non hyperbolic equilibria, one can introduce the concept of a center manifold  $W_{\text{loc}}^c(\Phi, x)$ , which is  $n_c$ -dimensional and tangent to the critical eigenspace at the equilibrium. The existence of this locally defined manifold is implied by the Center Manifold Theorem.

As a final remark, we notice that the stability of limit cycles in a continuous-time dynamical system can be categorized in a similar way by studying the Poincaré map associated with the cycle. The Poincaré map defines a  $(n - 1)$ -dimensional discrete-time dynamical system.

## 1.4 Bifurcation Analysis

A continuous-time dynamical system defined by a set of ordinary differential equations can be analyzed by solving the ODE's numerically. However, if the differential equations also depend on a set of parameters,  $f_\alpha(x)$ ,  $\alpha \in \mathbb{R}^m$ , one is often not interested in the exact solutions for specific values of  $\alpha$ , but in the topological properties of the phase portrait such as the number of equilibria, limit cycles and their stability or the existence of chaotic attractors. In general, changes of the phase portrait, when  $\alpha$  is varied occur smoothly except for some specific values of  $\alpha$ , where the topology of the phase portrait changes. Changes in the topology of the phase portrait are called bifurcations. Topology changes often occur near or within invariant sets. Bifurcations can be divided in 2 subclasses:

- local bifurcations: bifurcations that can be detected by considering small but non-shrinking neighborhoods of equilibria or limit cycles.
- global bifurcations: bifurcations that cannot be detected in this way. Topology changes typically involve multiple invariant sets.

In addition, bifurcations may be called subcritical or supercritical, depending on the stability of the equilibria or limit cycles that appear or disappear at the bifurcation. Furthermore, bifurcations can be characterized by their codimension. The codimension of a bifurcation in a generic system is given by the number of independent conditions that have to be satisfied for a bifurcation to happen, and is also related to the number of critical eigenvalues of the Jacobian matrix at the equilibrium. Consequently, the codimension of a bifurcation is always smaller or equal to the dimension of the parameter space. In general, many types of bifurcations can be found. For an overview of possible bifurcations and their conditions, we refer to [9]. In this section, we discuss bifurcations and related terminology that is relevant for subsequent chapters. In doing so, we closely follow [9]. Bifurcations in low dimensional systems and with low codimension can often be found using analytical techniques, but for higher dimensional systems and in particular for higher codimension of the bifurcation one often has to rely on numerical techniques. Multiple programs have been developed for bifurcation analysis. In this thesis we make use of the Matlab package Matcont [10]. Bifurcation software relies on the conditions that have to be satisfied in order for a bifurcation to happen.

In different dynamical systems one can expect different bifurcations, which are not immediately defined by the same conditions. However, one would like to have a way of categorizing bifurcation in various systems. For this, we need the notion of *topological equivalence*. Con-



sider two continuous-time dynamical systems:

$$\dot{x} = f(x, \alpha), \quad x \in \mathbb{R}^n, \alpha \in \mathbb{R}^m; \quad (1.40)$$

$$\dot{y} = g(y, \beta), \quad y \in \mathbb{R}^n, \beta \in \mathbb{R}^m. \quad (1.41)$$

**Definition.** *Dynamical systems (1.40) and (1.41) are topologically equivalent if*  
 (i) *there exists a homeomorphism of the parameter space  $p: \mathbb{R}^m \rightarrow \mathbb{R}^m$  s.t.  $\beta = p(\alpha)$ ;*  
 (ii) *there exists a parameter-dependent homeomorphism of the phase space  $h_\alpha: \mathbb{R}^n \rightarrow \mathbb{R}^n$  s.t.  $y = h_\alpha(x)$ , mapping orbits of the system (1.40) at parameter values  $\alpha$  onto orbits of the system (1.41) at parameter values  $\beta = p(\alpha)$ , preserving the direction of time.*

Since many bifurcations are locally defined, one is often only interested in *local topological equivalence* near specific points.

**Definition.** *Dynamical systems (1.40) and (1.41) are locally topologically equivalent near the origin, if there exists a map  $(x, \alpha) \mapsto (h_\alpha(x), p(\alpha))$ , defined in a small neighborhood of  $(x, \alpha) = (0, 0) \in \mathbb{R}^n \times \mathbb{R}^m$  such that*

(i)  *$p: \mathbb{R}^m \rightarrow \mathbb{R}^m$  is a homeomorphism defined in a small neighbourhood of  $\alpha = 0$ ,  $p(0) = 0$ ;*

(ii)  *$h_\alpha: \mathbb{R}^n \rightarrow \mathbb{R}^n$  is a parameter-dependent homeomorphism defined in a small neighborhood  $U_\alpha$  of  $x = 0$ ,  $h_0(0) = 0$ , and mapping orbits of the system (1.40) in  $U_\alpha$  onto orbits of the system (1.41) in  $h_\alpha(U_\alpha)$ , preserving the direction of time.*

By coordinate translations one can easily generalize this definition to local topological equivalence in arbitrary points. Having these definitions, one can categorize bifurcations by topological equivalence to normal forms. Consider a polynomial in  $z_i$  for a continuous-time dynamical system

$$\dot{z} = g(z, \beta; \sigma), \quad z \in \mathbb{R}^n, \beta \in \mathbb{R}^k, \sigma \in \mathbb{R}^l, \quad (1.42)$$

which has an equilibrium  $z = 0$  at  $\beta = 0$ , satisfying  $k$  bifurcation conditions. Here,  $\sigma$  is a vector of the coefficients of the polynomial  $g(z, \beta; \sigma)$ .

**Definition.** *System (1.42) is a topological normal form for the bifurcation if any generic system (1.40) with equilibrium  $x_0$  satisfying the bifurcation conditions  $\alpha_0$  is locally topologically equivalent near  $(x_0, \alpha_0)$  to (1.42) for some values of the coefficients  $\sigma_i$ .*

We notice that the system (1.40) can have higher dimension than is needed for the bifurcation to occur:  $x \in \mathbb{R}^n$ , while the normal form has  $z^c \in \mathbb{R}^{n_c}$  with  $n_c < n$ . In such a case, there is a continuation of the critical center manifold. For nearby parameter values (1.40) is locally topologically equivalent to

$$\dot{z}^c = g(z^c, \beta; \sigma), \quad (1.43)$$

$$\dot{z}^s = -z^s, \quad (1.44)$$

$$\dot{z}^u = +z^u, \quad (1.45)$$

where  $g(z^c, \beta; \sigma)$  is the generic normal form on the center manifold and  $z^s \in \mathbb{R}^{n_s}$ ,  $z^u \in \mathbb{R}^{n_u}$  correspond to the stable and unstable directions.

We now give a short discussion of bifurcations that will be encountered in later sections.

### Saddle-Node Bifurcation

A saddle-node bifurcation (figure 1.1) is a codimension one bifurcation at which two equilibria collide and disappear, and is also known as fold or limit point bifurcation. The bifurcation occurs at  $(\bar{x}, \bar{\alpha})$ , if the following conditions hold for the system (1.40):

- 
- $f(\bar{x}, \bar{\alpha}) = 0$
  - $f_x(\bar{x}, \bar{\alpha}) = 0$ ,
  - $a = \frac{1}{2}f_{xx}(\bar{x}, \bar{\alpha}) \neq 0$ ,
  - $f_\alpha(\bar{x}, \bar{\alpha}) \neq 0$ ,

where  $a$  is the quadratic coefficient of the system (1.40). The system is then locally topologically equivalent near  $(\bar{x}, \bar{\alpha})$  to the normal form given by

$$\dot{\tilde{x}} = \tilde{\alpha} \pm \tilde{x}^2, \quad \tilde{x}, \tilde{\alpha} \in \mathbb{R}, \quad (1.46)$$

where  $\tilde{x} = x - \bar{x}$  and  $\tilde{\alpha} = \alpha - \bar{\alpha}$ .

### Adronov-Hopf Bifurcation

An Adronov-Hopf or Hopf bifurcation figure (1.2) is a codimension one bifurcation, and indicates the birth of a limit cycle. The bifurcation occurs at an equilibrium  $(\bar{x}, \bar{\alpha})$ , if a pair of two conjugate complex eigenvalues of the Jacobian matrix crosses the imaginary axis. Generically, at the Hopf bifurcation the system is locally topologically equivalent near  $(\bar{x}, \bar{\alpha})$  to the normal form given by

$$\begin{aligned} \dot{\tilde{x}}_1 &= \tilde{\alpha}\tilde{x}_1 - \tilde{x}_2 \pm \tilde{x}_1(\tilde{x}_1^2 + \tilde{x}_2^2), \\ \dot{\tilde{x}}_2 &= \tilde{x}_1 + \tilde{\alpha}\tilde{x}_2 \pm \tilde{x}_2(\tilde{x}_1^2 + \tilde{x}_2^2) \quad \tilde{x}_1, \tilde{x}_2, \tilde{\alpha} \in \mathbb{R}, \end{aligned} \quad (1.47)$$

where  $\tilde{x} = x - \bar{x}$  and  $\tilde{\alpha} = \alpha - \bar{\alpha}$ . The plus sign corresponds to the subcritical case, where an unstable limit cycles is created and the minus sign to the supercritical case, where a stable limit cycle is created.

### Transcritical Bifurcation

A Transcritical bifurcation (figure 1.3) is a codimension one bifurcation in the class of systems that always have a trivial equilibrium, and is also called branching point bifurcation. At the bifurcation, two equilibria collide and exchange their stability. The bifurcation occurs at  $(\bar{x}, \bar{\alpha})$ , if the following conditions hold for the system (1.40):

- $f(\bar{x}, \bar{\alpha}) = 0$
- $f_x(\bar{x}, \bar{\alpha}) = f_\alpha(\bar{x}, \bar{\alpha}) = 0$ ,
- $f_{xx}(\bar{x}, \bar{\alpha}) \neq 0, f_{x\alpha}(\bar{x}, \bar{\alpha}) \neq 0$ .

The system is then locally topologically equivalent near  $(\bar{x}, \bar{\alpha})$  to the normal form given by

$$\dot{\tilde{x}} = \tilde{\alpha}\tilde{x} \pm \tilde{x}^2, \quad \tilde{x}, \tilde{\alpha} \in \mathbb{R}, \quad (1.48)$$

where  $\tilde{x} = x - \bar{x}$  and  $\tilde{\alpha} = \alpha - \bar{\alpha}$ . Notice that we can transform the normal form of the transcritical bifurcation to the normal form of the saddle-node bifurcation by the non-invertible coordinate transformation

$$(\tilde{x}, \tilde{\alpha}) \rightarrow (\tilde{x}', \tilde{\alpha}') = \left( \tilde{x} \pm \frac{\tilde{\alpha}}{2}, \mp \frac{\tilde{\alpha}^2}{4} \right).$$

This is called a nonversal unfolding of the saddle-node bifurcation.

### Pitchfork Bifurcation

A pitchfork bifurcation (figure 1.4) is a codimension one bifurcation for systems with reflectional symmetry, and is also a branching point bifurcation. At the bifurcation one equilibrium splits into three equilibria. The bifurcation occurs at  $(\bar{x}, \bar{\alpha})$ , if the following conditions hold for the system (1.40):

- 
- $f(\bar{x}, \bar{\alpha}) = 0$
  - $f_x(\bar{x}, \bar{\alpha}) = f_{xx}(\bar{x}, \bar{\alpha}) = f_\alpha(\bar{x}, \bar{\alpha}) = 0$ ,
  - $f_{xxx}(\bar{x}, \bar{\alpha}), f_{x\alpha}(\bar{x}, \bar{\alpha}) \neq 0$ .

The system is then locally topologically equivalent near  $(\bar{x}, \bar{\alpha})$  to the normal form given by

$$\dot{\tilde{x}} = \tilde{\alpha}\tilde{x} \pm \tilde{x}^3, \quad \tilde{x}, \tilde{\alpha} \in \mathbb{R}, \quad (1.49)$$

where  $\tilde{x} = x - \bar{x}$  and  $\tilde{\alpha} = \alpha - \bar{\alpha}$ . The  $-$  sign gives the supercritical case where a stable equilibrium splits into two stable equilibria and an unstable equilibrium, and the  $+$  sign is the subcritical case, where an unstable equilibrium splits into two unstable equilibria and a stable equilibrium.

### Cusp Bifurcation

A cusp bifurcation (figure 1.5) is a codimension two bifurcation in generic systems, where two branches of saddle-node bifurcation meet tangentially. Nearby the system can have three equilibria which collide and disappear at the saddle-node bifurcations. The bifurcation occurs at  $(\bar{x}, \bar{\alpha})$ , if the following nondegeneracy conditions hold for the system (1.40):

- $c = \frac{1}{6}f_{xxx}(\bar{x}, \bar{\alpha}) \neq 0$ ,
- the map  $(x, \alpha) \mapsto (f(x, \alpha), f_x(x, \alpha), f_{xx}(x, \alpha))$  is regular at  $(x, \alpha) = (\bar{x}, \bar{\alpha})$ ,

where  $c$  is the cubic coefficient of the system (1.40). The system is then locally topologically equivalent near  $(\bar{x}, \bar{\alpha})$  to the normal form given by

$$\dot{\tilde{x}} = \tilde{\alpha}_1 + \tilde{\alpha}_2\tilde{x} \pm \tilde{x}^3, \quad \tilde{x}, \tilde{\alpha}_1, \tilde{\alpha}_2 \in \mathbb{R}, \quad (1.50)$$

where  $\tilde{x} = x - \bar{x}$  and  $\tilde{\alpha} = \alpha - \bar{\alpha}$ .

### Saddle-Node-Transcritical Bifurcation

A Saddle-Node-Transcritical bifurcation (figure 1.6) [11] is a codimension two bifurcation, where two branches of a transcritical bifurcation curve meet on a saddle-node bifurcation curve. There exist two cases of this bifurcation. One can be seen as the unfolding of a Cusp bifurcation, while the second can be obtained as an unfolding of a degenerate Bogdanov-Takens bifurcation. Here, we discuss the first case. Nearby the system can have three equilibria (a,b,c) one pair (a,b) has a transcritical bifurcation at one of the branches and another pair (a,c) has a transcritical bifurcation at another branch. The last possible pair (b,c) collides and disappears at the saddle-node bifurcation curve. The bifurcation occurs at  $(\bar{x}, \bar{\alpha})$ , the system is then locally topologically equivalent near  $(\bar{x}, \bar{\alpha})$  to the normal form given by

$$\dot{\tilde{x}} = \tilde{\alpha}_1\tilde{x} + \tilde{\alpha}_2\tilde{x}^2 \pm \tilde{x}^3, \quad \tilde{x}, \tilde{\alpha}_1, \tilde{\alpha}_2 \in \mathbb{R}, \quad (1.51)$$

where  $\tilde{x} = x - \bar{x}$  and  $\tilde{\alpha} = \alpha - \bar{\alpha}$ . We then find a transcritical bifurcation along the line  $\tilde{\alpha}_1 = 0$ , and a saddle-node bifurcation along  $\tilde{\alpha}_1 = \pm \frac{\tilde{\alpha}_2^2}{4}$ . The normal form can be transformed to the normal form of the cusp bifurcation through the transformation

$$(\tilde{x}, \tilde{\alpha}_1, \tilde{\alpha}_2) \rightarrow (\tilde{x}', \tilde{\alpha}'_1, \tilde{\alpha}'_2) = \left( \tilde{x} \pm \frac{\tilde{\alpha}_2}{3}, \frac{2\tilde{\alpha}_2^3}{27} \mp \frac{\tilde{\alpha}_1\tilde{\alpha}_2}{3}, \tilde{\alpha}_1 \mp \frac{\tilde{\alpha}_2^2}{3} \right).$$

## 1.5 Bifurcation Analysis of the Renormalization Group Equations

The beta functions as defined in equations (1.18) and (1.38) define a system of differential equations in the space of coupling constants  $\{g_i\}$ , which is known as theory space  $\mathcal{T}$ . Both

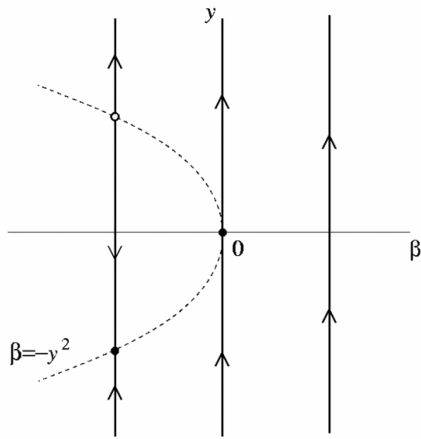


Figure 1.1: Saddle-Node bifurcation in the system  $\dot{y} = \beta + y^2$  [12].

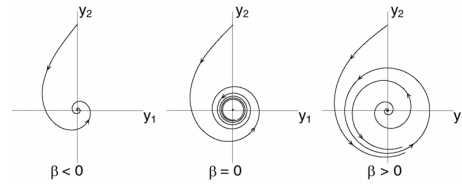


Figure 1.2: Supercritical Andronov-Hopf bifurcation in the system  $\dot{y}_1 = \beta y_1 - y_2 - y_1(y_1^2 + y_2^2)$ ,  $\dot{y}_2 = y_1 + \beta y_2 - y_2(y_1^2 + y_2^2)$  [13].

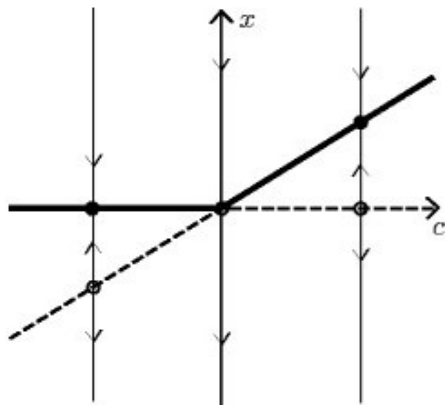


Figure 1.3: Transcritical bifurcation in the system  $\dot{x} = cx - x^2$  [14].

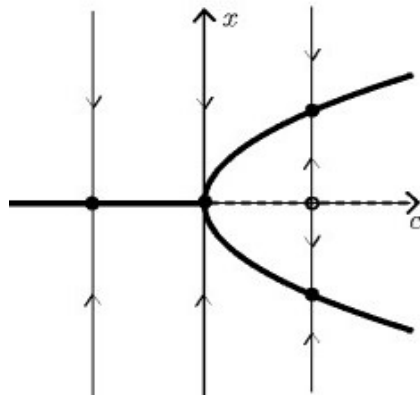


Figure 1.4: Supercritical pitchfork bifurcation in the system  $\dot{x} = cx - x^3$  [14].

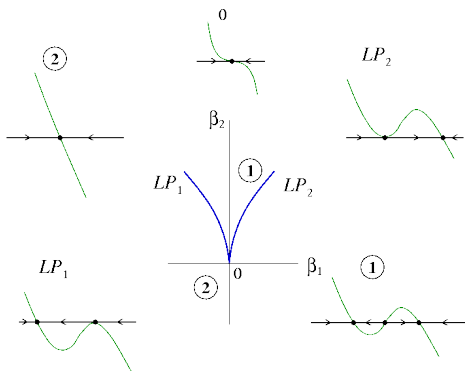


Figure 1.5: Cusp bifurcation in the system  $\dot{y} = \beta_1 + \beta_2 y - y^3$  [15].

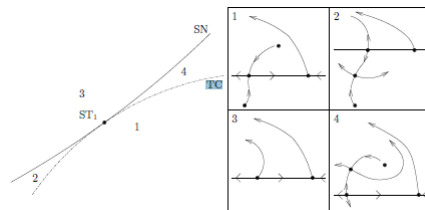


Figure 1.6: Illustration of the Saddle-node-transcritical bifurcation [11].

---

in the perturbative picture, starting from the bare action, as in the exact picture, starting from the effective action, the flow of the dynamical system  $\langle \mathcal{T}, \mathbb{R} \rangle$  provides insight in the physical properties of a certain theory. First of all it shows how coupling constants change with energy scales in certain theories. In addition, two theories with different coupling constants that both have an orbit towards the same stable point will be represented by a similar theory in the IR limit, and vice versa for the UV limit. The flow field represents a phase diagram in theory space. Different phases in theory space yield qualitatively different theories. One could study the change of these phase diagrams when the number of field-components, the dimension of a certain symmetry group or the dimension of space-time is changed. These parameters can be used as bifurcation parameters. Bifurcation analysis of the renormalization group flows then provides information about the change of the theory when these parameters are changed, and about the existence of qualitative different theories within a certain framework.

A first step in this direction has recently been made by Gukov [16]. In this paper, among other things a saddle-node bifurcation is found in the  $\text{QCD}_4$  model, which will be discussed in the next section. A question, that is raised, is whether other bifurcations can be found in more complicated models, and what this implies for those models. Furthermore, another question raised by Wilson already in 1971 [17] was whether limit cycles may appear in renormalization group flows. A limit cycle would be associated to a Hopf bifurcation in the dynamical system, and would represent a physical theory, where the coupling constants behave periodically with increasing energy scales. Some examples of theories with limit cycles have been constructed [18], [19] and [20]. However, so far all examples in QFT either break unitarity or relativistic invariance [21]. Also, more exotic behavior like chaos might be found in RG-flows [22]. Bifurcation analysis is an ideal tool to study the existence of and transition to exotic behavior in various field theories.

---

## 2 QCD<sub>4</sub>

Quantum Chromodynamics describes the strong interactions that bind quarks together. On a fundamental level it describes the interactions between quarks and gluons. The quark model described by QCD contains  $N_f$  massive flavors of quarks, which can be described by fermion fields, and each quark comes in  $N_c$  colors. Quantum Chromodynamics is a typical example of a non-abelian gauge theory, which is a type of quantum field theory, where the Lagrangian is invariant under local (gauge) transformations, that can be described by certain groups. The group associated to this symmetry in QCD is  $SU(N_c)$ , which is a non-abelian Lie group. The generators of the group can generally be associated to bosonic particles, transferring the force between the fermionic fields. In QCD these particles are known as gluons. Within the standard model of particle physics, there are 3 colors,  $N_c = 3$ , and therefore 8 gluons, and 6 massive flavors,  $N_f = 6$ . Theoretically, one can extend such theories to general  $N_c, N_f \in \mathbb{N}$ . This extension plays an important role in the search for theories beyond the standard model of particle physics, and also for the study of the quark-gluon plasma. Theories with a  $SU(N)$  symmetry are generally known as Yang-Mills theories, and are applicable to a wide range of physical phenomena, also within condensed matter [23]. Here, we consider Quantum Chromodynamics with  $N_f$  quark flavors and  $N_c$  colors in 4 space-time dimensions (as expressed by the 4 in QCD<sub>4</sub>). The Lagrangian is then given by

$$\mathcal{L} = -\frac{1}{4}G_{\mu\nu}^A G_A^{\mu\nu} + \sum_{i=1}^{N_f} \bar{\psi}_{ai} (i\mathcal{D}_b^a - m_i\delta_b^a) \psi^{bi}, \quad (2.1)$$

where  $\mu \in \{0, \dots, 3\}$  labels the space-time dimension,  $i \in \{1, \dots, N_f\}$  labels the flavor in the fundamental representation of  $SU(N_f)$ ,  $a \in \{1, \dots, N_c\}$  labels the color in the fundamental representation of  $SU(N_c)$  and  $A \in \{1, \dots, (N_c^2 - 1)\}$  the color in the adjoint representation of  $SU(N_c)$ . The field strength is given by  $G_{\mu\nu}^A = \partial_\mu A_\nu^A - \partial_\nu A_\mu^A + gf_{BC}^A [A_\mu^B, A_\nu^C]$ , and the differential operator by  $D_\mu = \partial_\mu - igt_A A_\mu^A$ , where  $\{t_A\}$  are the generators of  $SU(N_c)$ .  $A_\mu^A$  is the gluon gauge field, and  $\psi^{ai}$  are the fermion fields. The fermion fields can be represented as a 4-component spinor or as two 2-component spinors (left and right). We set the fermion masses  $m_i = 0$ . The Lagrangian has by construction a local (coordinate dependent)  $SU(N_c)$  symmetry, acting on the fields as  $\psi(x) \rightarrow U(x)\psi(x), \bar{\psi}(x) \rightarrow \bar{\psi}(x)U^\dagger(x), U(x) \in SU(N_c)$ . Furthermore, it has a global  $U(1)_V$  symmetry acting on the fermion fields and a global  $SU(N_f)_L \times SU(N_f)_R$  symmetry, acting on the left and right handed fermion fields (the two 2-component representations) independently. This last chiral symmetry can be spontaneously broken into a  $SU(N_f)_V$  symmetry acting on the 4 component representation of the fermion field. This symmetry breaking forms a quark condensate, and is studied further in this thesis.

A main property of QCD is color confinement. Color confinement states that coupling between quarks grows when the energy is decreased (length scale is increased) and can even diverge. This divergence results in the fact that quarks can't be pulled apart without creating a new pair of quarks, which is the reason why quarks are always confined within matter such as protons and neutrons or hadrons. Only at very large temperature this confinement may be overcome and a quark gluon plasma can be formed, where quarks can exist as interacting particles. This happened microseconds after the big bang in our universe and happens in high energy particle collisions such as at CERN or at SLAC [24]. Furthermore, we expect it to happen at the core of Neutron stars [25], where pressure is very high. At even higher temperatures the interaction between quarks becomes weaker until quarks can move around freely. The confinement of quarks is a result of the color charge of the quarks, and may also be overcome by increasing the ratio of the number of massless quark flavors

---

over the number of colors. For this, the QCD model needs to have the  $SU(N_f)_L \times SU(N_f)_R$  symmetry. We define the ratio

$$x = \frac{N_f}{N_c}.$$

It is known [26] that for high ratios  $x > 5.5$  coupling between quarks through gluons is zero, and quarks can move around freely (without interactions) at low energy scales. These kind of theories are infrared free. Below this value, the coupling constants in the low energy limit start to grow, making the theory infrared safe, meaning that the coupling is non-zero but finite. At lower ratios, the low energy coupling will diverge, and color confinement will set in. The range where the theory is infrared safe is known as the conformal window, because of the existence of non-trivial fixed points, where the quantum field theory is conformally symmetric. The upper edge of this window is well known, but little is known exactly about the value of the lower edge and the phase transition happening there, although multiple scenarios have been considered. Multiple approaches have indicated that the conformal window at of the quantum field theory at zero temperature is continuously connected to the the quark-gluon plasma phase at high temperatures [27–29], implying that the study of the conformal window can shine a light on the quark gluon-plasma and vice versa.

A problem here is that due to the growth of the coupling in the low energy limit of the conformal window, the perturbative calculation of the beta functions are no longer a good approximation, and therefore the behavior at the lower edge can't be described by perturbative calculations. A common way to do calculations in QCD is the use of lattice regularization. Lattice regularization, as opposed to dimensional regularizations introduced in the introduction, regularizes the divergences in the theory by discretizing space-time into a lattice. The regularization parameter is then the lattice spacing. The limit where the lattice spacing goes to 0 should give the true continuum limit. Lattice regularization keeps all symmetries that where present in the Lagrangian, but it destroys the Poincaré symmetry (invariance under transformations of space-time generated by the Poincaré group), which comes from special relativity. The lattice approximation provides a framework to do simulations of the theory. Simulation with many lattice sites, and therefore small lattice spacing can give useful results in QCD.

Another common approach in QCD is the use of the holographic principle [28–30], which can be used very well in the conformal window. In the conformal window both the high and the low energy limit are represented by fixed points of the beta function. At these fixed points the theory is invariant under conformal transformations and therefore defines a conformal field theory. According to the holographic principle there can be dual geometric theories to these conformal field theories. Therefore, the behavior at and close to fixed points can be described with geometry, which yields a new set of computational methods to derive properties of the theory.

In this thesis, we'll take another approach to the problem. Here, we include effective interactions between the quarks that one expects to appear at low energies. Through the addition of effective interactions, we include many terms in the beta function, which otherwise could only be included by going to infinite order in perturbation theory. We call these non-perturbative terms. The downside of the method is that many other terms that would be included in high order of perturbation theory will be left out, unless all effective interactions are taken into account. In this thesis we only consider the effective four-fermi interactions, as was done in [32]. It is believed that these play an important role for chiral symmetry breaking at the lower edge of the conformal window [38]. Higher order effective interactions are left out. It is natural to expect that most of them would be irrelevant, although some might play a role at the lower edge of the conformal window. Adding higher order effective interactions would make both the calculation and the analysis of the beta

functions more complicated, but could be done in further studies.

## 2.1 The Beta Functions

In order to study the behavior of the theory in the Wilsonian picture, we need to find the effective action, which is given by the Legendre transform of the Lagrangian (2.1). We impose the symmetries obeyed by the Lagrangian on the effective action and expand the effective action in the quark fields  $\psi^{ai}$  up to the 4-quark interactions. This yields

$$\Gamma_\Lambda = \int d^4x \left( -\frac{1}{4g^2} G_{\mu\nu}^A G^{A\mu\nu} + \bar{\psi}_{ai} i \not{D} \psi^{ai} + \mathcal{L}_{4f} \right), \quad (2.2)$$

where we have redefined the gauge fields  $A \rightarrow A' = gA$ , such that  $G_{\mu\nu}^A \rightarrow \frac{1}{g} G_{\mu\nu}^A$  and  $D_\mu = \partial_\mu - it_A A_\mu^A$ . Imposing the symmetries, one can find four independent four-fermi operators, which are given by [31]

$$\mathcal{L}_{4f} = \frac{G_S}{\Lambda^{2(1+\eta)}} \mathcal{O}_S + \frac{G_V}{\Lambda^{2(1+\eta)}} \mathcal{O}_V + \frac{G_{V_1}}{\Lambda^{2(1+\eta)}} \mathcal{O}_{V_1} + \frac{G_{V_2}}{\Lambda^{2(1+\eta)}} \mathcal{O}_{V_2},$$

where  $\eta = \gamma_\psi$  is the anomalous dimension of the fermion field and

$$\begin{aligned} \mathcal{O}_S &= 2\bar{L}_i R^j \bar{R}_j L^i = \frac{1}{2} [\bar{\psi}_i \psi^j \bar{\psi}_j \psi^i - \bar{\psi}_i \gamma_5 \psi^j \bar{\psi}_j \gamma_5 \psi^i], \\ \mathcal{O}_V &= \bar{L}_i \gamma^\mu L^j \bar{L}_j \gamma_\mu L^i + (L \leftrightarrow R) = \frac{1}{2} [\bar{\psi}_i \gamma^\mu \psi^j \bar{\psi}_j \gamma_\mu \psi^i + \bar{\psi}_i \gamma^\mu \gamma_5 \psi^j \bar{\psi}_j \gamma_\mu \gamma_5 \psi^i], \\ \mathcal{O}_{V_1} &= 2\bar{L}_i \gamma^\mu L^i \bar{R}_j \gamma_\mu R^j = \frac{1}{2} [(\bar{\psi}_i \gamma^\mu \psi^i)^2 - (\bar{\psi}_i \gamma^\mu \gamma_5 \psi^i)^2], \\ \mathcal{O}_{V_2} &= (\bar{L}_i \gamma^\mu L^i)^2 + (L \leftrightarrow R) = \frac{1}{2} [(\bar{\psi}_i \gamma^\mu \psi^i)^2 + (\bar{\psi}_i \gamma^\mu \gamma_5 \psi^i)^2], \end{aligned}$$

where the color indices are contracted and  $i, j$  represent the flavor index. From now on, we will use rescaled parameters  $g_i = \frac{G_i}{4\pi^2}$  and  $\alpha_g = \frac{g^2}{(4\pi)^2}$ . We calculate the beta function of the four-fermi interaction using the Wetterich equation (1.36). This is done in appendix C. The beta function for the gauge coupling  $\alpha_g$  can't be derived from the effective action (2.2) easily, since we would have to include an expansion in the gluon fields to the effective action [32], which makes calculations fairly complicated. Instead, we start from the perturbative equation and include the effective four-fermi interactions to it. The calculation for this beta function can be found in appendix B. The complete set of beta-functions is given by<sup>2.1</sup>

$$\left\{ \begin{aligned} \Lambda \frac{d\alpha_g}{d\Lambda} &= -\frac{2}{3}(11N_c - 2N_f)\alpha_g^2 - \frac{2}{3} \left( 34N_c^2 - 13N_c N_f + 3\frac{N_f}{N_c} \right) \alpha_g^3 + 2N_c N_f g_V \alpha_g^2, \\ \Lambda \frac{dg_S}{d\Lambda} &= 2g_S - 2N_c g_S^2 + 2N_f g_S g_V + 6g_S g_{V_1} + 2g_S g_{V_2} \\ &\quad - 6 \left( N_c - \frac{1}{N_c} \right) g_S \alpha_g + 12g_{V_1} \alpha_g - \frac{3}{2} \left( 3N_c - \frac{8}{N_c} \right) \alpha_g^2, \\ \Lambda \frac{dg_V}{d\Lambda} &= 2g_V + \frac{N_f}{4} g_S^2 + (N_c + N_f) g_V^2 - 6g_V g_{V_2} \\ &\quad - \frac{6}{N_c} g_V + 6g_{V_2} \alpha_g - \frac{3}{4} \left( N_c - \frac{8}{N_c} \right) \alpha_g^2, \\ \Lambda \frac{dg_{V_1}}{d\Lambda} &= 2g_{V_1} - \frac{1}{4} g_S^2 - g_S g_V - 3g_{V_1}^2 - N_f g_S g_{V_2} + 2(N_c + N_f) g_V g_{V_1} \\ &\quad + 2(N_c N_f + 1) g_{V_1} g_{V_2} + \frac{6}{N_c} g_{V_1} \alpha_g + \frac{3}{4} \left( 1 + \frac{4}{N_c^2} \right) \alpha_g^2, \\ \Lambda \frac{dg_{V_2}}{d\Lambda} &= 2g_{V_2} - 3g_V^2 - N_c N_f g_{V_1}^2 + (N_c N_f - 2) g_{V_2}^2 - N_f g_S g_{V_1} \\ &\quad + 2(N_c + N_f) g_V g_{V_2} + 6g_V \alpha_g - \frac{6}{N_c} g_{V_2} \alpha_g - \frac{3}{4} \left( 3 + \frac{4}{N_c^2} \right) \alpha_g^2. \end{aligned} \right. \quad (2.3)$$

<sup>2.1</sup>We find a slightly different model from the one presented in [32]. In the Veneziano limit the models are the same.



For further study, we define new parameters

$$x := \frac{N_f}{N_c}, \quad N := N_c.$$

Notice that one can add loops to any diagram by adding gauge or four-fermion vertices. When adding two gauge vertices, the scalar or the vector interaction, this gives an extra factor  $a$  or  $aN$ , where  $a$  is a finite constant, while adding a  $\mathcal{O}_{V_1}$  or  $\mathcal{O}_{V_2}$  interaction can bring in a factor  $a$ ,  $aN$  or  $aN^2$ . Therefore, we do another rescaling

$$\begin{aligned} N\alpha_g &\rightarrow \alpha_g \\ Ng_S &\rightarrow g_S \\ Ng_V &\rightarrow g_V \\ N^2g_{V_1} &\rightarrow g_{V_1} \\ N^2g_{V_2} &\rightarrow g_{V_2}, \end{aligned} \tag{2.4}$$

which allows us to study the Veneziano limit, where  $N \rightarrow \infty$  and  $x$  remains finite. All terms that may appear in the beta functions will either be suppressed or give a constant contribution in the Veneziano limit, when this rescaling is used. This yields

$$\left\{ \begin{aligned} \Lambda \frac{d\alpha_g}{d\Lambda} &= -\frac{2}{3}(11-2x)\alpha_g^2 - \frac{2}{3}(34-13x)\alpha_g^3 + 2xg_V\alpha_g^2 \\ &\quad + N^{-2}(-2x\alpha_g^3), \\ \Lambda \frac{dg_S}{d\Lambda} &= 2g_S - 2g_S^2 + 2xg_Sg_V - 6g_S\alpha_g - \frac{9}{2}\alpha_g^2 \\ &\quad + N^{-2}(6g_Sg_{V_1} + 2g_Sg_{V_2} + 6g_S\alpha_g + 12g_{V_1}\alpha_g + 12\alpha_g^2), \\ \Lambda \frac{dg_V}{d\Lambda} &= 2g_V + \frac{1}{4}xg_S^2 + (1+x)g_V^2 - \frac{3}{4}\alpha_g^2 \\ &\quad + N^{-2}(-6g_Vg_{V_2} - 6g_V\alpha_g + 6g_{V_2}\alpha_g + 6\alpha_g^2), \\ \Lambda \frac{dg_{V_1}}{d\Lambda} &= 2g_{V_1} - \frac{1}{4}g_S^2 - g_Sg_V - xg_Sg_{V_2} + 2(1+x)g_Vg_{V_1} + 2xg_{V_1}g_{V_2} + \frac{3}{4}\alpha_g^2 \\ &\quad + N^{-2}(-3g_{V_1}^2 + 2g_{V_1}g_{V_2} + 6g_{V_1}\alpha_g + 3\alpha_g^2), \\ \Lambda \frac{dg_{V_2}}{d\Lambda} &= 2g_{V_2} - 3g_V^2 - xg_{V_1}^2 + xg_{V_2}^2 - xg_Sg_{V_1} + 2(1+x)g_Vg_{V_2} + 6g_V\alpha_g - \frac{9}{4}\alpha_g^2 \\ &\quad + N^{-2}(-2g_{V_2}^2 - 6g_{V_2}\alpha_g - 3\alpha_g^2). \end{aligned} \right. \tag{2.5}$$

Finally, we define the time parameter  $t = -\ln(\Lambda)$ , such that the orbits of the RG-flow are directed from high energy (UV) scales towards low energy (IR) scales, and find

$$\left\{ \begin{aligned} \frac{d\alpha_g}{dt} &= \frac{2}{3}(11-2x)\alpha_g^2 + \frac{2}{3}(34-13x)\alpha_g^3 - 2xg_V\alpha_g^2 \\ &\quad + N^{-2}(2x\alpha_g^3), \\ \frac{dg_S}{dt} &= -2g_S + 2g_S^2 - 2xg_Sg_V + 6g_S\alpha_g + \frac{9}{2}\alpha_g^2 \\ &\quad + N^{-2}(-6g_Sg_{V_1} - 2g_Sg_{V_2} - 6g_S\alpha_g - 12g_{V_1}\alpha_g - 12\alpha_g^2), \\ \frac{dg_V}{dt} &= -2g_V - \frac{1}{4}xg_S^2 - (1+x)g_V^2 + \frac{3}{4}\alpha_g^2 \\ &\quad + N^{-2}(6g_Vg_{V_2} + 6g_V\alpha_g - 6g_{V_2}\alpha_g - 6\alpha_g^2), \\ \frac{dg_{V_1}}{dt} &= -2g_{V_1} + \frac{1}{4}g_S^2 + g_Sg_V + xg_Sg_{V_2} - 2(1+x)g_Vg_{V_1} - 2xg_{V_1}g_{V_2} - \frac{3}{4}\alpha_g^2 \\ &\quad + N^{-2}(3g_{V_1}^2 - 2g_{V_1}g_{V_2} - 6g_{V_1}\alpha_g - 3\alpha_g^2), \\ \frac{dg_{V_2}}{dt} &= -2g_{V_2} + 3g_V^2 + xg_{V_1}^2 - xg_{V_2}^2 + xg_Sg_{V_1} - 2(1+x)g_Vg_{V_2} - 6g_V\alpha_g + \frac{9}{4}\alpha_g^2 \\ &\quad + N^{-2}(2g_{V_2}^2 + 6g_{V_2}\alpha_g + 3\alpha_g^2). \end{aligned} \right. \tag{2.6}$$

## 2.2 The Veneziano Limit

In this section, we study the Veneziano limit of the model (2.6) as was done in [16] and [32].<sup>2.2</sup> The Veneziano limit,  $N \rightarrow \infty$  yields

$$\begin{cases} \frac{d\alpha_g}{dt} &= \frac{2}{3}(11 - 2x)\alpha_g^2 + \frac{2}{3}(34 - 13x)\alpha_g^3 - 2xg_V\alpha_g^2, \\ \frac{dg_S}{dt} &= -2g_S + 2g_S^2 - 2xg_Sg_V + 6g_S\alpha_g + \frac{9}{2}\alpha_g^2, \\ \frac{dg_V}{dt} &= -2g_V - \frac{1}{4}xg_S^2 - (1+x)g_V^2 + \frac{3}{4}\alpha_g^2, \\ \frac{dg_{V_1}}{dt} &= -2g_{V_1} + \frac{1}{4}g_S^2 + g_Sg_V + xg_Sg_{V_2} - 2(1+x)g_Vg_{V_1} - 2xg_{V_1}g_{V_2} - \frac{3}{4}\alpha_g^2, \\ \frac{dg_{V_2}}{dt} &= -2g_{V_2} + 3g_V^2 + xg_{V_1}^2 - xg_{V_2}^2 + xg_Sg_{V_1} - 2(1+x)g_Vg_{V_2} - 6g_V\alpha_g + \frac{9}{4}\alpha_g^2. \end{cases} \quad (2.7)$$

The first three equations decouple from the last 2. Therefore, we can reduce analysis to the system<sup>2.3</sup>

$$\begin{cases} \dot{\alpha}_g &= \frac{2}{3}(11 - 2x)\alpha_g^2 + \frac{2}{3}(34 - 13x)\alpha_g^3 - 2xg_V\alpha_g^2, \\ \dot{g}_S &= -2g_S + 2g_S^2 - 2xg_Sg_V + 6g_S\alpha_g + \frac{9}{2}\alpha_g^2, \\ \dot{g}_V &= -2g_V - \frac{1}{4}xg_S^2 - (1+x)g_V^2 + \frac{3}{4}\alpha_g^2. \end{cases} \quad (2.8)$$

The domain of the variables and parameters is given by  $x \in \mathbb{R}^+$ ,  $\alpha \in \mathbb{R}_0^+$  and  $g_S, g_V \in \mathbb{R}$ . Due to the approximate nature of the model (2.3), we expect better results for small parameter values. As a rough bound on the size of the parameter values, we use  $\alpha_g < 1$ ,  $|g_i| < 1$ .

The beta function for  $\alpha_g$  has a double root for  $\alpha_g^t = 0$  and another root for  $\alpha_g^{nt} = \frac{11-2x-3xg_V}{13x-34}$ . Therefore, the fixed points of the RG-flow lie on these manifolds. The manifold defined by  $\alpha_g = 0$  is an invariant set of the system, since  $\dot{\alpha}_g$  vanishes for  $\alpha_g = 0$ .

The behavior of the fixed points projected on the  $(x, \alpha_g)$ -plane,  $(x, g_S)$ -plane and the  $(x, g_V)$ -plane is shown in figure 2.1, and the projections on the  $(x, \alpha_g, g_S)$ -space,  $(x, \alpha_g, g_V)$ -space and the  $(x, g_S, g_V)$ -space in figure 2.2. We use the following color coding:

- Solid red line: stable node, 3 negative eigenvalues.
- Dashed red line: saddle point, 2 negative and 1 positive eigenvalue.
- Dashed blue line: saddle point, 1 negative and 2 positive eigenvalues.
- Solid blue line: unstable node, 3 positive eigenvalues.

The equilibria on the  $\alpha_g = 0$  manifold all have a trivial eigenvalue, and therefore do not fit the color coding as described above. In order to use the color coding, we define the sign of a trivial eigenvalue on this manifold by approaching the equilibrium along a line of constant  $g_S$  and  $g_V$  from positive but small  $\alpha_g$ . The trivial eigenvalue will then approach 0 from either positive or negative values. If the trivial eigenvalue is slightly positive for  $0 < \alpha_g \ll 1$ , we define the trivial eigenvalue to be positive and vice versa.

In figures 2.1 and 2.2, 4 up to 8 equilibria are shown, depending on the value of  $x$ . Furthermore, a few bifurcations are found. The parameter and coordinate values of these bifurcations are reported in table 1. The Branching points all correspond to transcritical

<sup>2.2</sup>The results in this section are an extension of the results discussed in [16] and mainly serve as an introduction into the complete model. Furthermore, they are a variation on the results from [32] in the sense that some parts are discussed more completely, while other parts are omitted.

<sup>2.3</sup>The orbits still have components in the  $g_{V_1}$  and  $g_{V_2}$  direction, which depend on the coordinates  $(\alpha_g, g_S, g_V)$ . However, the flow projected on the  $(\alpha_g, g_S, g_V)$  is independent of  $g_{V_1}$  and  $g_{V_2}$ . Therefore, the reduced system provides solid information about the flow in the complete 5-dimensional system.

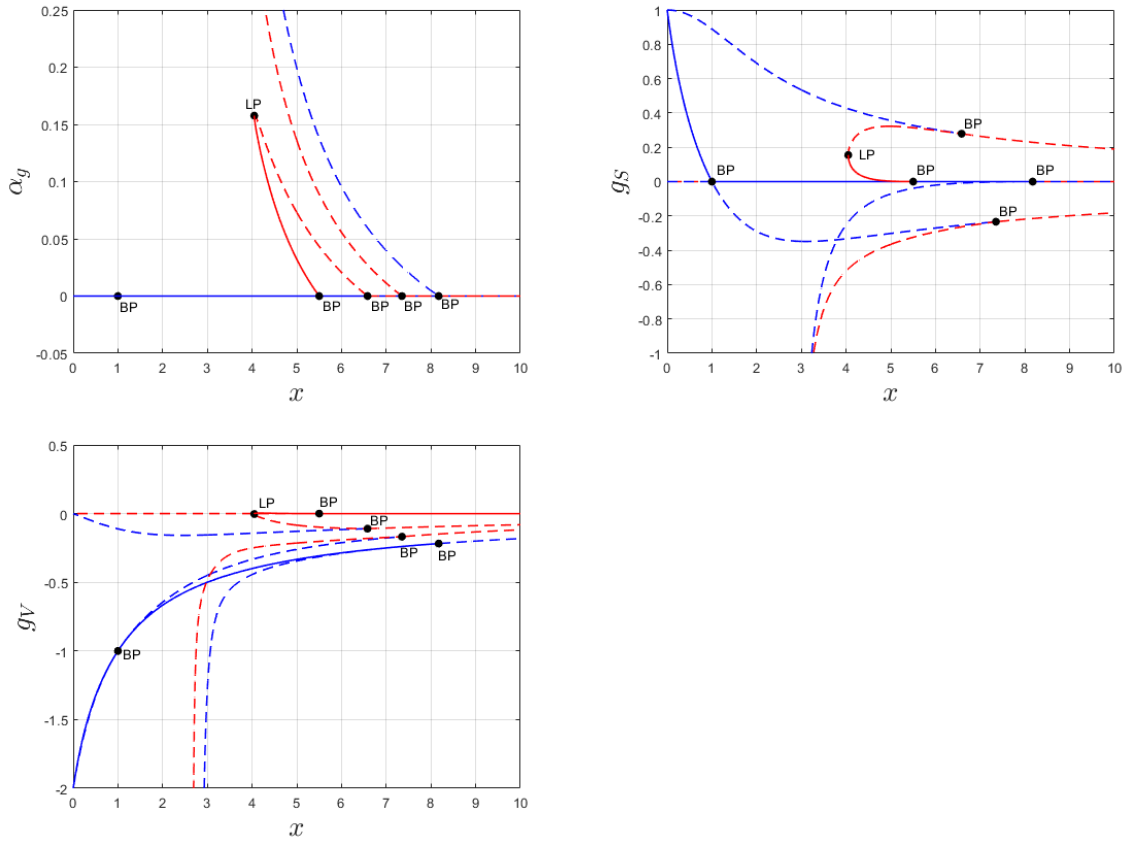


Figure 2.1: The fixed points of the RG-flow of (2.8) projected on the  $(x, \alpha_g)$ -plane,  $(x, g_S)$ -plane and the  $(x, g_V)$ -plane. Solid red line: stable node. Dashed red line: saddle with 1 positive eigenvalue. Dashed blue line: saddle with 2 positive eigenvalues. Solid blue line: unstable node. LP: Limit Point. BP: Branching Point.

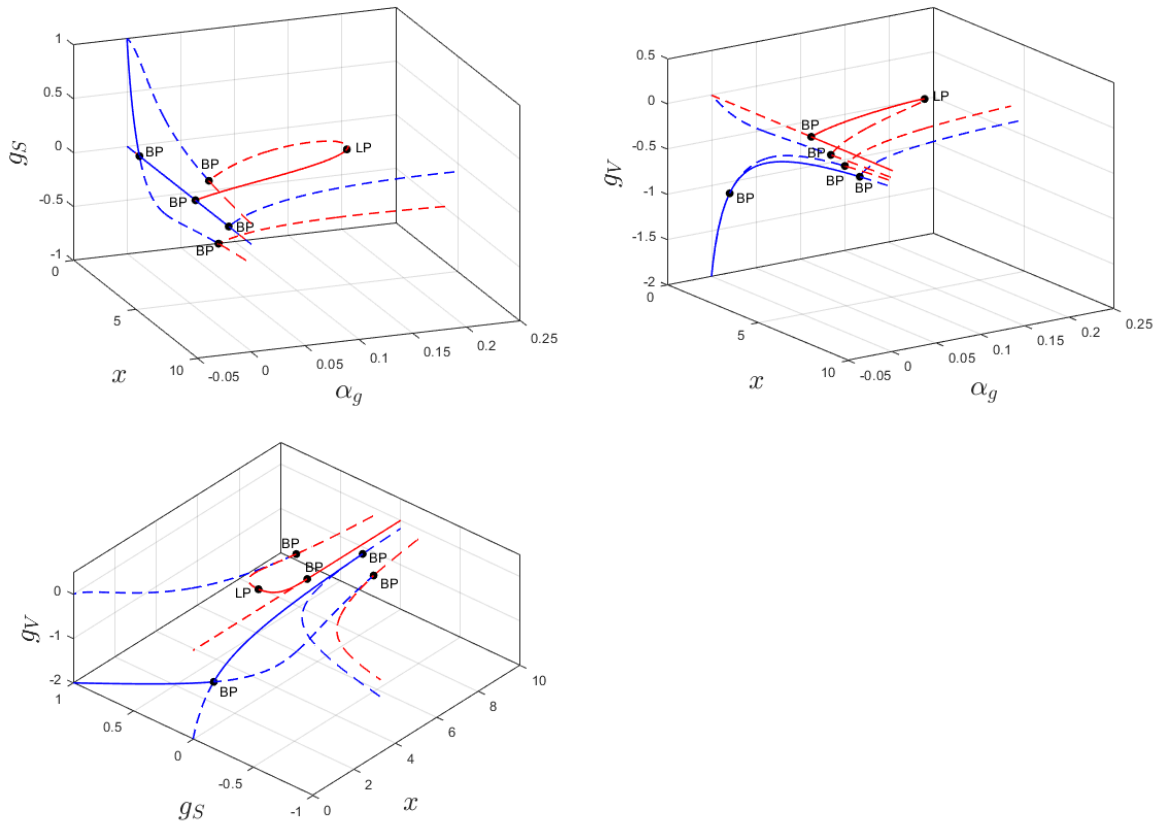


Figure 2.2: The fixed points of the RG-flow of (2.8) projected on the  $(x, \alpha_g, g_S)$ -space,  $(x, \alpha_g, g_V)$ -space and the  $(x, g_S, g_V)$ -space. Solid red line: stable node. Dashed red line: saddle with 1 positive eigenvalue. Dashed blue line: saddle with 2 positive eigenvalues. Solid blue line: unstable node. LP: Limit Point. BP: Branching Point.

bifurcations. The transcritical bifurcation at  $x = 1$  is located in the subspace  $\alpha_g = 0$ , while the other transcritical bifurcations are located on the intersection of the subspaces  $\alpha_g = 0$  and  $\alpha_g = \alpha_g^{nt}$ . In the last case, both a trivial and a non-trivial equilibrium<sup>2,4</sup> are involved. At all the non-trivial equilibria, the equilibrium has a positive eigenvalue, when  $\alpha_g < 0$ , that becomes negative when  $\alpha_g > 0$ , while the trivial equilibrium has a negative eigenvalue that becomes positive. At the branching point at  $x = 5.5$  a stable node with  $\alpha_g > 0$  is created. This indicates the upper edge of the conformal window as discussed in the introduction of this section. Finally, at  $x = 4.05$  two non-trivial equilibria collide and disappear through a saddle-node bifurcation (limit point). This saddle-node bifurcation could indicate the lower edge of the conformal window through a fixed point merger, as was discussed in [32] and [16]. The two other non-trivial fixed points diverge for  $x \lesssim 2.5$ .

Table 1: Locations of bifurcations found in model (2.8) for QCD<sub>4</sub> in the Veneziano limit.

Bifurcation	$x$	$\alpha_g$	$g_S$	$g_V$
Saddle-node	4.0489	0.1576	0.1550	-0.0029
Transcritical	1.0001	0	0	-1.0000
Transcritical	5.5005	0	0	0
Transcritical	6.5819	0	0.2790	-0.1095
Transcritical	7.3512	0	-0.2338	-0.1678
Transcritical	8.1731	0	0	-0.2180

A few characteristic orbits of the RG-flow in the Veneziano limit are visualized in figures 2.3, 2.4, 2.5, 2.6 and 2.7.

In figure 2.3, a phase portrait on the invariant plane  $\alpha_g = 0$  is shown at  $x = 5$ . We see 4 fixed points, and 4 red heteroclinic orbits connecting those fixed points marking the boundaries of an invariant set. All orbits inside this set have a finite UV and finite IR fixed point, while orbits outside the invariant set have a diverging IR limit, a diverging UV limit or both. The structure of this flow doesn't change, when  $x$  is varied in the region  $x > 1$ . Only the location of the fixed points and connecting orbits will change continuously. At  $x = 1$ , the two fixed points with lowest value of  $g_V$  collide and exchange stability, via a transcritical bifurcation, yielding a similar phase portrait.

In figure 2.4, a phase portrait of the flow in the whole space is shown at  $x = 5$ . Here, all 8 fixed points are shown, together with a few heteroclinic orbits connecting them. The red heteroclinic orbits form a skeleton of a 3-dimensional invariant set. This invariant set is bound by six invariant planes. The solid red lines lie on the intersections of these planes. The dashed red lines indicate the presence of other intersections, which haven't been found numerically. All orbits inside this set have a finite UV and IR fixed point, while orbits outside the invariant set have a diverging IR limit, a diverging UV limit or both. More precisely, the bulk of the invariant set consists of structurally stable orbits going from the equilibrium at  $(\alpha_g, g_S, g_V) = (0, 0, -0.333)$  to the equilibrium at  $(\alpha_g, g_S, g_V) = (0.032, 0.003, 0.000)$ , and the boundary planes consist of non-stable heteroclinic orbits between the other fixed points. Within the invariant set the theory is in a chirally symmetric phase, while outside the set the chiral symmetry is broken. The structure of this flow doesn't change when  $x$  is varied in the region  $4.05 < x < 5.5$ . Only the location of the fixed points and connecting orbits will change continuously. At  $x = 4.05$  the two fixed points shown at  $(\alpha_g, g_S, g_V) = (0.032, 0.003, 0.000)$  and  $(\alpha_g, g_S, g_V) = (0.073, 0.322, -0.084)$  disappear through a saddle-node bifurcation. A projection of the orbits on the  $g_S = 0$  plane is shown in figure 2.5. We notice that some of the orbits appear to intersect each other due to the fact that they're projected on a non-invariant plane. This intersection is not present in the 3-dimensional space.

<sup>2,4</sup>We call a fixed point trivial, if it has a trivial  $\alpha_g$  value and non-trivial otherwise.

In figure 2.6, a phase portrait in the whole space is shown at  $x = 4$ . Here, only 6 fixed points are left. The six fixed points together span two unstable bounded 2-dimensional invariant sets. The solid red lines border these sets, and the dashed red line indicates the location, where the last border is expected, which hasn't been found numerically. The 3-dimensional invariant set, which was present at  $x = 5$ , has been broken down at the saddle-node bifurcation to two 2-dimensional invariant planes. The structure of the flow doesn't change when  $x$  is varied in the region  $0 < x < 4.05$ , but the two non-trivial fixed points diverge when  $x$  is lowered towards  $x = 2.5$ . A projection of some orbits on the  $g_S = 0$  plane is shown in figure 2.7. The orbits outside of the invariant planes all diverge in the IR limit. The eigenvector with 0 eigenvalue at the saddle-node bifurcation<sup>2.5</sup> is mainly directed in the  $g_S$  direction, as can be found in table 2. Therefore, the divergence is the strongest in the  $g_S$  direction, indicating that the chiral symmetry is broken due to the scalar part of the four-fermi interaction, as discussed in [38]. Furthermore, we notice that there still are chirally symmetric trajectories with a zero UV and finite IR limit, but these are unstable, and therefore need a very precise fine-tuning, which makes them unlikely to occur in nature.

Table 2: Eigenvalues and eigenvectors at the saddle-node bifurcation at  $x = 4.0489$ .

Eigenvalue	Eigenvector w.r.t the basis $\{e_\alpha, e_S, e_V\}$
0	(0.09, 0.98, -0.15)
-0.56	(0.19, -0.95, 0.24)
-2.13	(0.10, 0.50, 0.86)

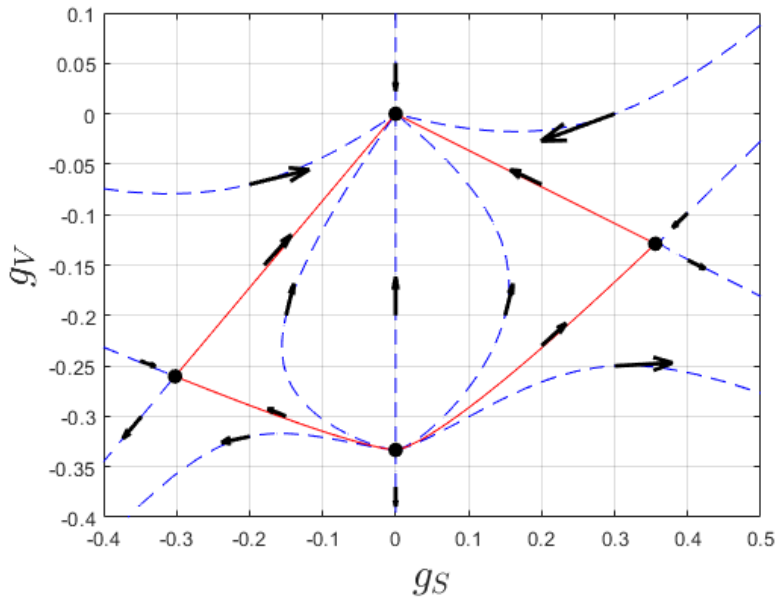


Figure 2.3: Phase portrait of the RG-flow in the  $(g_S, g_V)$ -plane for  $\alpha_g = 0$  in the Veneziano limit at  $x = N_f/N_c = 5$ . Solid red lines indicate the boundaries of an invariant set.

<sup>2.5</sup>This eigenvector is directly related to the operator that crosses marginality in the language of RG-flow.

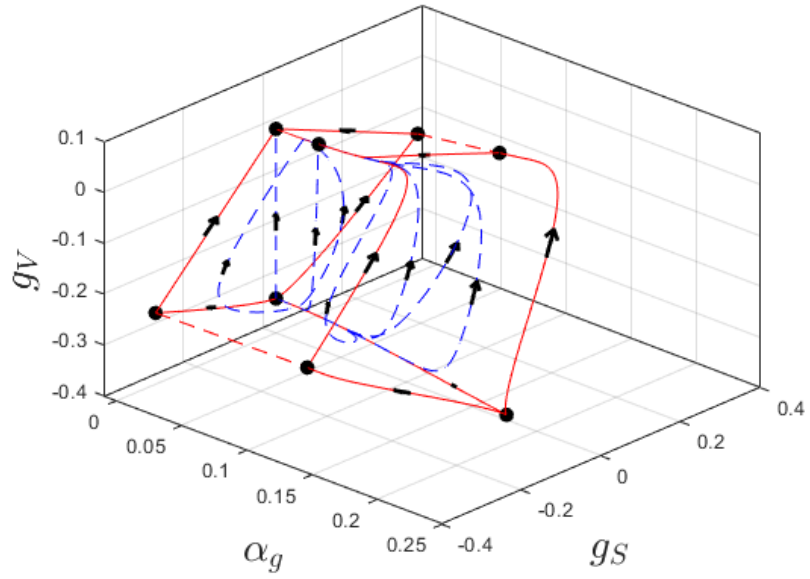


Figure 2.4: Phase portrait of the RG-flow in the  $(\alpha_g, g_S, g_V)$ -space in the Veneziano limit at  $x = N_f/N_c = 5$ . Red lines indicates the skeleton of an invariant set.

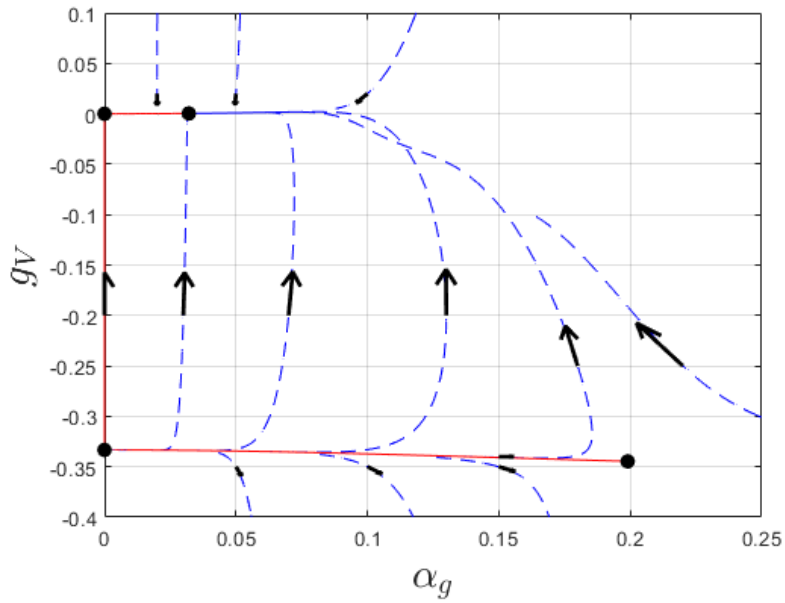


Figure 2.5: Phase portrait of the RG-flow projected on the  $(\alpha_g, g_V)$ -plane at  $g_S = 0$  in the Veneziano limit at  $x = N_f/N_c = 5$ . Red lines indicate the skeleton of an invariant set.

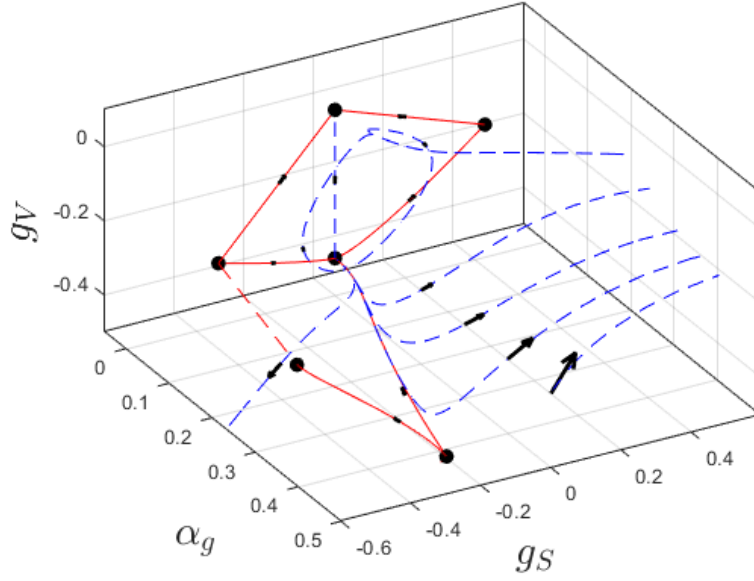


Figure 2.6: Phase portrait of the RG-flow in the  $(\alpha_g, g_S, g_V)$ -space in the Veneziano limit at  $x = N_f/N_c = 4$ . Red lines indicate the boundaries of 2-dimensional invariant sets.

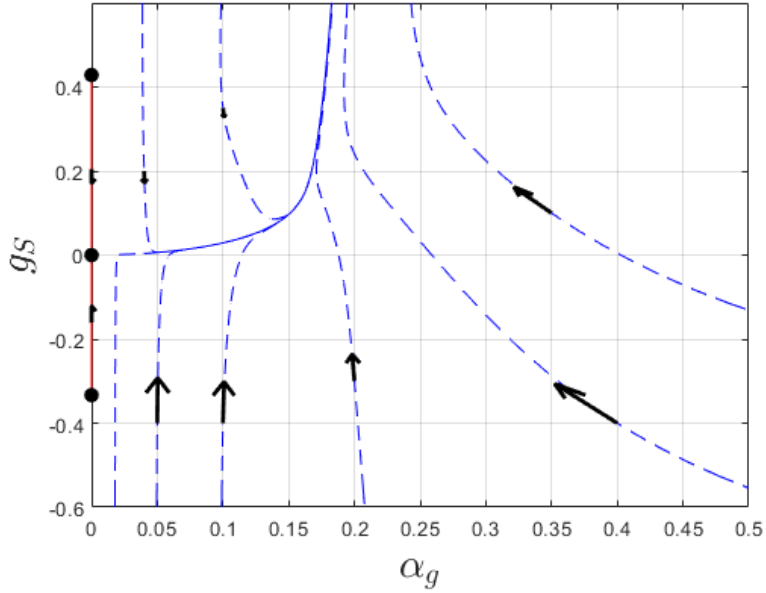


Figure 2.7: Phase portrait of the RG-flow projected on the  $(\alpha_g, g_S)$ -plane at  $g_V = 0$  in the Veneziano limit at  $x = N_f/N_c = 4$ . Red lines indicate the boundaries of 2-dimensional invariant sets.



## 2.3 The Complete Model

In the full model there are 2 bifurcation parameters  $N_c$  and  $x = N_f/N_c$ , which allows for more interesting types of bifurcations. Again, we are interested in the renormalized trajectories of the theory and the invariant sets enclosed by the renormalized trajectories, indicating the existence of chirally symmetric theories. The fixed points of the theory can be found numerically, and it's easily verified that the model contains up to 20 different real fixed points with  $\alpha_g \geq 0$  for integer values of  $(N_c, N_f) \in [1, 10] \times [1, 100]$ . The beta function for  $\alpha_g$  yields two roots

$$\alpha_g = 0, \quad \alpha_g = \alpha_g^{nt} := N_c^2 \frac{-11N_c + 2N_f + 3N_f g_V}{34N_c^3 - 13N_c^2 N_f + 3N_f},$$

where the trivial root has multiplicity two. The  $\alpha_g = 0$  plane is an invariant set of the model, which allows to study the model without gauge interactions separately. Setting  $\alpha_g = 0$ , one can find up to 12 fixed points, which can be continued using MatCont. Bifurcations found in this 4-dimensional subspace are shown in figure 2.8. The bifurcation curves separate the diagram into multiple regions. In the upper left region there are 12 fixed points. Two of those disappear through a saddle-node bifurcation. Below this saddle-node bifurcation curve, there are 10 remaining fixed points. At every following saddle-node bifurcation two will disappear. Furthermore, two transcritical bifurcation curves are found, where two equilibria collide and exchange stability. The transcritical bifurcation curves each meet a saddle-node bifurcation curve tangentially in the points SNT1 and IP1. In this figure, both points are a saddle-node-transcritical bifurcation as discussed in section 1.4. However, IP1 is a more degenerate point in the complete model.

The 10 remaining fixed points play an important role for the behavior for  $\alpha_g \neq 0$ . For every of these ten fixed points, there exists another fixed points on the manifold  $\alpha_g = \alpha_g^{nt}$ . For high values of  $x$  all the non-trivial fixed points have  $\alpha_g < 0$ , but for lower values of  $x$  they have  $\alpha_g > 0$ . On the intersection of the two planes, where  $\alpha_g = \alpha_g^{nt} = 0$ , i.e. when  $N_f = \frac{11N_c}{2+3g_V}$ , all non-trivial fixed points collide with a trivial fixed point, through a transcritical bifurcation. Therefore, all non-trivial fixed points can be related to a trivial fixed point. The branching point bifurcation curves at which these collisions happen are shown in figure 2.9.

The 10 non-trivial fixed points with positive  $\alpha_g$  exist for small values of  $x$ . However, they either disappear through a saddle-node bifurcation or diverge in one or multiple couplings, as is shown in figure 2.10. Here, we see that two pairs of fixed points will always disappear through a saddle-node bifurcation. One of these pairs (black line) is connected to the saddle-node bifurcation that was already found in the Veneziano limit. Another pair (black line) will disappear through a saddle-node bifurcation, unless  $N_c \lesssim 2$ , where the fixed points will diverge for small  $x$ . This pair is also connected to the same saddle-node bifurcation in the Veneziano limit<sup>2.6</sup>. A fourth pair disappears through a saddle-node bifurcation when  $1 < N_c < 16$ , diverges for  $N_c \geq 16$ , while at  $N_c = 1$  the fixed points will not exist for positive  $\alpha_g$ .

In this way, one can identify 5 pairs of non-trivial fixed points corresponding to 5 pairs of trivial fixed points. One can verify that between the fixed points within these sets, there exist heteroclinic orbits that have a structure as shown in figure 2.11: at first, for high  $x$ , the two non-trivial fixed points lie below the  $\alpha_g = 0$  plane, and the  $\alpha_g = 0$  plane is locally attractive in the IR limit, then, at a specific value of  $x$ , one of the non-trivial and one of the trivial fixed points collide through a transcritical bifurcation and the non-trivial fixed

<sup>2.6</sup>A second saddle-node bifurcation in the Veneziano limit can be expected with the same values for  $(x, \alpha_g, g_S, g_V)$ , but differing  $(g_{V_1}, g_{V_2})$ , if  $\beta_{g_{V_1}}$  and  $\beta_{g_{V_2}}$  would be considered in the Veneziano limit as well.

point gets a positive  $\alpha_g$  creating a locally attractive IR limit set bounded by orbits between the 3 fixed points with  $\alpha_g \geq 0$ . Next, at lower specific  $x$ , the other non-trivial fixed point will collide with the other trivial fixed point and also get positive  $\alpha_g$  value. After this, at low  $x$ , the non-trivial fixed points will either disappear through a saddle-node bifurcation or diverge, making the  $\alpha_g = 0$  plane locally repulsive in the IR limit. The transcritical and saddle-node bifurcation curves of all those pairs is shown in figure 2.13. The numbers in the plot label the equilibria, which are involved in the bifurcation. The numbers correspond to the numbers in figure 2.12, which shows the stability of the fixed points and the structure of the orbits between the fixed points in the  $\alpha_g = 0$  subspace. Since every fixed point with  $\alpha_g = 0$  is uniquely related to a fixed point at  $\alpha_g = \alpha_g^{nt}$  through a transcritical bifurcation, fixed points within such a pair have been given the same number. Furthermore, a label ‘a’ or ‘b’ is added to every number, such that fixed points with  $\alpha_g = 0$  are labeled with an ‘a’ and fixed points with  $\alpha_g = \alpha_g^{nt}$  with a ‘b’.

In total we find 4 saddle-node bifurcation curves with non-trivial value of  $\alpha_g$ . All four indicate the disappearance of two fixed points when the value of  $x$  is decreased. Along these curves we can identify the eigenvector corresponding to a zero eigenvalue as the relevant operator that crosses marginality. These critical eigenvectors at  $N_c = 3$  are reported in table 3. We have found that these operators are very dependent on  $x$ , but not on  $N_c$ . From the table we conclude that 3 of the saddle-node bifurcation have 2 complex eigenvalues at  $N_c = 3$ , while one has only real eigenvalues. We notice that the normalized eigenvectors corresponding to the complex eigenvalues are all directed along the four-fermi couplings, and have very small contributions ( $|\eta_{\alpha_g}| < 0.007$ ) along the  $e_{\alpha_g}$  direction, meaning that this complex scaling behavior only involves operators, which are linear combinations of the effective four-fermi interactions. Furthermore, we see that the operator crossing marginality is a linear combination of all operators. However the scalar four-fermi interaction is most relevant in three of the saddle-node bifurcations, while in the saddle-node bifurcation of equilibria 5 and the  $V_1$  interaction is most relevant.

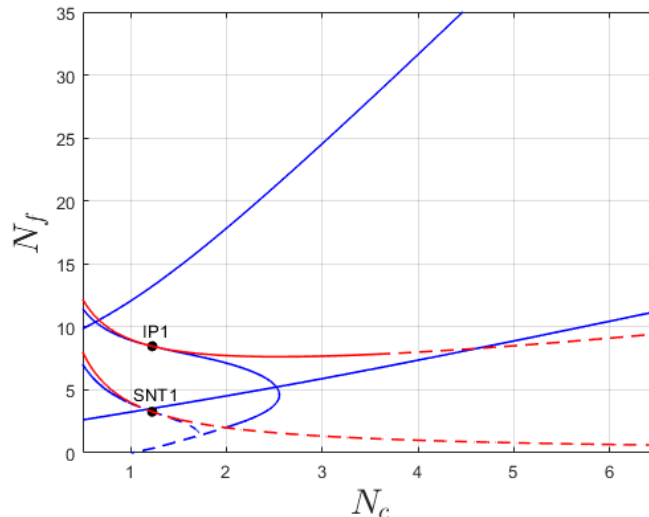


Figure 2.8: Bifurcations of the QCD<sub>4</sub> model (2.6) in the  $\alpha_g^t$  invariant subspace, shown in the  $(N_c, N_f)$ -plane. Blue lines: saddle-node bifurcation curves. Red lines: transcritical bifurcation curves. Dashed lines: bifurcation curves, with at least one of the coupling constants  $|g_i| > 1$ . SNT: Saddle-Node-Transcritical bifurcation. IP: degenerate bifurcation point.

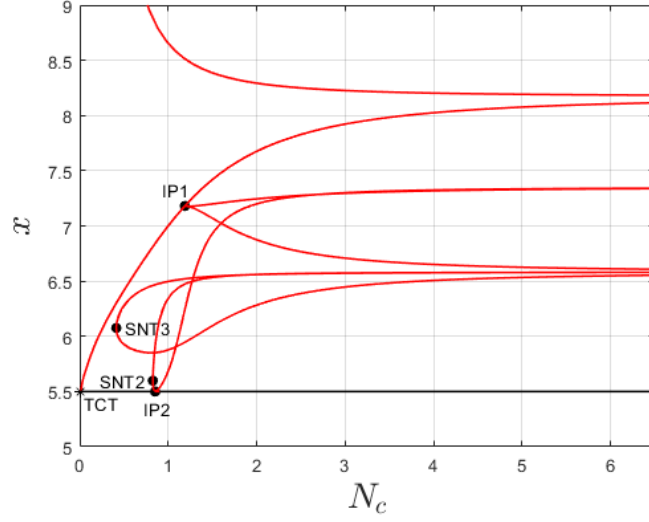


Figure 2.9: Bifurcations on the intersection of the  $\alpha_g = 0$  and  $\alpha_g = \alpha_g^{nt}$  subspaces of the QCD<sub>4</sub> model (2.6), shown in the  $(N_c, x)$ -plane. Red Lines: transcritical bifurcations. Black line: transcritical bifurcation marking the upper edge of the conformal window bifurcation curves. SNT: Saddle-Node-Transcritical bifurcation. TCT: Transcritical-Transcritical bifurcation. IP: degenerate bifurcation point.

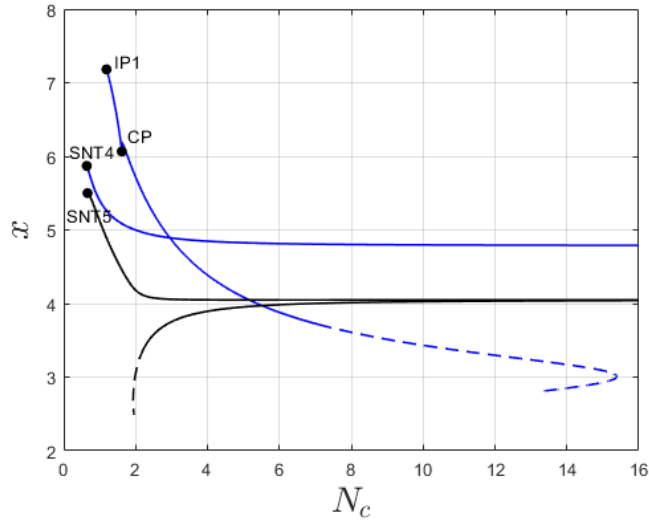


Figure 2.10: Bifurcations of the QCD<sub>4</sub> model (2.6) in the  $\alpha_g = \alpha_g^{nt} \geq 0$  subspace in the  $(N_c, x)$ -plane. Blue lines: saddle-node bifurcations. Black lines: saddle-node bifurcation, that was found in the Veneziano limit. Dashed lines: bifurcation curves, with at least one of the coupling constants  $|g_i| > 1$ . CP: Cusp bifurcation. SNT: Saddle-Node-Transcritical bifurcation. IP: degenerate bifurcation point.

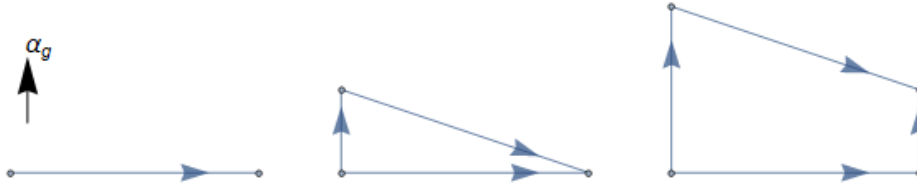


Figure 2.11: Flow structure between 4 fixed points. Left: the 2 non-trivial fixed points have  $\alpha_g < 0$ . Middle: One of the non-trivial fixed points has  $\alpha_g > 0$ . Right: Both of the non-trivial fixed points have  $\alpha_g > 0$ .

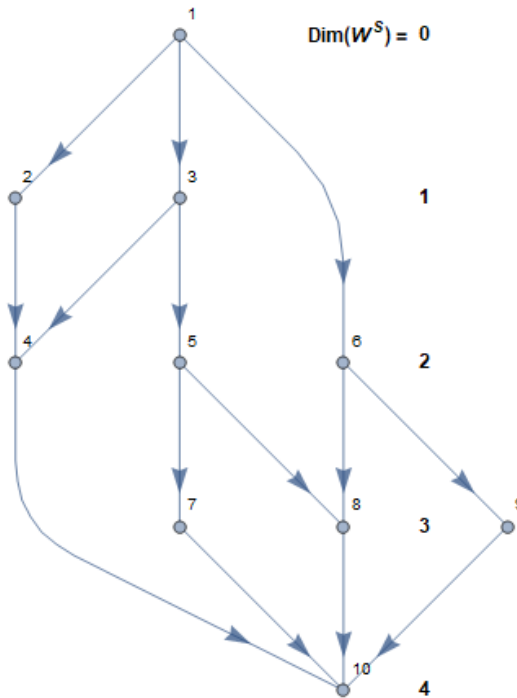
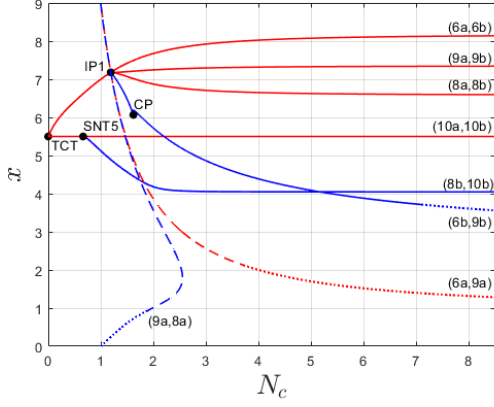


Figure 2.12: Stability of the fixed points and flow structure between the fixed points on the invariant set  $\alpha_g = 0$  at  $(N_c, N_f) = (3, 15)$ .

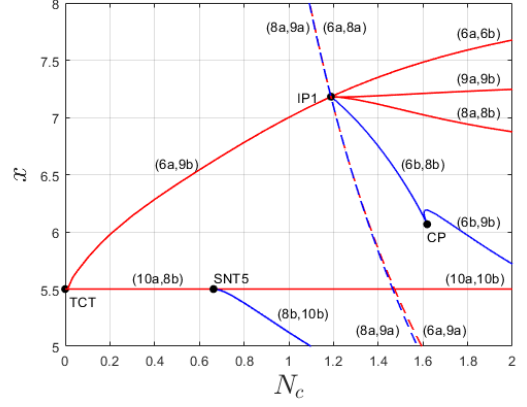
Table 3: Eigenvalues and critical eigenvectors crossing marginality of the saddle-node bifurcation with non-trivial  $\alpha_g$  at  $N_c = 3$ .

Equilibria	$(N_c, x)$	Eigenvalues	Critical eigenvector
8, 10	(3.00, 4.06)	$\{-2.88, -2.10, -1.36, -0.64, 0\}$	(0.12, 0.94, -0.17, 0.12, 0.22)
6, 9	(3.00, 4.86)	$\{-3.62 \pm 0.27i, 1.79, -0.62, 0\}$	(0.11, 0.86, -0.21, 0.35, 0.28)
3, 4	(3.00, 3.75)	$\{3.38 \pm 1.05i, -2.57, -0.81, 0\}$	(0.07, 0.77, -0.08, 0.50, -0.38)
5, 7	(3.00, 4.89)	$\{-1.66 \pm 0.09i, 1.59, -0.27, 0\}$	(0.04, 0.06, -0.07, 0.95, 0.28)

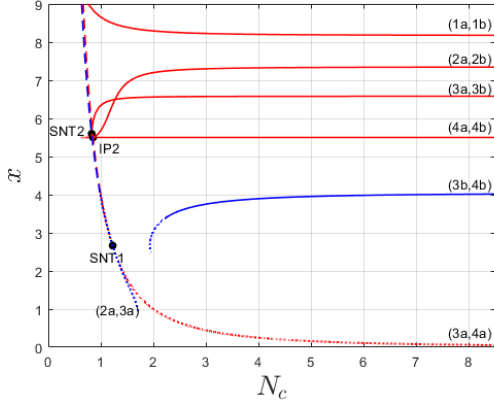
Next, we consider the flow generated by our model (2.3) in the various phases. For this, we set  $N_c = 3$ , and take  $N_f \in \{11, 12, 13, 15\}$ . The flow structure in the invariant  $\alpha_g = 0$  space will be the same for these four values of  $x$ , since there are no bifurcations in this region. Only the location of the fixed points will change continuously. Projections of the fixed points



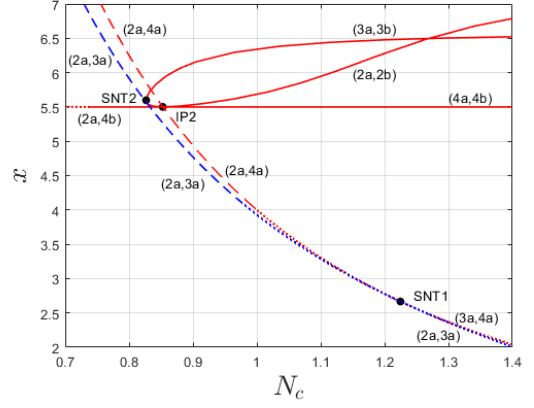
(a) Fixed points 6,8,9,10;  $N_c \in [0, 8.5]$ .



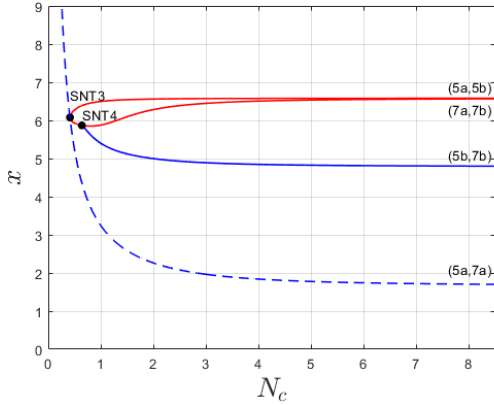
(b) Fixed points 6,8,9,10;  $N_c \in [0, 2]$ .



(c) Fixed points 1,2,3,4;  $N_c \in [0, 8.5]$ .



(d) Fixed points 1,2,3,4;  $N_c \in [0.7, 1.4]$ .



(e) Fixed points 5,7;  $N_c \in [0, 8.5]$ .

Figure 2.13: Bifurcations of various sets of fixed points in the QCD<sub>4</sub> model (2.6) in the  $(N_c, x)$ -plane. Blue solid lines: saddle-node bifurcations in the  $\alpha_g = \alpha_g^{nt}$  subspace. Blue dashed lines: saddle-node bifurcations in the  $\alpha_g = 0$  subspace. Red solid lines: transcritical bifurcations on the intersection of the subspaces,  $\alpha_g = \alpha_g^{nt} = 0$ . Red dashed lines: transcritical bifurcations in the  $\alpha_g = 0$  invariant subspace. Dotted lines: at least one of the coupling constants  $|g_i| > 1$ ; CP: Cusp bifurcation. SNT: Saddle-Node-Transcritical bifurcation. TCT: Transcritical-Transcritical bifurcation. IP: degenerate bifurcation point. Numbers indicate which equilibria are involved in the bifurcation, and correspond to the numbers in figure 2.12.

---

and a few heteroclinic orbits in this 4-dimensional invariant subspace, at  $\alpha_g = 0$ , are shown in figure 2.14. The fixed points and a few heteroclinic orbits in the  $\alpha_g = \alpha_g^{nt}$  subspace are shown in figures 2.15, 2.17, 2.18 and 2.19. In figures 2.16 and 2.20 the flow structure of these figures is shown as a graph.

At  $N_f = 15$ , we see 10 fixed points and a few heteroclinic orbits connecting them, both in the  $\alpha_g = 0$  and the  $\alpha_g = \alpha_g^{nt}$  plane. The red lines shown in the figures form part of a skeleton of a closed set in the 4-dimensional subspaces  $\alpha_g = 0$  and  $\alpha_g = \alpha_g^{nt}$ . These two 4-dimensional sets on  $\alpha_g = 0$  and  $\alpha_g = \alpha_g^{nt}$  form a 4-dimensional boundary of a larger 5-dimensional invariant subspace of the full 5-dimensional space. The other 4-dimensional subspaces which bound the full 5-dimensional invariant set are spanned by orbits going from  $\alpha_g = 0$  towards  $\alpha_g = \alpha_g^{nt}$ . Dashed red lines indicate parts of the skeleton that haven't been found numerically, but are expected to exist. The flow within the 5-dimensional invariant set is everywhere directed from the  $\alpha_g = 0$  towards the  $\alpha_g = \alpha_g^{nt} > 0$  subspace. This set consists of structurally stable renormalized trajectories that have finite UV (with trivial  $\alpha_g$ ) and IR limits (with strictly positive  $\alpha_g$ ) indicating the theory to be in a symmetric phase. Outside the set orbits have diverging IR and/or UV limit, and theories will have a broken chiral symmetry.

When the flavor number is reduced just below  $N_f = 15$ , at  $N_f = 14.7$  and  $N_f = 14.6$ , two pairs of fixed points disappear through a saddle-node bifurcation. Because of these bifurcations, the invariant set of orbits indicating symmetric theories is reduced. However, the most attractive IR fixed point with  $\dim(W^s) = 5$  still exists. This indicates that the invariant set is locally attractive in the IR limit. Reducing the flavor number even further to  $N_f = 12$  and  $N_f = 11$  more fixed points disappear through a saddle-node bifurcations. The invariant set of orbits at  $\alpha_g = \alpha_g^{nt}$  is reduced at every step, and therefore the set of asymptotically stable orbits with finite UV and IR limit becomes smaller, making the set of possible symmetric theories smaller. For  $N_f \leq 12.2$ , there is no fixed point left with  $\dim(W^s) = 5$ . Therefore, the remaining invariant set is not an IR attractor anymore. Furthermore, we expect that the dimension of the invariant set with finite trajectories reduces, when more fixed points have disappeared through a saddle-node bifurcation. When the invariant set splits up into multiple invariant sets with dimension smaller than 5, symmetric theories only exist under extreme fine-tuning, and are therefore unlikely to occur in nature. This is a strong indication that the lower edge of the conformal window has been crossed.

In figure 2.14, there is another peculiarity visible. Here we see a heteroclinic orbit with spiraling behavior indicating the existence of renormalized trajectories with complex scaling behavior in and close to the  $\alpha_g = 0$  plane. Equilibrium 5 and 7 are associated to this behavior.

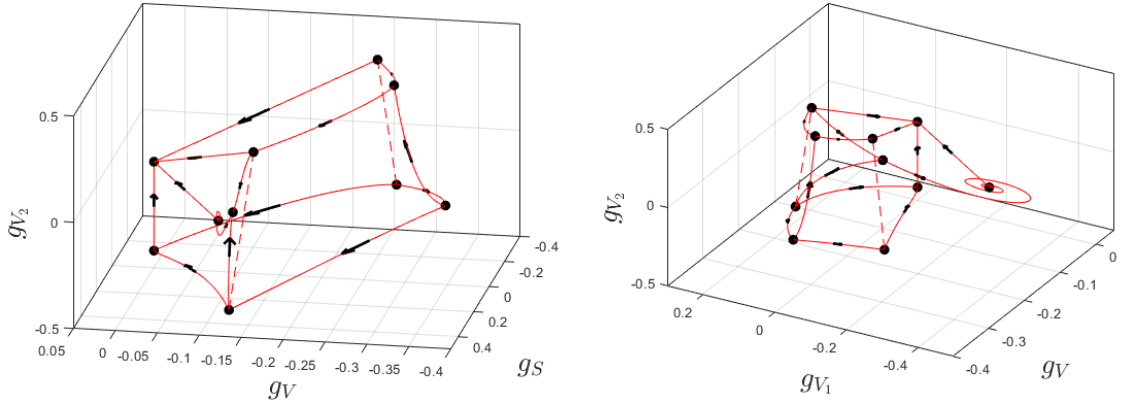


Figure 2.14: Fixed points and a few heteroclinic orbits in the QCD<sub>4</sub> model (2.6) at  $(N_c, N_f) = (3, 15)$  and  $\alpha_g = 0$ . Solid line: heteroclinic connections. Dashed lines: heteroclinic connections that are expected to exist, but haven't been found numerically. Left: projection on the  $(g_S, g_V, g_{V_2})$ -space. Right: projection on the  $(g_V, g_{V_1}, g_{V_2})$ -space.

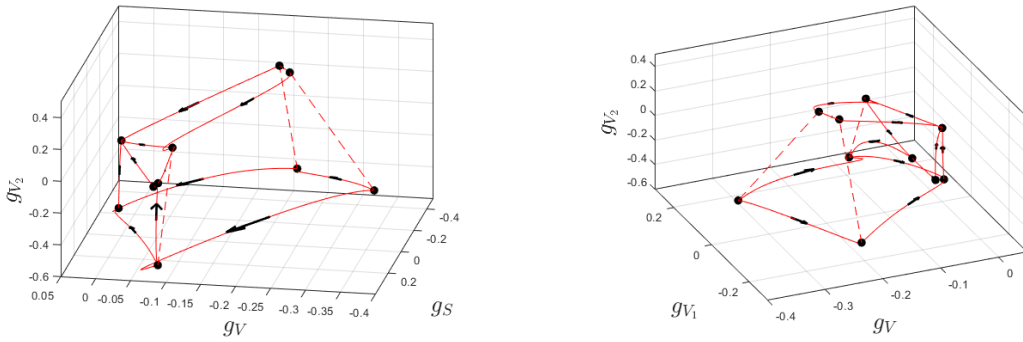
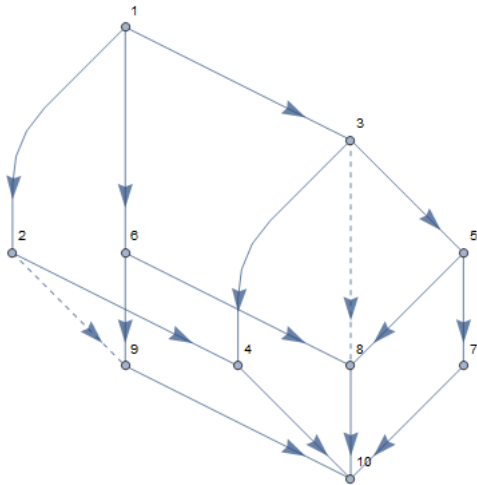
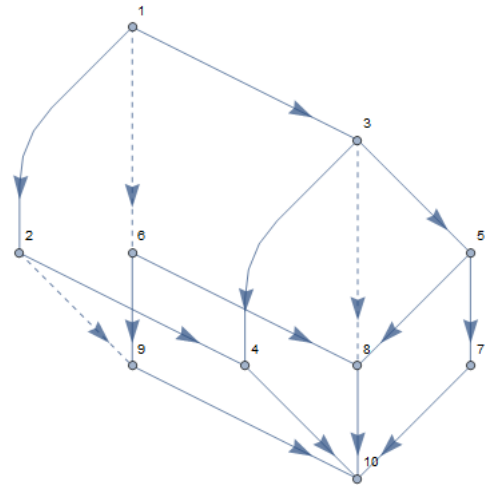


Figure 2.15: Fixed points and heteroclinic orbits in the QCD<sub>4</sub> model (2.6) at  $(N_c, N_f) = (3, 15)$  and  $\alpha_g = \alpha_g^{nt}$ . Solid line: heteroclinic connections. Dashed lines: heteroclinic connections that are expected to exist, but haven't been found numerically. Left: projection on the  $(g_S, g_V, g_{V_2})$ -space. Right: projection on the  $(g_V, g_{V_1}, g_{V_2})$ -space.



(a) Flow structure at  $\alpha_g = 0$  corresponding to fig. 2.14.



(b) Flow structure at  $\alpha_g = \alpha_g^{nt}$  corresponding to fig. 2.15.

Figure 2.16: Graphical representation of the fixed points and the skeleton of the invariant set at  $(N_c, N_f) = (3, 15)$  both on the  $\alpha_g = 0$  and the  $\alpha_g = \alpha_g^{nt}$  subspaces.

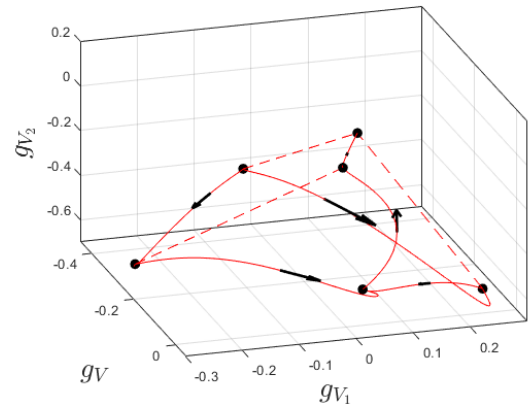
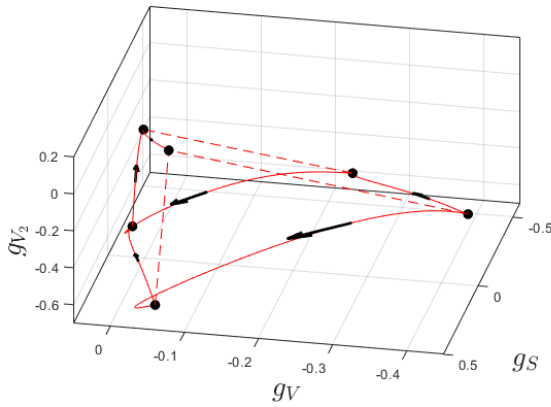


Figure 2.17: Fixed points and heteroclinic orbits of the QCD<sub>4</sub> model (2.6) at  $(N_c, N_f) = (3, 13)$  and  $\alpha_g = \alpha_g^{nt}$ . Solid line: heteroclinic connections. Dashed lines: heteroclinic connections that are expected to exist, but haven't been found numerically. Left: projection on the  $(g_S, g_V, g_{V_2})$ -space. Right: projection on the  $(g_V, g_{V_1}, g_{V_2})$ -space.



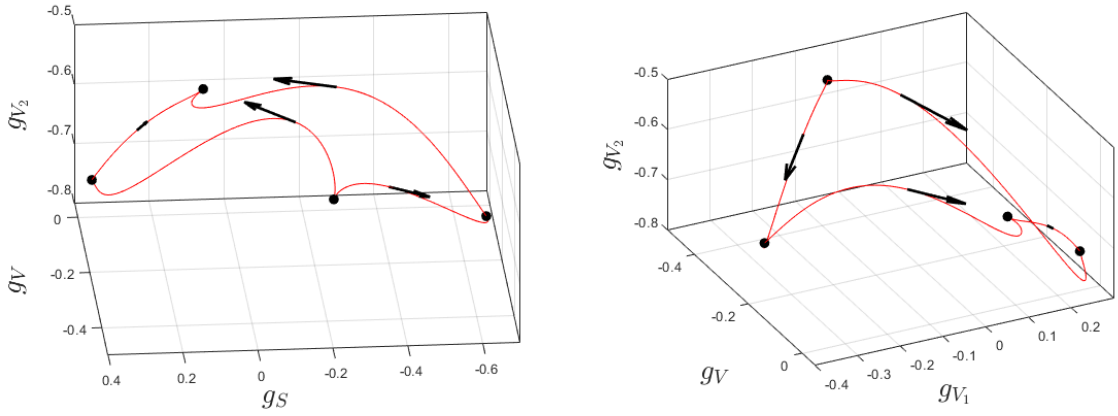


Figure 2.18: Fixed points and heteroclinic orbits of the QCD<sub>4</sub> model (2.6) at  $(N_c, N_f) = (3, 12)$  and  $\alpha_g = \alpha_g^{nt}$ . Left: projection on the  $(g_S, g_V, g_{V_2})$ -space. Right: projection on the  $(g_V, g_{V_1}, g_{V_2})$ -space.

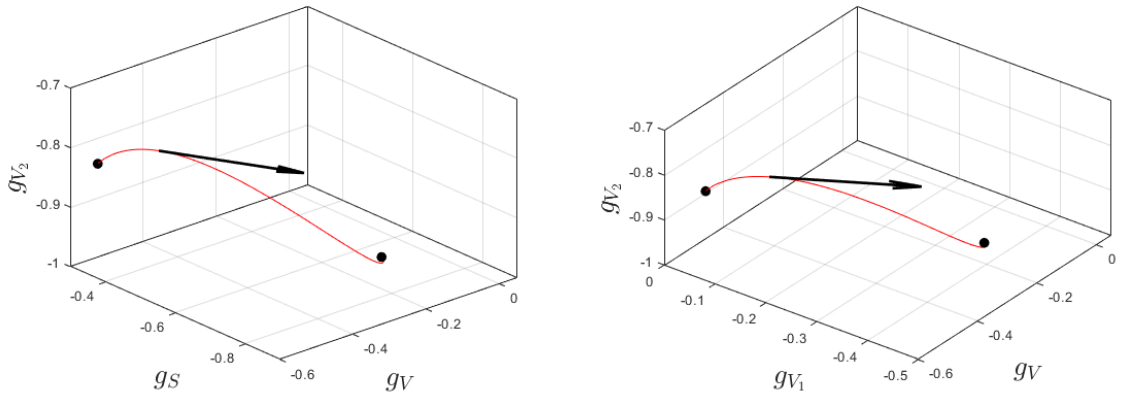


Figure 2.19: Fixed points and heteroclinic orbits of the QCD<sub>4</sub> model (2.6) at  $(N_c, N_f) = (3, 11)$  and  $\alpha_g = \alpha_g^{nt}$ . Left: projection on the  $(g_S, g_V, g_{V_2})$ -space. Right: projection on the  $(g_V, g_{V_1}, g_{V_2})$ -space.

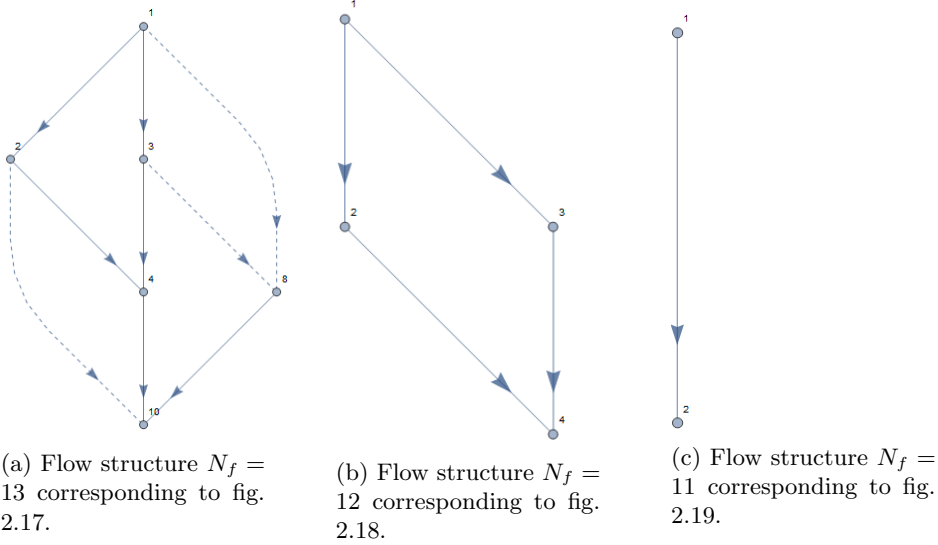


Figure 2.20: Graphical representation of the fixed points and the skeleton of the invariant set on the  $\alpha_g = \alpha_g^{nt}$  subspace at  $N_c = 3$  and various values of  $N_f$ .

## 2.4 Scaling Behavior

In this section<sup>2.7</sup>, we calculate the scaling dimensions of the operators crossing marginality at the bifurcations. This scaling dimension is related to the eigenvalues of the Jacobian indicating the bifurcation. The Jacobian of the normal form, eq. (1.46), with saddle-node bifurcation at  $(\bar{x}, \bar{\alpha})$  is given by  $\pm 2(x - \bar{x})$ , and is equal to the eigenvalue crossing marginality. Furthermore, the equilibria close to the saddle-node bifurcation are given by

$$x = \bar{x} \pm \sqrt{|\alpha - \bar{\alpha}|}. \quad (2.9)$$

Therefore, the eigenvalue of the operator crossing marginality is

$$2(\bar{x} \pm \sqrt{|\alpha - \bar{\alpha}|} - \bar{x}) = \pm 2\sqrt{|\alpha - \bar{\alpha}|}, \quad (2.10)$$

which is equal to the anomalous dimension of the four-fermi interaction that trigger the saddle-node bifurcation:

$$\gamma = \Delta_{4f} - d \approx \pm 2\sqrt{\|(N_c, N_f) - (\bar{N}_c, \bar{N}_f)\|}, \quad (2.11)$$

where we take the standard Euclidean norm.

At the upper edge of the conformal window the phase transition is due to a transcritical bifurcation for which the normal form, eq. (1.48), has Jacobian  $\alpha - \bar{\alpha} \pm 2(x - \bar{x})$ , and the equilibria are given by  $x = \bar{x}$  and  $x = \bar{x} \mp (\alpha - \bar{\alpha})$ . The anomalous dimension of the operator crossing marginality scales linearly:

$$\gamma = \Delta_{4f} - d \approx \pm \|(N_c, N_f) - (\bar{N}_c, \bar{N}_f)\|$$

<sup>2.7</sup>The results derived in this section are in accordance with results in [16] and [30]

Approaching the saddle-node bifurcation from the other side, we find for the energy scales

$$\begin{aligned}
\frac{\Lambda_{UV}}{\Lambda_{IR}} &= e^{t_{IR}-t_{UV}} \\
&= \exp\left(\int_{x_{UV}}^{x_{IR}} \frac{1}{\beta_x} dx\right) \\
&= \exp\left(\int_{x_{UV}}^{x_{IR}} \frac{1}{\alpha - x^2} dx\right), \tag{2.12}
\end{aligned}$$

where we have taken the plus in the normal form (1.46) and  $(\bar{x}, \bar{\alpha}) = (0, 0)$ . When both equilibria have disappeared, we have  $\alpha < 0$  and  $x_{IR} < 0 < x_{UV}$ . Hence,

$$\begin{aligned}
\frac{\Lambda_{UV}}{\Lambda_{IR}} &= \exp\left(\int_{x_{UV}}^{x_{IR}} \frac{1}{\alpha - x^2} dx\right) \\
&= \exp\left(\frac{1}{\alpha} \int_{x_{UV}}^{x_{IR}} \frac{1}{1 - x^2/\alpha} dx\right) \\
&= \exp\left(-\frac{1}{\sqrt{|\alpha|}} \left[ \arctan\left(\frac{x_{IR}}{\sqrt{-\alpha}}\right) - \arctan\left(\frac{x_{UV}}{\sqrt{-\alpha}}\right) \right]\right) \tag{2.13}
\end{aligned}$$

Approaching the bifurcation from negative  $\alpha$ , we can take  $|\alpha| \ll (|x_{IR}|, |x_{UV}|)$ , since  $|\alpha|$  can be taken arbitrarily close to 0, while the coupling constants in the IR and UV limit change discontinuously to 0 at the bifurcation. Taking this limit, we find

$$\frac{\Lambda_{UV}}{\Lambda_{IR}} = \exp\left(\frac{\pi}{\sqrt{|\alpha|}}\right) \tag{2.14}$$

indicating that the energy scales exponentially (i.e. Miransky scaling [30]) close to the bifurcation, which indicates a walking behavior of the fermion mass just below the conformal window. This walking behavior changes continuously to a running behavior further below the conformal window.

## 2.5 Bifurcation Points

In the complete model we have encountered nine bifurcation points with higher codimension. An overview can be found in table 4. Six of these points lie in the physical uninteresting region  $N_c \in (0, 1)$ , while three of them (CP, SNT1 and IP1) may have physical relevance, since  $N_c \geq 1$ .

Table 4: Locations of bifurcations found in the model of QCD<sub>4</sub> (2.8) with effective four-fermi interactions.

Bifurcation	$N_c$	$N_f$	$x$	$\alpha_g$	$g_S$	$g_V$	$g_{V_1}$	$g_{V_2}$
CP	1.62	9.82	6.07	0.05	0.03	-0.17	0.01	0.22
SNT1	1.22	3.27	2.67	0	0	0	0	-1.50
SNT2	0.83	4.63	5.60	0	0.28	-0.01	0.12	-0.82
SNT3	0.41	2.51	6.08	0	0.28	-0.06	-0.02	-0.01
SNT4	0.64	3.76	5.87	0	0.26	-0.04	-0.05	-0.04
SNT5	0.66	3.65	5.50	0	0	0	0	0
TCT	0	0	0	0	0	0	0	0
IP1	1.19	8.54	7.18	0	0	-0.16	0	0.17
IP2	0.85	4.69	5.50	0	0	0	0	-0.73

---

The point labeled with ‘CP’ corresponds to a cusp bifurcation and the points labeled with ‘SNT’ correspond to saddle-node-transcritical bifurcations, as discussed in the introduction. The point ‘TCT’ labels an intersection of two transcritical bifurcation curves. The points ‘IP’ label more degenerate bifurcation points, which will be discussed below.

At the cusp bifurcation 2 saddle-node bifurcation curves with non-trivial value of  $\alpha_g$  meet. The first curve is associated to the pair of equilibria (6b,8b) and the second to (6b,9b), where the number labels the pair as labeled in figure 2.12 and an ‘a’ is used for the trivial equilibrium within the pair and a ‘b’ for the non-trivial equilibrium.

The point SNT1, describes a saddle-node-transcritical bifurcation, of a saddle-node curve that lies in the subspace  $\alpha_g = 0$  and involves the equilibria (2a,3a), and two transcritical curves that also lie in the  $\alpha_g = 0$  subspace and involve the equilibria (2a,4a) and (3a,4a).

The point SNT2, describes a saddle-node-transcritical bifurcation, of a saddle-node curve that lies in the subspace  $\alpha_g = 0$  and involves the equilibria (2a,3a), and two transcritical curves that lie in the  $\alpha_g = \alpha_g^{nt} = 0$  subspace and involve the equilibria (2a,3b) and (3a,3b).

The point SNT3, describes a saddle-node-transcritical bifurcation, of a saddle-node curve that lies in the subspace  $\alpha_g = 0$  and involves the equilibria (5a,7a), and two transcritical curves that lie in the  $\alpha_g = \alpha_g^{nt} = 0$  subspace and involve the equilibria (5a,5b) and (7a,5b).

The point SNT4, describes a saddle-node-transcritical bifurcation, of a saddle-node curve with non-trivial value of  $\alpha_g$  and involves the equilibria (5b,7b), and two transcritical curves that lie in the  $\alpha_g = \alpha_g^{nt} = 0$  subspace and involve the equilibria (7a,5b) and (7a,7b). We notice that only the part of the saddle-node bifurcation with  $\alpha_g > 0$  has been shown in figure 2.13e

The point SNT5, describes a saddle-node-transcritical bifurcation, of a saddle-node curve with non-trivial value of  $\alpha_g$  and involves the equilibria (8b,10b), and two transcritical curves that lie in the  $\alpha_g = \alpha_g^{nt} = 0$  subspace and involve the equilibria (10a,8b) and (10a,10b). We notice that only the part of the saddle-node bifurcation with  $\alpha_g > 0$  has been shown in figure 2.13a and 2.13b

The point TCT describes a degenerate transcritical bifurcation. Reduced to the subspace  $\alpha_g = 0$ , this point is a transcritical bifurcation of two equilibria (6a,10a). However in the full space it is a transcritical bifurcation of the transcritical bifurcation curves of the pairs (6a,9b) and (10a,8b).

IP1 is a highly degenerate bifurcation point. The model reduced on the invariant subspace  $\alpha_g = 0$  has a pitchfork bifurcation at this point. However, in the 5-dimensional model the branches of the equilibrium curves meeting at this pitchfork bifurcation are all transcritical bifurcation curves of the equilibria (6a,6b), (8a,8b), (9a,9b) and (6a,9b). In addition, to this pitchfork bifurcation we find a saddle-node-transcritical bifurcation at this point. The curves associated to this saddle-node-transcritical bifurcation all lie in the  $\alpha_g = 0$  subspace. The saddle-node curve involves the equilibria (8a,9a) and the branches of the transcritical bifurcation involve (6a,8a) and (6a,9a).<sup>2,8</sup> On top of this, there is a saddle-node bifurcation curve with non-trivial  $\alpha_g$  intersecting at this point. This curve involves the equilibria (6b,8b). Together with the branches of transcritical bifurcation curves of (6a,6b) and (8a,8b), that were contained in the pitchfork bifurcation, we could also see this point as saddle-node-transcritical bifurcation of these points. In short this point is highly degenerate

---

<sup>2,8</sup>This is still a bit speculative. We expect the pitchfork bifurcation and the saddle-node-transcritical bifurcation to overlap, but this is hard to verify numerically.

---

and can be unfolded into two saddle-node-transcritical bifurcation and a pitchfork bifurcation of transcritical bifurcation curves.

IP2 is a degenerate bifurcation point, where two transcritical bifurcation curves meet tangentially. Both these curves involve a transcritical bifurcation of a trivial equilibrium with a non-trivial equilibrium. In addition, a transcritical bifurcation curve involving two trivial equilibria intersects the two transcritical bifurcation curves in their intersection point. The equilibria 2a, 2b, 3a, 3b, 4a and 4b are involved in these bifurcation curves.

## 2.6 Discussion of the Results

In the complete model we can distinguish 10 pairs of fixed points, which are relevant to the physics in and below the conformal window. These points can be divided into three different sets:  $\{1, 2, 3, 4\}$ ,  $\{5, 7\}$  and  $\{6, 8, 9, 10\}$ . Here, we used the numbering as in figure 2.12. The first set contains the most repulsive fixed points and is therefore most relevant for the UV limit of the theory, while the last set contains the most attractive fixed points and is therefore most relevant for the IR limit of the theory.

The set of pairs of fixed points  $\{6, 8, 9, 10\}$  consists of points that were already found in the Veneziano limit. The non-trivial points of the pairs 8 and 10 disappear through a saddle-node bifurcation at  $x \approx 4$  for high values of  $N_c$  like in the Veneziano limit. Furthermore, the non-trivial points of the pairs 6 and 9 diverge for  $N_c \geq 16$ , and the trivial points of the pairs 6 and 9 have a transcritical bifurcation at  $x = 1$  for large values of  $N_c$ . This behavior was also found in the Veneziano limit. Equilibrium 10 is the most attractive and the point with non-trivial  $\alpha_g$  in this pair describes the IR limit of the structurally stable renormalized trajectories that exist within the invariant set. We see that like in the Veneziano limit the non-trivial IR point disappears through a saddle-node bifurcation with the non-trivial equilibrium of pair 8 at  $(N_c, x) = (3, 4.06)$  or  $(N_c, N_f) = (3, 12.2)$ . This saddle-node bifurcation is a good candidate for the lower edge of the conformal window in this model. This prediction is higher than but comparable to the predictions summarized in [16]. It coincides, however, with a recent prediction on a similar model including effective interactions [31]. Furthermore, we see that the transcritical bifurcation of the equilibria of pair 10, where the most attractive equilibrium gets a positive  $\alpha_g$  is constant at the ratio  $x = 5.5$ . This line indicates the upper edge of the conformal window, and the same value was found in the Veneziano limit. This is consistent with earlier predictions, as it should be, since it is an exact result which can be derived from the two-loop perturbative beta function of  $\alpha_g$  without four-fermi interactions.

If we take the saddle-node bifurcation of the non-trivial equilibria of the pairs 8 and 10 as the lower edge of the conformal window, we can see in figure 2.13a that the the ratio  $x$ , indicating the lower edge of the conformal window, increases for  $N_c \leq 2$ . Furthermore, we see that the two fixed points that were diverging in the Veneziano limit for low values of  $x$  will disappear through a saddle-node bifurcation for values  $1 < N_c < 16$ . This saddle-node bifurcation takes place for ratios below the conformal window for  $N_c > 5$ , and for  $1 < N_c \leq 5$  it takes place in or above the conformal window, while at  $N_c = 1$  these fixed points don't exist for strictly positive  $\alpha_g$ . This saddle-node bifurcation curve affects the closed invariant set of structurally stable orbits, and could therefore be relevant for the physics in the conformal window. For  $N_c \geq 16$ , we expect similar behavior as in the conformal window, where these two fixed points diverge around  $x \leq 2.5$ . Here, the fixed points form extremal points of a 5-dimensional closed invariant set, which is discontinuously broken down to a smaller invariant set, when the saddle-node bifurcation of the pairs 8 and 10 takes place. For  $5 < N_c < 16$ , the points no longer diverge, but also disappear through a saddle-node bifurcation. However, this happens for a value of  $x$  which is below the lower edge of the

---

conformal window. Therefore, the behavior within the conformal window won't be changed much by this saddle-node bifurcation. In the region  $3 \leq N_c \leq 5$  this saddle-node bifurcation takes place within the conformal window, resulting in a discontinuous change in size of the closed invariant set of structurally stable orbits (or renormalized trajectories with finite IR and UV limit) at the bifurcation. I.e. it doesn't affect the range of the conformal window, but it induces an discontinuous change in the set of symmetric theories, which could indicate a phase transition within the conformal window. At  $N_c = 2$ , the saddle-node bifurcation takes place above the conformal window, and therefore this discontinuous transition won't take place within the conformal window. However, we expect the possible set of symmetric theories in the conformal window to be smaller than at higher values of  $N_c$ . At  $N_c = 1$ , this saddle-node bifurcation only takes place for negative  $\alpha_g$ , but not for positive  $\alpha_g$ . Furthermore, the conformal window has become very small at  $N_c = 1$ .

The set of pairs of fixed points  $\{1, 2, 3, 4\}$  contains the four pairs of fixed points that are the most repulsive of the 10, and are therefore most relevant for the UV physics. Pair 1 is the most repulsive pair and therefore describes the UV limit of the renormalized trajectories within the invariant set of structurally stable orbits. At a curve  $x > 8$  the equilibria within this pair undergo a transcritical bifurcation, as can be seen in figures 2.13c. Below this curve the most repulsive of the pair is the trivial equilibrium making the theory asymptotically free. Above this curve the  $\alpha_g = 0$  plane is repulsive, and therefore the theory always diverges in the UV limit. The non-trivial fixed points of the pairs 1 and 2 both diverge when  $x$  is decreased. Furthermore, we see that two of the non-trivial equilibria, the ones from the pairs 3 and 4, disappear through a saddle-node bifurcation for  $N_c \geq 2$  this bifurcation happens for lower values of  $x$  than the saddle-node bifurcation which we took as the lower edge of the conformal window. We notice however, that this bifurcation curve also converges to  $x \approx 4$  in the Veneziano limit, where the saddle-node bifurcation was found in the Veneziano limit. We find that both this curve and the saddle-node bifurcation curve of the non-trivial fixed points 8 and 10 correspond to the saddle-node bifurcation that was found in the Veneziano limit, since the beta functions for  $g_{V_1}$  and  $g_{V_2}$  have two fixed points at this point indicating that there are actually 2 saddle-node bifurcations in the Veneziano limit, that differ in the values  $g_{V_1}$  and  $g_{V_2}$ . We expect that this the saddle-node bifurcation curve of the non-trivial fixed points of the pairs 3 and 4 is the actual lower edge of the conformal window, since there can still exist a 5-dimensional invariant set of structurally stable orbits between the two saddle-node bifurcation curves, although it is hard to verify this numerically. This set would, however, be repulsive in the IR limit in every direction. If we take the saddle-node bifurcation curve of points 3 and 4 as the lower edge of the conformal window, the saddle-node bifurcation curve would indicate a discontinuous change in the invariant set of structurally stable orbits indicating the symmetric theories. Furthermore, this would imply that the lower edge of the conformal window is just below  $N_f = 12$  at  $N_c = 3$ , as was found in lattice studies such as [33], and as a theoretical prediction in [34].

Finally, we notice that there is a last set of two pairs of fixed points,  $\{5, 7\}$ , which weren't found in the Veneziano limit. These fixed points have complex eigenvalues with relatively large complex part compared to the real part. This induces a spiraling behavior in the system. These points disappear through a saddle-node bifurcation both on the  $\alpha_g = \alpha_g^{nt}$  and the  $\alpha_g = 0$  subspace. Through their complex scaling behavior they induce exotic flow behavior in and below the conformal window, which completely disappears when the ratio  $x$  becomes small enough. These fixed points might have a physical interpretation or might be a consequence of the approximate nature of our model. Furthermore, the other fixed points (except for the pairs 8 and 10) can have complex eigenvalues, but for those the complex part is smaller than the real part, making the spiraling behavior less visible. Also, the eigenvectors corresponding to the complex eigenvalues are largely directed into the direction of the effective four-fermi couplings.

### 3 QCD<sub>4</sub> with a Scalar Field

In this section we extend our previous model with a meson-like scalar field  $\Phi$  that couples to the fermion fields with the coupling constant  $y$ , to see how this affects the model. The field  $\Phi$  is invariant under  $SU(N_c)$  and transforms in the adjoint representation of  $SU(N_f)_L \times SU(N_f)_R$ , i.e. as  $\Phi \rightarrow g_L \Phi g_R^\dagger$ , where  $g_i \in SU(N_f)_i$ . This extension is based on an extension mentioned in [31]. The Lagrangian is extended with a massless scalar field and a Yukawa coupling with the fermion fields yielding extra terms in the Lagrangian:

$$\delta\mathcal{L} = \frac{1}{2} \partial_\mu \Phi \partial^\mu \Phi - y \sum_{i,j=1}^{N_f} (\bar{L}_i \Phi_j^i R^j + \bar{R}_i (\Phi^\dagger)_j^i L^j). \quad (3.1)$$

The beta functions system of beta functions is then extended to a system of 6 differential equations in 6 variables and 2 parameters, which is calculated in appendix D,

$$\left\{ \begin{array}{l} \Lambda \frac{d\alpha_g}{d\Lambda} = -\frac{2}{3}(11N_c - 2N_f)\alpha_g^2 - \frac{2}{3} \left( 34N_c^2 - 13N_cN_f + 3\frac{N_f}{N_c} \right) \alpha_g^3 - 2N_f^2\alpha_y\alpha_g^2 + 2N_cN_fg_V\alpha_g^2, \\ \Lambda \frac{d\alpha_y}{d\Lambda} = 2\alpha_y \left( 2N_c\alpha_y + N_f\alpha_y - 3 \left( N_c - \frac{1}{N_c} \right) \alpha_g - 2N_cg_S + 8g_{V_1} \right), \\ \Lambda \frac{dg_S}{d\Lambda} = 2(1 + \alpha_y)g_S - 2N_cg_S^2 + 2N_fg_Sg_V + 6g_Sg_{V_1} + 2g_Sg_{V_2} + 4g_V\alpha_y \\ \quad - 6 \left( N_c - \frac{1}{N_c} \right) g_S\alpha_g + 12g_{V_1}\alpha_g - \frac{3}{2} \left( 3N_c - \frac{8}{N_c} \right) \alpha_g^2, \\ \Lambda \frac{dg_V}{d\Lambda} = 2(1 + \alpha_y)g_V + \frac{N_f}{4}g_S^2 + (N_c + N_f)g_V^2 - 6g_Vg_{V_2} - \frac{6}{N_c}g_V + g_S\alpha_y \\ \quad + 6g_{V_2}\alpha_g - \frac{3}{4} \left( N_c - \frac{8}{N_c} \right) \alpha_g^2, \\ \Lambda \frac{dg_{V_1}}{d\Lambda} = 2(1 + \alpha_y)g_{V_1} - \frac{1}{4}g_S^2 - g_Sg_V - 3g_{V_1}^2 - N_fg_Sg_{V_2} + 2(N_c + N_f)g_Vg_{V_1} \\ \quad + 2(N_cN_f + 1)g_{V_1}g_{V_2} - 2g_{V_2}\alpha_y + 2\alpha_y^2 + \frac{6}{N_c}g_{V_1}\alpha_g + \frac{3}{4} \left( 1 + \frac{4}{N_c^2} \right) \alpha_g^2, \\ \Lambda \frac{dg_{V_2}}{d\Lambda} = 2(1 + \alpha_y)g_{V_2} - 3g_V^2 - N_cN_fg_{V_1}^2 + (N_cN_f - 2)g_{V_2}^2 - N_fg_Sg_{V_1} \\ \quad + 2(N_c + N_f)g_Vg_{V_2} - 2g_{V_1}\alpha_y + 2\alpha_y^2 + 6g_V\alpha_g - \frac{6}{N_c}g_{V_2}\alpha_g - \frac{3}{4} \left( 3 + \frac{4}{N_c^2} \right) \alpha_g^2, \end{array} \right. \quad (3.2)$$

where we have defined  $\alpha_y = \frac{y^2}{(4\pi)^2}$ . We rescale the couplings as in (2.4), together with the rescaling  $N_c\alpha_y \rightarrow \alpha_y$ , and we define the ratio  $x := \frac{N_f}{N_c}$ , and  $N := N_c$ . We find

$$\left\{ \begin{array}{l} \Lambda \frac{d\alpha_g}{d\Lambda} = -\frac{2}{3}(11 - 2x)\alpha_g^2 - \frac{2}{3}(34 - 13x)\alpha_g^3 - 2x^2\alpha_y\alpha_g^2 + 2xg_V\alpha_g^2 \\ \quad + N^{-2}(-2x\alpha_g^3), \\ \Lambda \frac{d\alpha_y}{d\Lambda} = 2(2 + x)\alpha_y^2 - 6\alpha_y\alpha_g - 4g_S\alpha_y \\ \quad + N^{-2}(6\alpha_y\alpha_g + 16g_{V_1}\alpha_y), \\ \Lambda \frac{dg_S}{d\Lambda} = 2g_S - 2g_S^2 + 2xg_Sg_V - 6g_S\alpha_g - \frac{9}{2}\alpha_g^2 \\ \quad + N^{-1}(2g_S\alpha_y + 4g_V\alpha_y) + N^{-2}(6g_Sg_{V_1} + 2g_Sg_{V_2} + 6g_S\alpha_g + 12g_{V_1}\alpha_g + 12\alpha_g^2), \\ \Lambda \frac{dg_V}{d\Lambda} = 2g_V + \frac{1}{4}xg_S^2 + (1 + x)g_V^2 - \frac{3}{4}\alpha_g^2 \\ \quad + N^{-1}(2g_V\alpha_y + g_S\alpha_y) + N^{-2}(-6g_Vg_{V_2} - 6g_V\alpha_g + 6g_{V_2}\alpha_g + 6\alpha_g^2), \\ \Lambda \frac{dg_{V_1}}{d\Lambda} = 2g_{V_1} - \frac{1}{4}g_S^2 - g_Sg_V - xg_Sg_{V_2} + 2(1 + x)g_Vg_{V_1} + 2xg_{V_1}g_{V_2} + 2\alpha_y^2 + \frac{3}{4}\alpha_g^2 \\ \quad + N^{-1}(2g_{V_1}\alpha_y - 2g_{V_2}\alpha_y) + N^{-2}(-3g_{V_1}^2 + 2g_{V_1}g_{V_2} + 6g_{V_1}\alpha_g + 3\alpha_g^2), \\ \Lambda \frac{dg_{V_2}}{d\Lambda} = 2g_{V_2} - 3g_V^2 - xg_{V_1}^2 + xg_{V_2}^2 - xg_Sg_{V_1} + 2(1 + x)g_Vg_{V_2} + 6g_V\alpha_g + 2\alpha_y^2 - \frac{9}{4}\alpha_g^2 \\ \quad + N^{-1}(2g_{V_2}\alpha_y - 2g_{V_1}\alpha_y) + N^{-2}(-2g_{V_2}^2 - 6g_{V_2}\alpha_g - 3\alpha_g^2). \end{array} \right. \quad (3.3)$$

### 3.1 The Veneziano Limit

We can take the Veneziano limit ( $N \rightarrow \infty$ ), which yields

$$\begin{cases} \Lambda \frac{d\alpha_g}{d\Lambda} = -\frac{2}{3}(11-2x)\alpha_g^2 - \frac{2}{3}(34-13x)\alpha_g^3 - 2x^2\alpha_y\alpha_g^2 + 2xg_V\alpha_g^2, \\ \Lambda \frac{d\alpha_y}{d\Lambda} = 2(2+x)\alpha_y^2 - 6\alpha_y\alpha_g - 4g_S\alpha_y, \\ \Lambda \frac{dg_S}{d\Lambda} = 2g_S - 2g_S^2 + 2xg_Sg_V - 6g_S\alpha_g - \frac{9}{2}\alpha_g^2, \\ \Lambda \frac{dg_V}{d\Lambda} = 2g_V + \frac{1}{4}xg_S^2 + (1+x)g_V^2 - \frac{3}{4}\alpha_g^2, \\ \Lambda \frac{dg_{V_1}}{d\Lambda} = 2g_{V_1} - \frac{1}{4}g_S^2 - g_Sg_V - xg_Sg_{V_2} + 2(1+x)g_Vg_{V_1} + 2xg_{V_1}g_{V_2} + 2\alpha_y^2 + \frac{3}{4}\alpha_g^2, \\ \Lambda \frac{dg_{V_2}}{d\Lambda} = 2g_{V_2} - 3g_V^2 - xg_{V_1}^2 + xg_{V_2}^2 - xg_Sg_{V_1} + 2(1+x)g_Vg_{V_2} + 6g_V\alpha_g + 2\alpha_y^2 - \frac{9}{4}\alpha_g^2. \end{cases} \quad (3.4)$$

The first 4 equations decouple from the last two and we can reduce analysis to

$$\begin{cases} \Lambda \frac{d\alpha_g}{d\Lambda} = -\frac{2}{3}(11-2x)\alpha_g^2 - \frac{2}{3}(34-13x)\alpha_g^3 - 2x^2\alpha_y\alpha_g^2 + 2xg_V\alpha_g^2, \\ \Lambda \frac{d\alpha_y}{d\Lambda} = 2(2+x)\alpha_y^2 - 6\alpha_y\alpha_g - 4g_S\alpha_y, \\ \Lambda \frac{dg_S}{d\Lambda} = 2g_S - 2g_S^2 + 2xg_Sg_V - 6g_S\alpha_g - \frac{9}{2}\alpha_g^2, \\ \Lambda \frac{dg_V}{d\Lambda} = 2g_V + \frac{1}{4}xg_S^2 + (1+x)g_V^2 - \frac{3}{4}\alpha_g^2. \end{cases} \quad (3.5)$$

The domain of the variables and parameters is given by  $x \in \mathbb{R}^+$ ,  $\alpha_g, \alpha_y \in \mathbb{R}_0^+$  and  $g_S, g_V \in \mathbb{R}$ . Due to the approximate nature of the model (3.3), we expect good results for small parameter values. As a rough bound on the size of the parameters, we'll use  $\alpha_i < 1$ ,  $|g_i| < 1$ .

The beta function for  $\alpha_g$  has a double root for  $\alpha_g^t = 0$  and another root for  $\alpha_g^{nt} = \frac{11-2x+3x^2\alpha_y-3xg_V}{13x-34}$ . Therefore, the fixed points of the RG-flow lie on these manifolds. The manifold defined by  $\alpha_g = 0$  is an invariant set of the system, since  $\dot{\alpha}_g$  vanishes for  $\alpha_g = 0$ .

In addition, the beta function for  $\alpha_y$  has a root for  $\alpha_y^t = 0$  and another root for  $\alpha_y^{nt} = \frac{3\alpha_g+2g_S}{2+x}$ . Therefore, the fixed points of the RG-flow lie on these manifolds. The manifold defined by  $\alpha_y = 0$  is an invariant set of the system, since  $\dot{\alpha}_y$  vanishes for  $\alpha_y = 0$ .

The behavior of the fixed points projected on the  $(x, \alpha_g)$ -plane,  $(x, \alpha_y)$ -plane,  $(x, g_S)$ -plane and the  $(x, g_V)$ -plane is shown in figure 3.1, and the projections on the  $(x, \alpha_g, \alpha_y)$ -space,  $(x, \alpha_g, g_S)$ -space,  $(x, \alpha_g, g_V)$ -space,  $(x, \alpha_y, g_S)$ -space,  $(x, \alpha_g, g_V)$ -space and the  $(x, g_S, g_V)$ -space in figure 3.2. Here, we use the following color coding:

- Solid red line: stable node, 4 negative eigenvalues.
- Dashed red line: saddle point, 3 negative and 1 positive eigenvalue.
- Dashed green line: saddle point, 2 negative and 2 positive eigenvalues.
- Dashed blue line: saddle point, 1 negative and 3 positive eigenvalues.
- Solid blue line: unstable node, 4 positive eigenvalues.

The equilibria on the  $\alpha_g = 0$  manifold all have a trivial eigenvalue, and therefore do not fit the color coding as described above. In order to use the color coding, we define the sign of a trivial eigenvalue on this manifold by approaching the equilibrium along a line of constant  $\alpha_y, g_S$  and  $g_V$  from positive but small  $\alpha_g$ . The trivial eigenvalue will then approach 0 from either positive or negative values. If the trivial eigenvalue is slightly positive for  $0 < \alpha_g \ll 1$ , we define the trivial eigenvalue to be positive and vice versa.

Since  $\beta_{\alpha_y} = 0$  if  $\alpha_y = 0$ , we find the same fixed points and bifurcations as in the previous model without scalar field. In addition, we now find five fixed points with non-trivial value



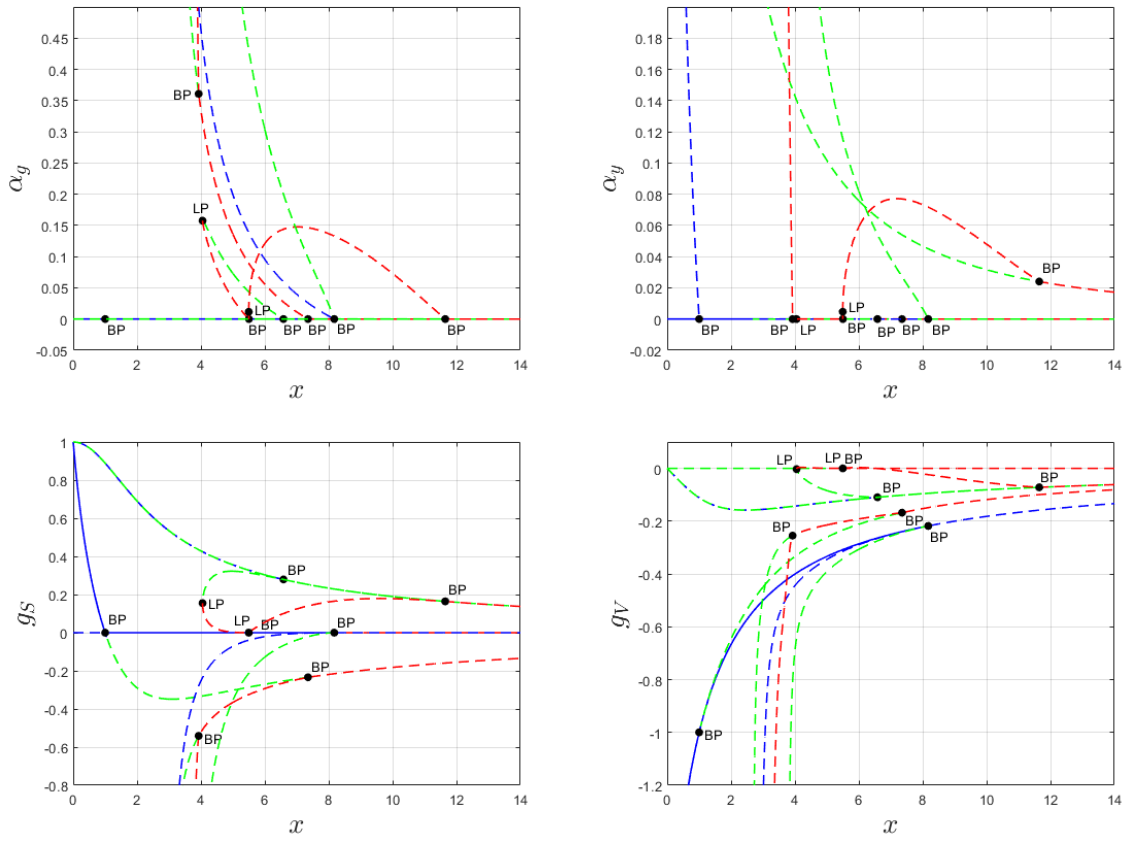


Figure 3.1: The equilibria of the RG-flow of (3.5) projected on the  $(x, \alpha_g)$ -plane,  $(x, \alpha_y)$ -plane,  $(x, g_S)$ -plane and the  $(x, g_V)$ -plane. Solid red line: stable node. Dashed red line: saddle with 1 positive eigenvalue. Dashed green line: saddle with 2 positive eigenvalues. Dashed blue line: saddle with 3 positive eigenvalues. Solid blue line: unstable node. LP: Limit Point. BP: Branching Point.

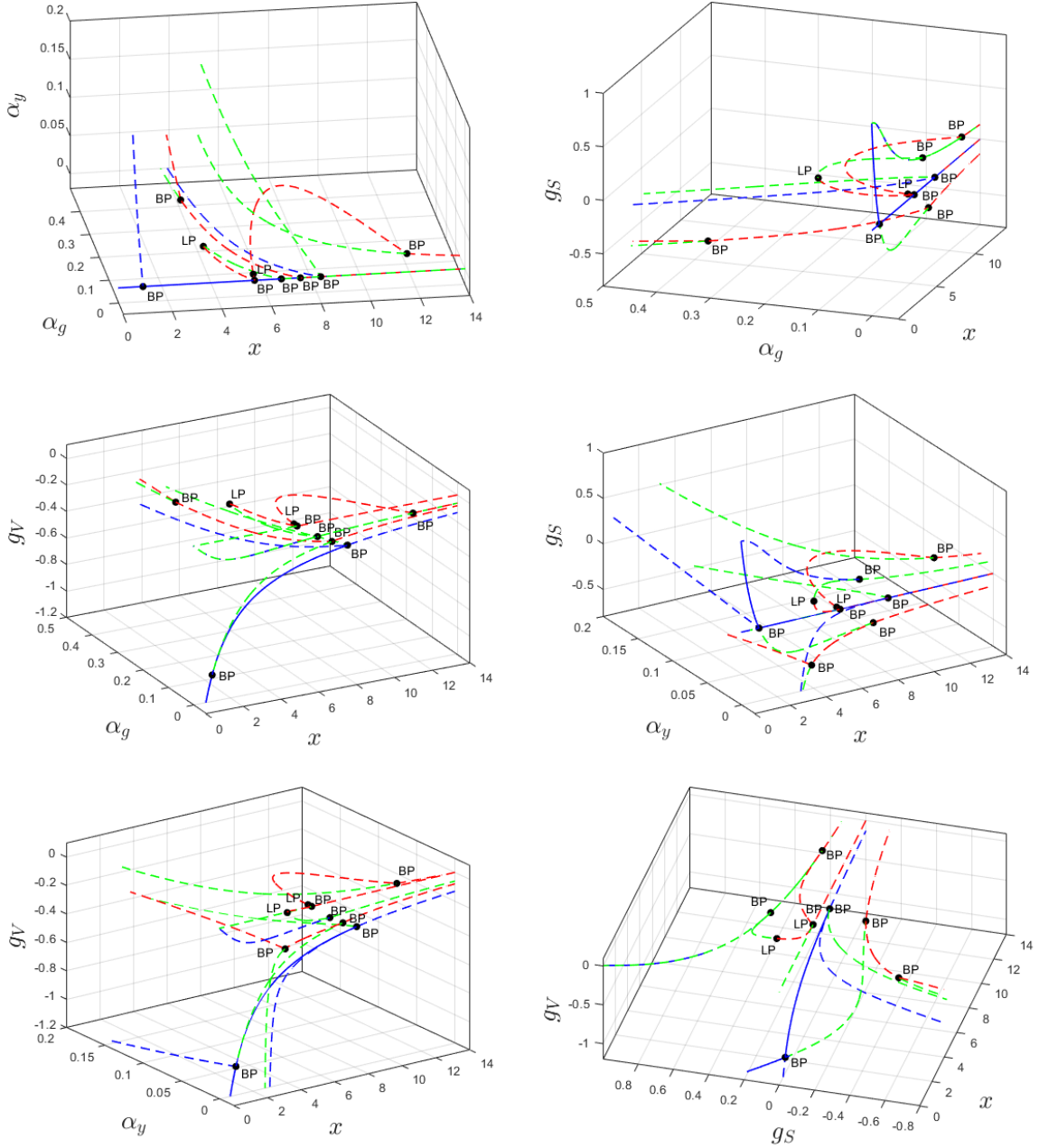


Figure 3.2: The equilibria of the RG-flow of (3.5) projected on the  $(x, \alpha_g, \alpha_y)$ -space,  $(x, \alpha_g, g_S)$ -space,  $(x, \alpha_g, g_V)$ -space,  $(x, \alpha_y, g_S)$ -space,  $(x, \alpha_y, g_V)$ -space and the  $(x, g_S, g_V)$ -space. Solid red line: stable node. Dashed red line: saddle with 1 positive eigenvalue. Dashed green line: saddle with 2 positive eigenvalues. Dashed blue line: saddle with 3 positive eigenvalues. Solid blue line: unstable node. LP: Limit Point. BP: Branching Point.

of  $\alpha_y$ . We find two additional branching points and one additional limit point, as can be seen in table 5. Furthermore, at 3 transcritical bifurcations, that were found in the  $\alpha_y = 0$  model, we now find three equilibria that intersect and exchange stability, corresponding to the normal form

$$\begin{cases} \dot{\tilde{x}} = \tilde{\alpha}\tilde{x} + \tilde{x}^2, \\ \dot{\tilde{y}} = \tilde{\alpha}\tilde{y} + \tilde{y}^2. \end{cases} \quad (3.6)$$

One of the additional fixed points branches off at the transcritical bifurcation at  $x = 1.000$  that was already found in the model without a scalar, and diverges rapidly in  $\alpha_y$ . In addition, one new fixed point branches off from one of the equilibria with non-trivial value of  $\alpha_g$  at  $x = 3.926$ , which also diverges rapidly in  $\alpha_y$ . Furthermore, at the branching point at  $x = 8.173$ , an extra fixed point branches off with a non-trivial value of  $\alpha_g$  and  $\alpha_y$ , which diverges when  $x$  is lowered towards  $x \approx 4$ . Another new fixed point with non-trivial  $\alpha_y$  exists in the scalar model. For this point  $\alpha_y \rightarrow 0$  if  $x \rightarrow \infty$  and  $\alpha_y \rightarrow \infty$  when  $x$  is lowered towards  $x \approx 2$ . From this point another fixed point branches off at  $x = 11.647$ . This point disappears through a saddle-node bifurcation at  $x = 5.497$ . The other point that disappears at this saddle-node bifurcation branches off at  $x = 5.5$  from the trivial fixed point  $(\alpha_g, \alpha_y, g_S, g_V) = (0, 0, 0, 0)$ . This point is the stable node in the system. This stable node disappears through a saddle-node bifurcation at  $5.497$ . We therefore find a conformal window with non-trivial for  $\alpha_y$  at  $x \in [5.497, 5.501]$ , which is slightly smaller than a prediction on a model without effective four-fermi interactions, where  $x \in (5.24, 5.5)$  [31].

Table 5: Locations of bifurcations found in the Veneziano limit of QCD<sub>4</sub> with a scalar field (3.5).

Bifurcation	$x$	$\alpha_g$	$\alpha_y$	$g_S$	$g_V$
Saddle-node	4.049	0	0.158	0.155	-0.003
Saddle-node	5.497	0.012	0.005	0	0
Transcritical	1.000	0	0	0	-1.000
Transcritical	3.926	0.361	0	-0.541	-0.255
Transcritical	5.501	0	0	0	0
Transcritical	6.582	0	0	0.279	-0.110
Transcritical	7.351	0	0	-0.234	-0.168
Transcritical	8.173	0	0	0	-0.218
Transcritical	11.647	0	0.024	0.164	-0.072

### 3.2 The Complete Model

In this section, we analyze the complete model (3.3) outside the Veneziano limit. The beta function for  $\alpha_g$  has two roots:

$$\alpha_g = 0, \quad \alpha_g = \alpha_g^{nt} := N_c \frac{-11N_c^2 + 2N_c N_f - 3N_f^2 \alpha_y + 3N_c N_f g_V}{34N_c^3 - 13N_c^2 N_f + 3N_f},$$

where the trivial root has multiplicity 2. The trivial root makes the  $\alpha_g = 0$  plane an invariant set of the model (3.3). The beta function for  $\alpha_y$  also has two roots:

$$\alpha_y = 0, \quad \alpha_y = \alpha_y^{nt} := \frac{N_c^2(3\alpha_g + 2g_S) - (3\alpha_g + 8g_{V_1})}{N_c(2 + N_f)}.$$

The trivial root makes the  $\alpha_y = 0$  plane an invariant set of the model (3.3). Since  $\alpha_y = 0$  is an invariant plane, we find the exact same bifurcations as in previous section. However, on top of those, there exist fixed points and bifurcations in the  $\alpha_y \neq 0$  space. We find up to six

fixed points with  $\alpha_g, \alpha_y \neq 0$  and up to six fixed points with  $\alpha_g = 0, \alpha_y \neq 0$ , depending on the values of  $(N_c, x)$ . As in the previous section, we find that fixed points with non-trivial  $\alpha_g$  always collide on the intersection  $\alpha_g^{nt} = 0$  with a fixed point with trivial value  $\alpha_g = 0$  through a transcritical bifurcation. This happens at

$$N_f = N_c \frac{2 + 3g_V \pm \sqrt{(2 + 3g_V)^2 - 132\alpha_y}}{6\alpha_y} \quad \text{or} \quad \alpha_y = 0, N_f = N_c \frac{11}{2 + 3g_V},$$

where the second condition is a reduction to the model without scalar field. Similarly, fixed points with non-trivial  $\alpha_y$  always collide on the intersection  $\alpha_y^{nt} = 0$  with a fixed point with trivial value  $\alpha_y = 0$  through a transcritical bifurcation. This happens at

$$N_c = \pm \sqrt{\frac{3\alpha_g + 8g_{V_1}}{3\alpha_g + 2g_S}} \quad \text{or} \quad g_S = -\frac{3}{2}\alpha_g, g_{V_1} = -\frac{3}{8}\alpha_g,$$

where only the positive root is a physically relevant solution. In this way, one can relate most fixed points with  $(\alpha_g > 0, \alpha_y > 0)$  to a fixed point with  $(\alpha_g = 0, \alpha_y > 0)$ , a fixed point with  $(\alpha_g > 0, \alpha_y = 0)$  and a fixed point with  $(\alpha_g = 0, \alpha_y = 0)$ . We find that the orbits between these points are always as indicated in figure 3.3. Furthermore, a non-trivial fixed point<sup>3.1</sup> with positive  $\alpha_g$  and  $\alpha_y$  can appear through a transcritical bifurcation at  $(\alpha_g = \alpha_g^{nt} = 0, \alpha_y > 0)$ , at  $(\alpha_g > 0, \alpha_y = \alpha_y^{nt} = 0)$  or at  $(\alpha_g = \alpha_g^{nt} = 0, \alpha_y = \alpha_y^{nt} = 0)$ . These transcritical bifurcation curves are shown in figure 3.4 by dash-dotted red lines, dash-dotted black lines and solid red lines respectively. When  $x$  decreases non-trivial fixed points will either diverge in one or multiple couplings or disappear through a saddle-node bifurcation with another fixed point. We find three saddle-node bifurcation curves with  $(\alpha_g \neq 0, \alpha_y \neq 0)$  as shown in figure 3.4a, 3.4b and 3.4c. They're shown together with the related<sup>3.2</sup> saddle-node bifurcation curves that were found for  $\alpha_y = 0$  in the previous section. In addition, a saddle-node bifurcation curve with  $(\alpha_g = 0, \alpha_y = 0)$  related to the saddle-node bifurcation in figure 3.4c is shown.

Figure 3.4a shows the bifurcations of the sets of fixed points which were indicated as pairs 8 and 10 in the previous section. Here, we see the transcritical and saddle-node bifurcations that were found in the previous section. In addition, there is now an extra transcritical bifurcation at the solid red line, where a non-trivial fixed point branches of. The solid red line converges to the branching point at  $x = 5.5$  that was found in the Veneziano limit. Furthermore, we see a transcritical bifurcation at non-trivial value of  $\alpha_y$  (dash-dotted red line), where a non-trivial fixed point splits of. This transcritical bifurcation converges to the branching point found at  $x = 11.6$  in the Veneziano limit. The two non-trivial fixed points disappear through a saddle-node bifurcation at the solid blue line, which is related to the blue dashed line representing the saddle-node bifurcation that was found in the  $\alpha_y = 0$  space. The solid blue line converges to limit point that was found at  $x = 5.5$  in the Veneziano limit.

Figure 3.4b shows the bifurcations of the sets of fixed points which were indicated by the pairs 3 and 4 in the previous section. Here, we see the transcritical and saddle-node bifurcations that were found in the previous section. In addition, there is now an extra transcritical bifurcation at the solid red line, where a non-trivial fixed point branches of. The solid red line converges to the branching point at  $x = 5.5$  that was found in the Veneziano limit. Furthermore, we see a transcritical bifurcation at non-trivial value of  $\alpha_y$  (dash-dotted red line), where a non-trivial fixed point splits of. This transcritical bifurcation converges to the branching point found at  $x = 11.6$  in the Veneziano limit. The two non-trivial fixed points

<sup>3.1</sup>We call a fixed point non-trivial if  $(\alpha_g \neq 0, \alpha_y \neq 0)$

<sup>3.2</sup>We say that saddle-node bifurcation curves with  $(\alpha_g > 0, \alpha_y > 0)$  and  $(\alpha_g > 0, \alpha_y = 0)$  or  $(\alpha_g = 0, \alpha_y > 0)$  are related, if the equilibria that are involved can be related through a transcritical bifurcation in the  $\alpha_g = \alpha_g^{nt} = 0$  or  $\alpha_y = \alpha_y^{nt} = 0$  subspace.

---

disappear through a saddle-node bifurcation at the solid blue line, which is related to the blue dashed line representing the saddle-node bifurcation that was found in the  $\alpha_y = 0$  space. The solid blue line converges to limit point that was found at  $x = 5.5$  in the Veneziano limit.

Figure 3.4c shows the bifurcations of the sets of fixed points which were indicated by the pairs 6 and 9 in the previous section. Here, we see the transcritical and saddle-node bifurcations that were found in the previous section. In addition there is now an extra transcritical bifurcation at the solid red line, where a non-trivial fixed point branches of. The solid red line converges to the branching point at  $x = 7.4$  that was found in the Veneziano limit. Furthermore, we see a transcritical bifurcation at non-trivial value of  $\alpha_g$  (dash-dotted black line), where a non-trivial fixed point splits of. This transcritical bifurcation diverges in the Veneziano limit. The two non-trivial fixed points disappear through a saddle-node bifurcation at the solid blue line, which is related to the blue dashed line representing the saddle-node bifurcation that was found in the  $\alpha_y = 0$  space. The solid blue line intersects the black dash-dotted line at SNT6. Therefore only in a small interval  $N_c \in (1.2, 1.5)$  the non-trivial fixed points disappear through a saddle-node bifurcation, while at larger  $N_c$  the non-trivial fixed points that branch of from the solid red line and the black dash-dotted line diverge for low values of  $x$ . In addition, for these fixed points we find a saddle-node bifurcation curve not only in the  $\alpha_y = 0$  space, as was the case in the previous figures, but also in the  $\alpha_g = 0$  space (dash-dotted blue line).

Figure 3.4d shows a few more transcritical bifurcation curves lying in the  $\alpha_y^{nt} = 0$  and/or  $\alpha_g^{nt} = 0$  subspace. Non-trivial fixed points that are related to these transcritical bifurcation curves, all diverge in one or multiple couplings for low  $x$  instead of disappearing through a saddle-node bifurcation. We notice the the black, solid red and dashed red line involve the sets of equilibria 1 and 2, as labeled in the previous section.

The eigenvectors that cross zero at the saddle-node bifurcations shown in figure 3.4a and 3.4b are shown in table 6 for  $N_c = 3$  along with the eigenvalues of the other eigenvectors. We see that in this model the bifurcations are strongly triggered by the  $\alpha_g$  interaction. Furthermore, as in the previous, model we find two complex eigenvalues for the saddle-node bifurcation of point the non-trivial fixed points 3 and 4. Eigenvectors corresponding to the complex eigenvalues are directed along the four-fermion couplings, and have very small contributions ( $|\eta_{\alpha_g}| < 0.004, |\eta_{\alpha_y}| < 0.016$ ) along the  $e_{\alpha_g}$  and  $e_{\alpha_y}$  direction, meaning that this complex scaling behavior involves operators, which are linear combinations of the effective four-fermi interactions.

Furthermore, we find multiple bifurcation points in figure 3.4, which are reported in table 7. The first cusp bifurcation and the points SNT5, IP1 and IP2 were already found in the previous model. In addition, we find an extra cusp point in the saddle-node bifurcation curve in the  $\alpha_g = 0$  space. This curve has another cusp bifurcation at IP1, making IP1 even more degenerate. The points TCT1 up to TCT6 all describe the intersection of two transcritical bifurcation curves, and can be described by the normal form

$$\begin{cases} \dot{\tilde{x}} = \tilde{\alpha}\tilde{x} + \tilde{x}^2, \\ \dot{\tilde{y}} = \tilde{\beta}\tilde{y} + \tilde{y}^2. \end{cases} \quad (3.7)$$

Finally, IP3 describes a point where 2 saddle-node bifurcation curves and 2 branches of a transcritical bifurcation intersect, and can therefore be described as a saddle-node-transcritical bifurcation, where an additional saddle-node bifurcation intersects. Four fixed points are involved in this bifurcation.

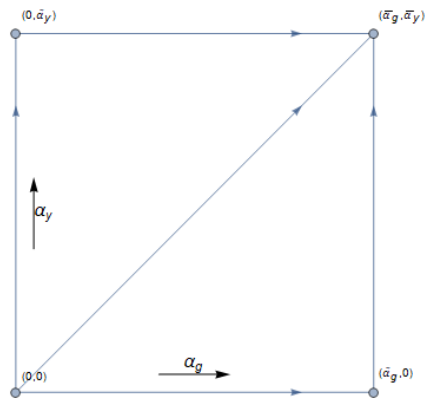


Figure 3.3: Flow structure between 4 fixed points.

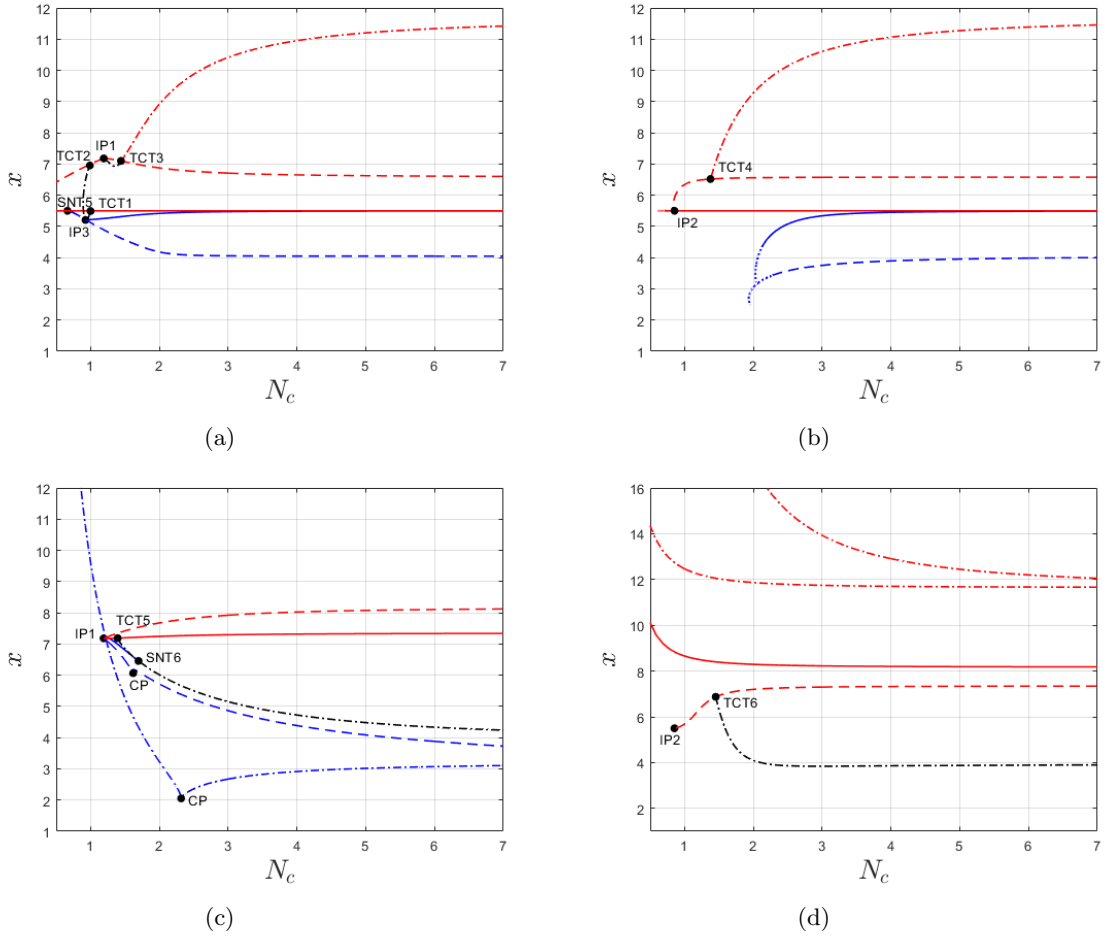


Figure 3.4: Bifurcations in the RG-flow of (3.3) in the  $(N_c, x)$ -plane.

- Solid blue line: saddle-node bifurcation with  $\alpha_g > 0, \alpha_y > 0$ .
- Dashed blue line: saddle-node bifurcation with  $\alpha_g > 0, \alpha_y = 0$ .
- Dash-dotted blue line: saddle-node bifurcation with  $\alpha_g = 0, \alpha_y > 0$ .
- Solid red line: transcritical bifurcation with  $\alpha_g = \alpha_g^{nt} = 0, \alpha_y = \alpha_y^{nt} = 0$ .
- Dashed red line: transcritical bifurcation with  $\alpha_g = \alpha_g^{nt} = 0, \alpha_y = 0$ .
- Dashed-dotted red line: transcritical bifurcation with  $\alpha_g = \alpha_g^{nt} = 0, \alpha_y > 0$ .
- Dash-dotted black line: transcritical bifurcation with  $\alpha_g > 0, \alpha_y = \alpha_y^{nt} = 0$ .
- Dotted line: at least one of the coupling constants  $|g_i| > 1$ .

Table 6: Eigenvalues and critical eigenvectors crossing marginality of the saddle-node bifurcation with non-trivial  $\alpha_g, \alpha_y$  at  $N_c = 3$ .

Equilibria	$(N_c, x)$	Eigenvalues	Critical eigenvector
8, 10	(3.00, 5.47)	$\{-2.06, -2.04, -1.93, -1.83, -0.20, 0\}$	(0.92, 0.36, 0.11, 0.00, -0.04, 0.07)
3, 4	(3.00, 5.34)	$\{2.38 \pm 0.28i, -2.34, -1.36, -1.09, 0\}$	(0.69, 0.29, 0.32, 0.09, 0.41, -0.39)

Table 7: Locations of bifurcations found in the model of QCD<sub>4</sub> (3.3) shown in figures 3.4a, 3.4b and 3.4c.

Bifurcation	$N_c$	$N_f$	$x$	$\alpha_g$	$\alpha_y$	$g_S$	$g_V$	$g_{V_1}$	$g_{V_2}$
CP	1.62	9.82	6.07	0.05	0	0.03	-0.17	0.01	0.22
CP	2.32	4.75	2.05	0	0.20	0.55	-0.32	0.20	0.51
SNT5	0.66	3.65	5.50	0	0	0	0	0	0
SNT6	1.70	10.95	6.46	0.03	0	-0.10	-0.17	-0.05	0.23
TCT1	1.00	5.50	5.50	0	0	0	0	0	0
TCT2	1.00	6.95	6.95	0	0	0	-0.14	0	0.14
TCT3	1.44	10.23	7.10	0	0	0.13	-0.15	0.07	0.20
TCT4	1.38	8.97	6.52	0	0	0.40	-0.10	0.19	-0.42
TCT5	1.39	10.02	7.19	0	0	-0.10	-0.16	-0.05	0.20
TCT6	1.45	9.98	6.87	0	0	-0.40	-0.13	-0.21	0.39
IP1	1.19	8.54	7.18	0	0	0	-0.16	0	0.17
IP2	0.85	4.69	5.50	0	0	0	0	0	-0.73
IP3	0.93	4.82	5.21	0.05	0	-0.01	-0.01	0.00	0.01

### 3.3 Discussion of the Results

In this section, we were interested how the addition of a scalar field can change the bifurcations found in the previous section. In particular, we would like to know whether we find similar behavior in the  $(\alpha_g > 0, \alpha_y > 0)$  space as we found in the  $(\alpha_g > 0, \alpha_y = 0)$  space. We find the transcritical bifurcation at  $x = 5.5$ , which marks the upper edge of the conformal window. This transcritical bifurcation now indicates the intersection of three fixed points: one on the  $(\alpha_g = 0, \alpha_y = 0)$  subspace, one on the  $(\alpha_g > 0, \alpha_y = 0)$  subspace, and one on the  $(\alpha_g > 0, \alpha_y > 0)$ . Furthermore, at this line there are two different transcritical bifurcation curves for different values of  $(g_S, g_V, g_{V_1}, g_{V_2})$  as was also found in the previous model. One of these bifurcations is shown in figure 3.4a and the other in figure 3.4b. We see that both saddle-node bifurcations that could indicate the lower edge of the conformal window in the model with  $\alpha_y = 0$  have a related saddle-node bifurcation in the  $(\alpha_g > 0, \alpha_y > 0)$  space, indicating that the phase transition at the lower edge of the conformal window is similar to the previous section and involves the merger of fixed points, followed by a walking behavior of the coupling constant, that changes continuously to a running behavior. However, the non-trivial saddle-node bifurcations are found at a higher value of  $x$  than the ones in the  $\alpha_y = 0$  subspace. This curve is very close but slightly below  $x = 5.5$  at high values of  $N_c$  and slightly decreases towards lower  $N_c$ . Therefore, the conformal window is much smaller in the theory that contains a scalar field in the adjoint representation, although conformal fixed and renormalized trajectories between those points remain to exist for lower values of  $x$ , but these are very unstable and require a high degree of fine-tuning.

Furthermore, we find that the fixed points, which were labeled by 5 and 7 have no related fixed points with non-trivial value of  $\alpha_y$ . Therefore, we don't have the spiraling behavior related to those fixed points as we had in the previous section. For the saddle-node bifurcation of the pair labeled by 6 and 9 there is only a related bifurcation with non-trivial and positive  $\alpha_g$  and  $\alpha_y$  in a small interval  $N_c \in (1.2, 1.5)$ , which makes it irrelevant for the physical model, since we require integer values of  $N_c$ . Therefore, we find that the non-trivial fixed points of the sets 1, 2, 6 and 9 all diverge for low  $x$ .



---

## 4 Conclusions and Outlook

The purpose of this thesis was twofold. On the one hand, we wanted to elaborate on the connections between renormalization group theory and dynamical systems theory and see whether physical theories can be improved from the interaction between those two fields, as was proposed in [16]. On the other hand, we have rigorously analyzed a model for quantum chromodynamics in 4 dimensions to shine light on the phase transition at the lower edge of the conformal window and to find new methods of probing quantum chromodynamics at scales where perturbation theory is not reliable anymore. We have found that bifurcation analysis is a good tool to analyze renormalization group flows in quantum field theory. By translation to the language of dynamical systems and the use of numerical tools developed in this field we have been able to find phase transitions in renormalization group flows in multiple control parameters. This analysis was usually done in a limit such that models can be analyzed analytically, where only one control parameter is left. On the other hand, numerical methods in this field usually involve lattice simulations, which is computationally intensive, since a separate simulation has to be done for every value of  $(N_c, N_f)$ . Although lattice simulations can provide more information on the model than bifurcation analysis can do, for the study of the location and type of phase transition bifurcation analysis is the ideal tool. In future research, it would be useful to consider bifurcation analysis as a standard tool in analyzing dynamical systems generated by the renormalization group. In particular, since it's a good tool to analyze the phase transitions in complicated models without heavy computational techniques. Together with other methods it can then provide a more complete picture of many quantum field theories, especially in models with multiple parameters.

From a dynamical systems perspective, on the other hand we have not found many new bifurcations, and in this sense the technique doesn't provide the more interesting results which can be found in other applications such as climate model and population dynamics, since we expect that limit cycles can't exist in renormalization group flows of unitary quantum field theories. We do however find saddle-node and transcritical bifurcation, and many degenerate interactions between the two. For future research it would be interesting to study those interactions more carefully, and try to find normal forms of these interactions.

From the physical perspective, we have rigorously analyzed all possible fixed points and bifurcations in a model for  $\text{QCD}_4$  with effective four interaction, with and without scalar interactions. We have started from the standard QCD lagrangian and added effective four-fermi interaction to it, since it is expected from earlier work that these interaction play a crucial role in the breaking of chiral symmetry and the generation of fermion mass in QCD. By switching to an effective lagrangian we have been able to bring higher order terms into the beta functions. In this way, we were able to make predictions for quantum chromodynamics in regions where perturbation theory breaks down. In particular, we have argued that the conformal window in  $\text{QCD}_4$  closes due to a fixed point merger or saddle-node bifurcation. Due to this bifurcation all renormalized trajectories with finite IR limit become unstable. This happens close to  $N_f/N_c = 4$  for all  $N_c \geq 3$ , while this ratio changes for  $N_c < 3$ . Furthermore, we have argued that there might exist a phase transition within the conformal window, where the size of the set of structurally stable renormalized trajectories changes discontinuously, but remains to exist. This transition could possibly be related to phase transitions in the quark gluon plasma. Also, we have found multiple fixed points and bifurcations of those points within the theory, which haven't been reported before. In addition, we found orbits within the RG-flow that showed spiraling behavior along effective interactions. This spiraling behavior is induced by complex eigenvalues (scaling dimensions). It would be interesting to see if those can be related to exotic RG-flows as discussed in [21]. Furthermore, we have added a meson-like scalar field to the model to see how this affects

---

the model. Due to the scalar field the conformal window closes. However, the type of bifurcations that we found for  $(\alpha_g > 0, \alpha_y > 0)$  are similar to the ones found for  $(\alpha_g > 0, \alpha_y = 0)$ .

For future research, it would be interesting to extend the model with other effective interactions such as six-fermi interactions. Also, it could be interesting to extend the scalar model with a scalar mass, add a fourth order interaction to the extension of the model or to consider models that transform in other representation of the gauge-group. Studies of such extended models and comparisons with the analysis in this thesis could shed light on which fixed points and orbits have physical relevance, and which appear in this specific model only.

## A Feynman Rules for QCD<sub>4</sub> with a Four-Fermi Interaction

The effective action given by eq. (2.1) invokes a set of Feynman rules. An overview of the rules is given in this section.

The theory has three propagators<sup>A.1</sup>:

$$\begin{aligned}
 A_\mu^A \text{---} \overleftarrow{k} \text{---} A_\nu^B &\sim g^2 \delta^{AB} \frac{1}{k^2} \left( \eta_{\mu\nu} - (1-\xi) \frac{k_\mu k_\nu}{k^2} \right), \\
 \bar{L}_{ai} \text{---} \overleftarrow{p} \text{---} L^{bj} &\sim \delta_a^b \delta_i^j \frac{1+\gamma^5}{2} \frac{i}{\not{p}} \frac{1-\gamma^5}{2}, \\
 \bar{R}_{ai} \text{---} \overleftarrow{p} \text{---} R^{bj} &\sim \delta_a^b \delta_i^j \frac{1-\gamma^5}{2} \frac{i}{\not{p}} \frac{1+\gamma^5}{2},
 \end{aligned}$$

where  $\mu, \nu$  label the space-time indices,  $A, B$  label the colors in the adjoint representation of  $SU(N_c)$ ,  $a, b$  label the color in the fundamental representation of  $SU(N_c)$  and  $\{i, j\}$  label the flavor in the fundamental representation of  $SU(N_f)$ . Furthermore, we take the Landau gauge in which the gauge parameter  $\xi = 0$ .

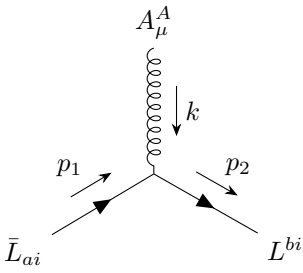
There exists a 3-point and a 4-point gluon-gluon interaction, which won't be encountered in the one-loop expansions, that will be considered later on, but are mentioned for completeness:

$$\begin{aligned}
 \begin{array}{c}
 A_\mu^A \\
 \downarrow k_1 \\
 \begin{array}{ccc}
 A_\nu^B & \swarrow k_2 & \searrow k_3 \\
 & & A_\rho^C
 \end{array}
 \end{array}
 &\sim g^{-2} f_{ABC} (\eta^{\mu\nu} (k_1 - k_2)^\rho + \eta^{\nu\rho} (k_2 - k_3)^\mu + \eta^{\rho\mu} (k_3 - k_1)^\nu) \\
 &\quad \times \delta(k_1 + k_2 + k_3) A_\mu^A(k_1) A_\nu^B(k_2) A_\rho^C(k_3), \\
 \\
 \begin{array}{c}
 A_\mu^A \\
 \downarrow k_1 \\
 \begin{array}{ccc}
 A_\nu^B & \xrightarrow{k_2} & A_\sigma^D \\
 \uparrow k_3 & & \leftarrow k_4 \\
 & & A_\rho^C
 \end{array}
 \end{array}
 &\sim g^{-2} [f_{ABE} f_{CD}^E (\eta^{\mu\rho} \eta^{\nu\sigma} - \eta^{\mu\sigma} \eta^{\nu\rho}) \\
 &\quad + f_{ACE} f_{BD}^E (\eta^{\mu\nu} \eta^{\rho\sigma} - \eta^{\mu\sigma} \eta^{\rho\nu}) \\
 &\quad + f_{ADE} f_{BC}^E (\eta^{\mu\nu} \eta^{\sigma\rho} - \eta^{\mu\rho} \eta^{\sigma\nu})] \\
 &\quad \times \delta(k_1 + k_2 + k_3 + k_4) A_\mu^A(k_1) A_\nu^B(k_2) A_\rho^C(k_3) A_\sigma^D(k_4).
 \end{aligned}$$

<sup>A.1</sup>All Feynman diagrams are made with the Tikz-Feynman package [35].

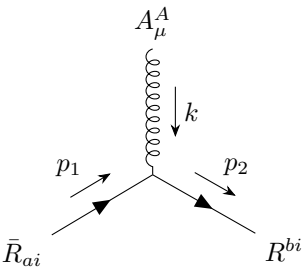
---

The fermion-gluon interaction (gauge vertex) is given by:



The diagram shows a central vertex where a gluon line (represented by a wavy line) and two fermion lines meet. The gluon line is labeled  $A_\mu^A$  and has a downward-pointing arrow labeled  $k$ . The fermion line on the left is labeled  $\bar{L}_{ai}$  and has an upward-pointing arrow labeled  $p_1$ . The fermion line on the right is labeled  $L^{bi}$  and has a downward-pointing arrow labeled  $p_2$ .

$$\sim (t_A)_b^a \delta(p_1 - p_2 + k) \bar{L}_{ai} \gamma^\mu A_\mu^A L^{bi}$$



The diagram shows a central vertex where a gluon line (represented by a wavy line) and two fermion lines meet. The gluon line is labeled  $A_\mu^A$  and has a downward-pointing arrow labeled  $k$ . The fermion line on the left is labeled  $\bar{R}_{ai}$  and has an upward-pointing arrow labeled  $p_1$ . The fermion line on the right is labeled  $R^{bi}$  and has a downward-pointing arrow labeled  $p_2$ .

$$\sim (t_A)_b^a \delta(p_1 - p_2 + k) \bar{R}_{ai} \gamma^\mu A_\mu^A R^{bi}$$

Furthermore, there are four four-fermi interactions:

$$\begin{array}{l}
 \begin{array}{c}
 \bar{L}_{ai} \quad \bar{R}_{bj} \\
 \swarrow \quad \searrow \\
 p_1 \quad p_2 \quad p_3 \quad p_4 \\
 \swarrow \quad \searrow \\
 R^{aj} \quad L^{bi}
 \end{array}
 \sim \frac{2G_S}{\Lambda^2} \delta(p_1 - p_2 + p_3 - p_4) \bar{L}_{ai} R^{aj} \bar{R}_{bj} L^{bi} \\
 \\
 \begin{array}{c}
 \bar{L}_{ai} \quad \bar{L}_{bj} \\
 \swarrow \quad \searrow \\
 p_1 \quad p_2 \quad p_3 \quad p_4 \\
 \swarrow \quad \searrow \\
 L^{aj} \quad L^{bi}
 \end{array}
 \sim \frac{G_V}{\Lambda^2} \delta(p_1 - p_2 + p_3 - p_4) \bar{L}_{ai} \gamma^\mu L^{aj} \bar{L}_{bj} \gamma_\mu L^{bi} + (L \rightarrow R) \\
 \\
 \begin{array}{c}
 \bar{L}_{ai} \quad \bar{R}_{bj} \\
 \swarrow \quad \searrow \\
 p_1 \quad p_2 \quad p_3 \quad p_4 \\
 \swarrow \quad \searrow \\
 L^{ai} \quad R^{bj}
 \end{array}
 \sim \frac{2G_{V_1}}{\Lambda^2} \delta(p_1 - p_2 + p_3 - p_4) \bar{L}_{ai} \gamma^\mu L^{ai} \bar{R}_{bj} \gamma_\mu R^{bj} \\
 \\
 \begin{array}{c}
 \bar{L}_{ai} \quad \bar{L}_{bj} \\
 \swarrow \quad \searrow \\
 p_1 \quad p_2 \quad p_3 \quad p_4 \\
 \swarrow \quad \searrow \\
 L^{ai} \quad L^{bj}
 \end{array}
 \sim \frac{G_{V_2}}{\Lambda^2} \delta(p_1 - p_2 + p_3 - p_4) \bar{L}_{ai} \gamma^\mu L^{ai} \bar{L}_{bj} \gamma_\mu L^{bj} + (L \rightarrow R).
 \end{array}$$

Notice that the vertices have been split up in two parts. This is done to make clear along which lines the color charge is conserved, and will make the calculations in appendix C more tractable, but has no further physical meaning.

## B Beta Function for the Gauge Vertex

In this appendix, we reproduce the method used in [32] to calculate the beta function for the gauge vertex. We're only interested in gauge invariant contributions to the beta function, but the Wetterich equation (1.36) doesn't necessarily respect gauge invariance. Therefore, we don't use the exact renormalization approach. Instead we start from the well known 2-loop perturbative beta function for QCD<sub>4</sub> with  $N_c$  colors and  $N_f$  massless flavors [36]:

$$\beta_g^{[2]} \equiv \Lambda \frac{d\alpha_g}{d\Lambda} = -2b_0\alpha_g^2 - 2b_1\alpha_g^3 \quad (\text{B.1})$$

with

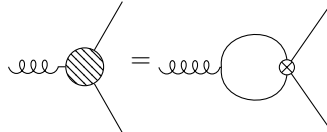
$$b_0 = \frac{11}{3}N_c - \frac{2}{3}N_f$$

$$b_1 = \frac{34}{3}N_c^2 - N_f \left( \frac{N_c^2 - 1}{N_c} + \frac{10}{3}N_c \right).$$

Next, we would like to include effective interactions induced by the four-fermi couplings. These can be added perturbatively to the beta functions. The beta function is then given by

$$\Lambda \frac{d\alpha_g}{d\Lambda} = \beta_g^{[2]} + \Delta\alpha_g, \quad (\text{B.2})$$

where the last term is represents the perturbative corrections induced by the effective couplings. These perturbations should be chosen such that they're gauge invariant and such that they represent perturbations, that are included in  $\lim_{n \rightarrow \infty} \beta_g^{[n]}$ , but not in  $\beta_g^{[2]}$ . There is one one-loop correction induced by the effective four-fermi interaction, which is represented by



$$\text{Diagram (B.3)} \quad (\text{B.3})$$

This diagram is in the sharp cutoff limit evaluated as

$$\frac{N_f(G_S - 2G_V)}{8\pi^2} \bar{L}_{ai}(t_A)^a \gamma^\mu A_\mu^A L^{bi} \delta \ln(\Lambda) + (L \rightarrow R). \quad (\text{B.4})$$

The contribution due to the  $G_{V_1}$  and the  $G_{V_2}$  interaction vanish due to the tracelessness of the generators of  $SU(N)$ . The contribution to the beta function of  $g$  is therefore given by

$$\delta g = -\frac{N_f}{2}(g_S - 2g_V)g\delta \ln(\Lambda), \quad (\text{B.5})$$

and hence in terms of  $\alpha_g$

$$\delta\alpha_g = -N_f(g_S - 2g_V)\alpha_g\delta \ln(\Lambda). \quad (\text{B.6})$$

However, this correction turns out to be gauge dependent [37], and therefore we discard it. A possible two-loop correction is given by



$$\text{Diagram (B.7)} \quad (\text{B.7})$$

For the effective four-fermi interaction one could take  $\mathcal{O}_i$ ,  $i \in \{S, V, V_1, V_2\}$ . However, since the interactions should represent perturbations, which are included in  $\lim_{n \rightarrow \infty} \beta_g^{[n]}$  the

---

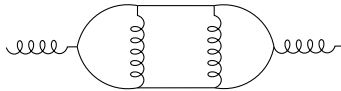
chirality should be the same in the whole diagram. This excludes the interactions  $\mathcal{O}_S$  and  $\mathcal{O}_{V_1}$ . Furthermore, due to the tracelessness of the generators of  $SU(N)$  the contribution due to  $\mathcal{O}_{V_2}$  vanishes. Therefore, only  $\mathcal{O}_V$  contributes, and its contribution is in the sharp cutoff limit given by

$$-\frac{N_c N_f g^4 G_V}{32\pi^4} \delta \ln(\Lambda), \quad (\text{B.8})$$

yielding a contribution to the beta function of the form

$$\delta\alpha_g = 2N_c N_f \alpha_g^2 g_V \delta \ln(\Lambda). \quad (\text{B.9})$$

To make the beta function closer to the exact one, one could add more corrections, like the three-loop corrections to the vacuum polarization containing the effective four-fermi coupling or corrections induced by the four-fermi interaction to the three-gluon or four-gluon interactions.<sup>B.1</sup> Also, one could use a higher order beta function  $\beta_g^{[n]}$  of the gauge coupling. However, one should be careful, since terms in  $\beta_g^{[n]}$  and  $\delta\alpha_g$  might overlap. For example, the diagram



is contained in both  $\beta_g^{[3]}$  and in the correction given by eq. (B.7).

---

<sup>B.1</sup>These correction are all two-loop or higher.

## C Beta Functions for the Four-Fermi Interactions

We can find the beta functions of the model using equation (1.38):

$$\frac{d}{dt}\Gamma_\Lambda[\phi] = -\Lambda \frac{d}{d\Lambda}\Gamma_\Lambda[\phi] = \sum_{n=1}^{\infty} \beta_{g_n}(t) \mathcal{O}_n(\phi)$$

by noticing that

$$\frac{d}{d\Lambda}\Gamma_\Lambda[\phi] = \lim_{\delta\Lambda \rightarrow 0} \frac{\Gamma_{\Lambda+\delta\Lambda}[\phi] - \Gamma_\Lambda[\phi]}{\delta\Lambda} =: \lim_{\delta\Lambda \rightarrow 0} \frac{\delta\Gamma_\Lambda[\phi]}{\delta\Lambda}.$$

Furthermore,

$$\delta\Gamma_\Lambda = \int d^4p \delta\mathcal{L}_{\text{QCD}} + \delta\mathcal{L}_{4f}$$

with

$$\delta\mathcal{L}_{4f} = \sum_{i \in \{S, V, V_1, V_2\}} \left( \frac{\delta G_i(\Lambda)}{\Lambda^{2(1+\eta)}} - \frac{2G_i(\Lambda)\delta\Lambda}{\Lambda^{3+2\eta}} \right) \mathcal{O}_i,$$

whence

$$\Lambda \frac{dG_i}{d\Lambda} = \lim_{\delta\Lambda \rightarrow 0} \left[ 2(1+\eta)G_i + \Lambda^{3+2\eta} \frac{\delta\Gamma_\Lambda}{\delta\Lambda} \right]_{\text{terms} \propto \mathcal{O}_i}.$$

For this Lagrangian the anomalous dimension is  $\eta = 0$  [32]. The last term can be evaluated using the Wetterich equation (1.36):

$$\lim_{\delta\Lambda \rightarrow 0} \Lambda \frac{\delta\Gamma_\Lambda}{\delta\Lambda} = \frac{1}{2} \text{Tr} \left[ \left( \frac{\delta^2\Gamma_\Lambda}{\delta\phi\delta\phi} + \mathcal{R}_\Lambda \right)^{-1} \frac{\delta\mathcal{R}_\Lambda}{\delta\Lambda} \right].$$

The right hand side is equal to the expansion in terms of all 1-particle-irreducible diagrams, so we only have to find all the 1-particle-irreducible diagrams proportional to the four point interactions. We'll evaluate the diagrams in the sharp cutoff limit, where  $\delta\mathcal{R}_\Lambda = \Lambda\delta(|p| - \Lambda)\delta\Lambda$ . Furthermore, we use spherical coordinates in which

$$\int' dp := \int_{-\infty}^{\infty} \frac{d^4p}{(2\pi)^4} \Lambda\delta(|p| - \Lambda) = \frac{1}{(2\pi)^4} \int_0^{\infty} dp p^3 \int d\Omega \Lambda\delta(|p| - \Lambda),$$

where the  $\Omega$  represents the spherical part. If there is no angular dependence this part is the surface area of a 3-dimensional sphere, which is  $2\pi^2$ . In the calculations of the diagrams we'll make use of the following integrals, which follow from symmetry arguments

$$\begin{aligned} \int' dp \frac{p_\mu p_\nu}{p^{2n}} &= \frac{\Lambda^{6-2n}}{8\pi^2} \frac{1}{4} \eta_{\mu\nu} \\ \int' dp \frac{p_\mu p_\nu p_\rho p_\sigma}{p^{2n}} &= \frac{\Lambda^{8-2n}}{8\pi^2} \frac{1}{24} (\eta_{\mu\nu}\eta_{\rho\sigma} + \eta_{\mu\rho}\eta_{\nu\sigma} + \eta_{\mu\sigma}\eta_{\nu\rho}) \\ \int' dp \frac{p_\alpha p_\beta p_\mu p_\nu p_\rho p_\sigma}{p^{2n}} &= \frac{\Lambda^{10-2n}}{8\pi^2} \frac{1}{192} (\eta_{\alpha\beta}\eta_{\mu\nu}\eta_{\rho\sigma} + \eta_{\alpha\beta}\eta_{\mu\rho}\eta_{\nu\sigma} + \eta_{\alpha\beta}\eta_{\mu\sigma}\eta_{\nu\rho} + \eta_{\alpha\mu}\eta_{\beta\nu}\eta_{\rho\sigma} \\ &\quad + \eta_{\alpha\mu}\eta_{\beta\rho}\eta_{\nu\sigma} + \eta_{\alpha\mu}\eta_{\beta\sigma}\eta_{\nu\rho} + \eta_{\alpha\nu}\eta_{\beta\mu}\eta_{\rho\sigma} + \eta_{\alpha\nu}\eta_{\beta\rho}\eta_{\mu\sigma} + \eta_{\alpha\nu}\eta_{\beta\sigma}\eta_{\mu\rho} \\ &\quad + \eta_{\alpha\rho}\eta_{\beta\mu}\eta_{\nu\sigma} + \eta_{\alpha\rho}\eta_{\beta\nu}\eta_{\mu\sigma} + \eta_{\alpha\rho}\eta_{\beta\sigma}\eta_{\mu\nu} + \eta_{\alpha\sigma}\eta_{\beta\mu}\eta_{\nu\rho} + \eta_{\alpha\sigma}\eta_{\beta\nu}\eta_{\mu\rho} \\ &\quad + \eta_{\alpha\sigma}\eta_{\beta\rho}\eta_{\mu\nu}). \end{aligned}$$



In addition, we make extensive use of the following identities

$$\begin{aligned}
\{\gamma^\mu, \gamma^\nu\} &= 2\eta^{\mu\nu} I_4 \\
\gamma^\mu \gamma_\mu &= 4I_4 \\
\gamma^\mu \gamma^\nu \gamma_\mu &= -2\gamma^\nu \\
\gamma^\mu \gamma^\nu \gamma^\rho \gamma_\mu &= 4\eta^{\nu\rho} I_4 \\
\gamma^\mu \gamma^\nu \gamma^\rho &= \eta^{\mu\nu} \gamma^\rho + \eta^{\nu\rho} \gamma^\mu - \eta^{\mu\rho} \gamma^\nu - i\varepsilon^{\sigma\mu\nu\rho} \gamma_\sigma \gamma^5 \\
\text{Tr}(\gamma^\mu \gamma^\nu) &= 4\eta^{\mu\nu} \\
\text{Tr}(\gamma^5) &= \text{Tr}(\gamma^\mu \gamma^\nu \gamma^5) = 0, \\
\varepsilon_{\alpha\mu\nu\rho} \varepsilon^{\beta\mu\nu\rho} &= -6\delta_\alpha^\beta.
\end{aligned}$$

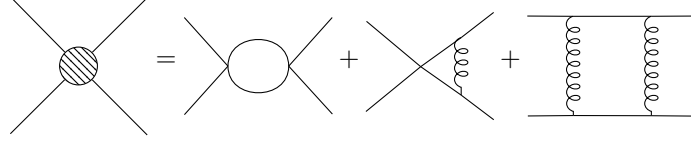
Finally, we use the identities [32]

$$2 \sum_{A=1}^{N_c} (t^A)_d^a (t^A)_b^c = \delta_b^a \delta_d^c - \frac{1}{N_c} \delta_d^a \delta_b^c$$

and [32]

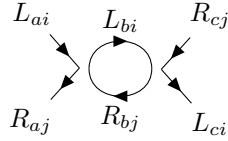
$$\begin{aligned}
\bar{L}_{ai} \gamma^\mu L^{ai} \bar{R}_{bj} \gamma_\mu R^{bj} &= -2\bar{L}_{ai} R^{bj} \bar{R}_{bj} L^{ai} \\
\bar{L}_{ai} \gamma^\mu L^{bi} \bar{R}_{bj} \gamma_\mu R^{aj} &= -2\bar{L}_{ai} R^{aj} \bar{R}_{bj} L^{bi} \\
\bar{L}_{ai} \gamma^\mu L^{ai} \bar{L}_{bj} \gamma_\mu L^{bj} &= \bar{L}_{ai} \gamma^\mu L^{bj} \bar{L}_{bj} \gamma_\mu L^{ai}, \quad (L \rightarrow R) \\
\bar{L}_{ai} \gamma^\mu L^{bi} \bar{L}_{bj} \gamma_\mu L^{aj} &= \bar{L}_{ai} \gamma^\mu L^{aj} \bar{L}_{bj} \gamma_\mu L^{bi}, \quad (L \rightarrow R).
\end{aligned}$$

Using the Feynman rules from appendix A, we find the following contributing 1PI diagrams:



There are 29 different diagrams of the first type, 12 of the second type and 4 of the third.

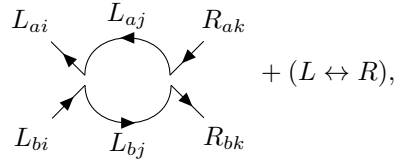
Five diagrams of the first type contribute to the beta function of  $G_S$ . One of those is proportional to  $g_S^2$ :



which is evaluated as

$$\begin{aligned}
&\left(\frac{2G_s}{\Lambda^2}\right)^2 N_c \int' dp \bar{L}_{ai} R^{aj} \text{Tr} \left[ \frac{1-\gamma^5}{2} \frac{i}{\not{p}} \frac{1+\gamma^5}{2} \frac{1+\gamma^5}{2} \frac{i}{\not{p}} \frac{1-\gamma^5}{2} \right] \bar{R}_{cj} L^{ci} \\
&= -\frac{1}{2} \frac{4G_s^2}{\Lambda^4} N_c \int' dp \frac{p_\mu p_\nu}{p^4} \text{Tr} [\gamma^\mu (1+\gamma^5) \gamma^\nu] \frac{\mathcal{O}_S}{2} \\
&= -\frac{G_s^2}{\Lambda^4} N_c \frac{\Lambda^2}{8\pi^2} \frac{\eta_{\mu\nu}}{4} \text{Tr} [\gamma^\mu (1+\gamma^5) \gamma^\nu] \mathcal{O}_S \\
&= -\frac{N_c G_s^2}{2\pi^2 \Lambda^2} \mathcal{O}_S.
\end{aligned}$$

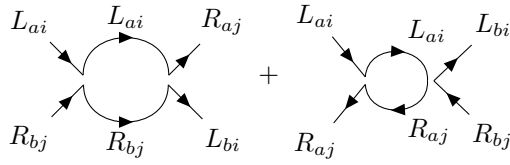
One diagram is proportional to  $g_S g_V$ :



which is evaluated as

$$\frac{N_f G_S G_V}{2\pi^2 \Lambda^2} \mathcal{O}_S.$$

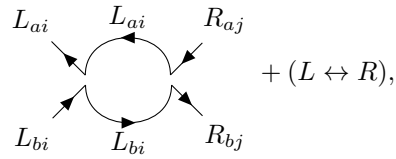
Two diagrams are proportional to  $g_S g_{V_1}$ :



which are evaluated as

$$-\frac{G_S G_{V_1}}{2\pi^2 \Lambda^2} \mathcal{O}_S \quad \text{and} \quad \frac{2G_S G_{V_1}}{\pi^2 \Lambda^2} \mathcal{O}_S.$$

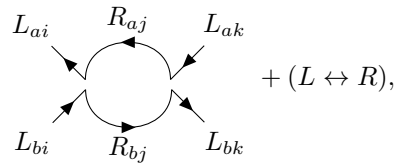
One diagram is proportional to  $g_S g_{V_2}$ :



which is evaluated as

$$\frac{G_S G_{V_2}}{2\pi^2 \Lambda^2} \mathcal{O}_S.$$

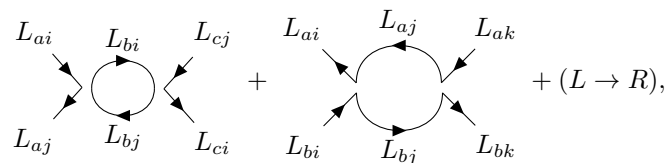
Five diagrams of the first type contribute to the beta function of  $G_V$ . One of those is proportional to  $g_S^2$ :



which is evaluated as

$$\frac{N_f G_S^2}{16\pi^2 \Lambda^2} \mathcal{O}_V.$$

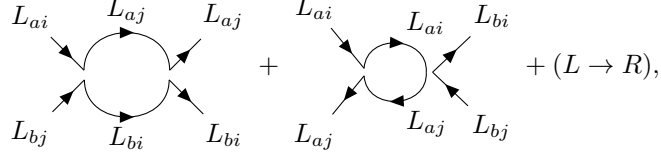
Two diagrams are proportional to  $g_V^2$ :



which are evaluated as

$$\frac{N_c G_V^2}{4\pi^2 \Lambda^2} \mathcal{O}_V \quad \text{and} \quad \frac{N_f G_V^2}{4\pi^2 \Lambda^2} \mathcal{O}_V.$$

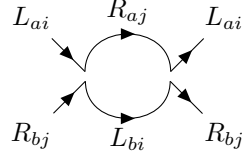
Two diagrams are proportional to  $g_V g_{V_2}$ :



which are evaluated as

$$-\frac{2G_V G_{V_2}}{\pi^2 \Lambda^2} \mathcal{O}_V \quad \text{and} \quad \frac{G_V G_{V_2}}{2\pi^2 \Lambda^2} \mathcal{O}_V.$$

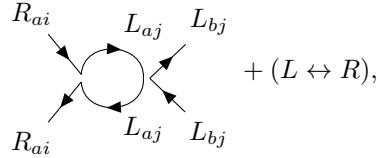
Nine diagrams of the first type contribute to the beta function of  $G_{V_1}$ . One of those is proportional to  $g_S^2$ :



which is evaluated as

$$-\frac{G_S^2}{16\pi^2 \Lambda^2} \mathcal{O}_{V_1}.$$

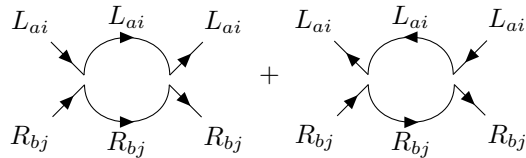
One diagram is proportional to  $g_S g_V$ :



which is evaluated as

$$-\frac{G_S G_V}{4\pi^2 \Lambda^2} \mathcal{O}_{V_1}.$$

Two diagrams are proportional to  $g_{V_1}^2$ :



which are evaluated as

$$\frac{G_{V_1}^2}{4\pi^2 \Lambda^2} \mathcal{O}_{V_1} \quad \text{and} \quad -\frac{G_{V_1}^2}{\pi^2 \Lambda^2} \mathcal{O}_{V_1}.$$

One diagram is proportional to  $g_S g_{V_2}$ :

$$\begin{array}{c}
 L_{ai} \quad R_{aj} \quad R_{bk} \\
 \swarrow \quad \nearrow \quad \swarrow \\
 \text{---} \text{---} \text{---} \\
 \nwarrow \quad \searrow \quad \nwarrow \\
 L_{ai} \quad R_{aj} \quad R_{bk}
 \end{array}
 + (L \leftrightarrow R),$$

which is evaluated as

$$-\frac{N_f G_S G_{V_2}}{4\pi^2 \Lambda^2} \mathcal{O}_{V_1}.$$

Two diagrams are proportional to  $g_V g_{V_1}$ :

$$\begin{array}{c}
 L_{ai} \quad L_{bi} \quad R_{cj} \\
 \swarrow \quad \nearrow \quad \swarrow \\
 \text{---} \text{---} \text{---} \\
 \nwarrow \quad \searrow \quad \nwarrow \\
 L_{ai} \quad L_{bi} \quad R_{cj}
 \end{array}
 +
 \begin{array}{c}
 L_{ai} \quad L_{aj} \quad R_{bk} \\
 \swarrow \quad \nearrow \quad \swarrow \\
 \text{---} \text{---} \text{---} \\
 \nwarrow \quad \searrow \quad \nwarrow \\
 L_{ai} \quad L_{aj} \quad R_{bk}
 \end{array}
 + (L \leftrightarrow R),$$

which are evaluated as

$$\frac{N_c G_V G_{V_1}}{2\pi^2 \Lambda^2} \mathcal{O}_{V_1} \quad \text{and} \quad \frac{N_f G_V G_{V_1}}{2\pi^2 \Lambda^2} \mathcal{O}_{V_1}.$$

Two diagrams are proportional  $g_{V_1} g_{V_2}$ :

$$\begin{array}{c}
 L_{ai} \quad R_{bj} \quad R_{ck} \\
 \swarrow \quad \nearrow \quad \swarrow \\
 \text{---} \text{---} \text{---} \\
 \nwarrow \quad \searrow \quad \nwarrow \\
 L_{ai} \quad R_{bj} \quad R_{ck}
 \end{array}
 +
 \begin{array}{c}
 L_{ai} \quad L_{ai} \quad R_{bj} \\
 \swarrow \quad \nearrow \quad \swarrow \\
 \text{---} \text{---} \text{---} \\
 \nwarrow \quad \searrow \quad \nwarrow \\
 L_{ai} \quad L_{ai} \quad R_{bj}
 \end{array}
 + (L \leftrightarrow R),$$

which are evaluated as

$$\frac{N_c N_f G_{V_1} G_{V_2}}{2\pi^2 \Lambda^2} \mathcal{O}_{V_1} \quad \text{and} \quad \frac{G_{V_1} G_{V_2}}{2\pi^2 \Lambda^2} \mathcal{O}_{V_1}.$$

Ten diagrams of the first type contribute to the beta function of  $G_{V_2}$ . Two of those are proportional to  $g_V^2$ :

$$\begin{array}{c}
 L_{ai} \quad L_{aj} \quad L_{ai} \\
 \swarrow \quad \nearrow \quad \swarrow \\
 \text{---} \text{---} \text{---} \\
 \nwarrow \quad \searrow \quad \nwarrow \\
 L_{bj} \quad L_{bi} \quad L_{bj}
 \end{array}
 +
 \begin{array}{c}
 L_{ai} \quad L_{aj} \quad L_{bj} \\
 \swarrow \quad \nearrow \quad \swarrow \\
 \text{---} \text{---} \text{---} \\
 \nwarrow \quad \searrow \quad \nwarrow \\
 L_{ai} \quad L_{aj} \quad L_{bj}
 \end{array}
 + (L \rightarrow R),$$

which are evaluated as

$$-\frac{G_V^2}{\pi^2 \Lambda^2} \mathcal{O}_{V_2} \quad \text{and} \quad \frac{G_V^2}{4\pi^2 \Lambda^2} \mathcal{O}_{V_2}.$$

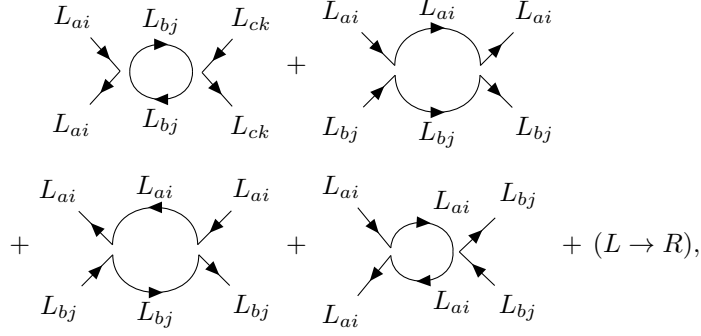
One diagram is proportional to  $g_{V_1}^2$ :

$$\begin{array}{c}
 L_{ai} \quad R_{bj} \quad L_{ck} \\
 \swarrow \quad \nearrow \quad \swarrow \\
 \text{---} \text{---} \text{---} \\
 \nwarrow \quad \searrow \quad \nwarrow \\
 L_{ai} \quad R_{bj} \quad L_{ck}
 \end{array}
 + (L \leftrightarrow R),$$

which is evaluated as

$$-\frac{N_c N_f G_{V_1}^2}{4\pi^2 \Lambda^2} \mathcal{O}_{V_2}.$$

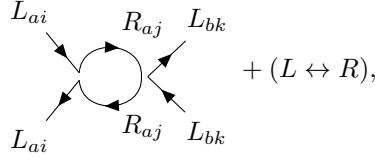
Four diagrams are proportional to  $g_{V_2}^2$ :



which are evaluated as

$$\frac{N_c N_f G_{V_2}^2}{4\pi^2 \Lambda^2} \mathcal{O}_{V_2}, \quad -\frac{G_{V_2}^2}{\pi^2 \Lambda^2} \mathcal{O}_{V_2}, \quad \frac{G_{V_2}^2}{4\pi^2 \Lambda^2} \mathcal{O}_{V_2} \quad \text{and} \quad \frac{G_{V_2}^2}{4\pi^2 \Lambda^2} \mathcal{O}_{V_2}.$$

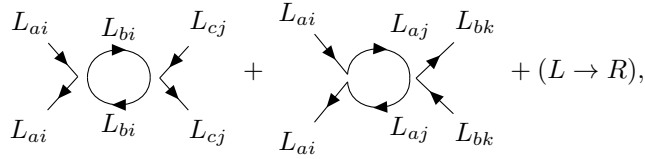
One diagram is proportional  $g_S g_{V_1}$ :



which is evaluated as

$$-\frac{N_f G_S G_{V_1}}{4\pi^2 \Lambda^2} \mathcal{O}_{V_2}.$$

Two diagrams are proportional  $g_V g_{V_2}$ :

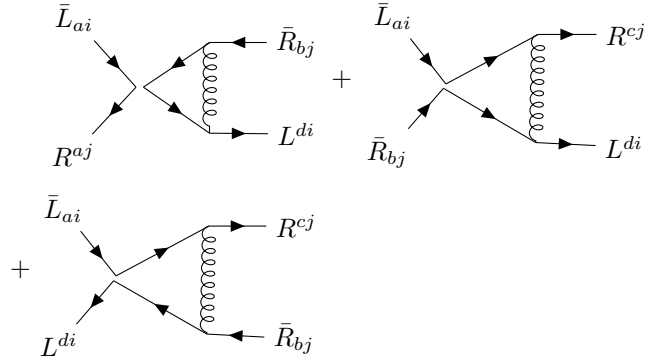


which are evaluated as

$$\frac{N_c G_V G_{V_2}}{2\pi^2 \Lambda^2} \mathcal{O}_{V_2} \quad \text{and} \quad \frac{N_f G_V G_{V_2}}{2\pi^2 \Lambda^2} \mathcal{O}_{V_2}.$$

Three diagrams of the second type are proportional to  $g_S \alpha_g$  and contribute to the beta

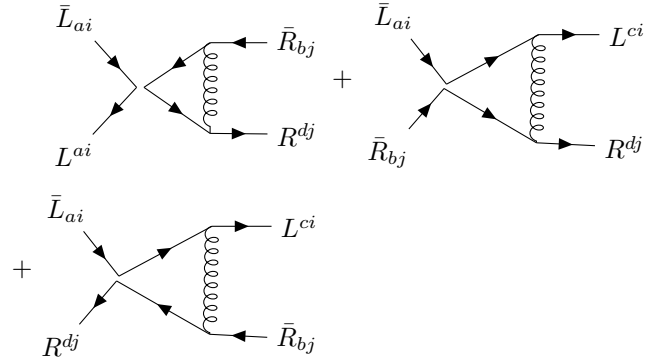
functions of  $G_S$  and  $G_{V_1}$ :



The second and the third both evaluate to 0 and the first is evaluated as

$$-3 \left( N_c - \frac{1}{N_c} \right) \frac{G_S g^2}{8\pi^2 \Lambda^2} \mathcal{O}_S.$$

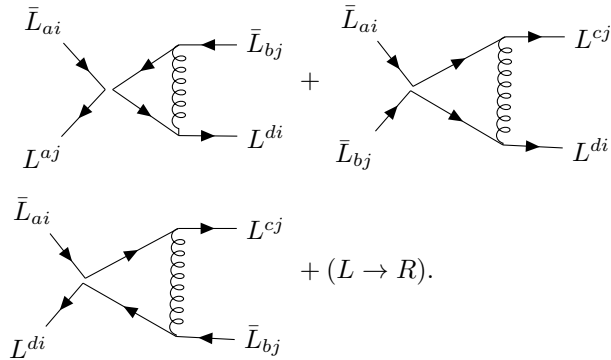
Three diagrams of the second type are proportional to  $g_{V_1} \alpha_g$  and contribute to the beta functions of  $G_S$  and  $G_{V_1}$ :



The first and second both evaluate to 0 and the third evaluates to

$$6 \frac{G_{V_1} g^2}{8\pi^2 \Lambda^2} \mathcal{O}_S + \frac{3}{N_c} \frac{G_{V_1} g^2}{8\pi^2 \Lambda^2} \mathcal{O}_{V_1}.$$

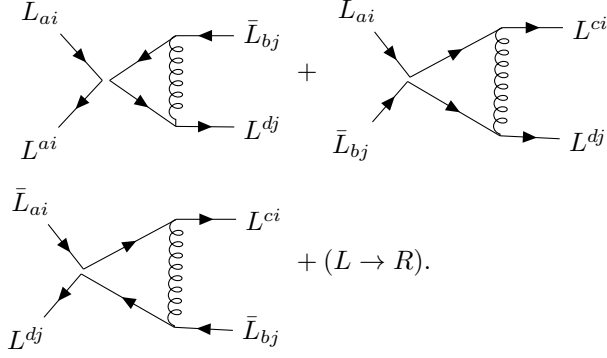
Three diagrams of the second type are proportional to  $g_V \alpha_g$  and contribute to the beta functions of  $G_V$  and  $G_{V_2}$ :



The first and third evaluate to 0 and the second is evaluated as

$$-\frac{3}{N_c} \frac{G_V g^2}{8\pi^2 \Lambda^2} \mathcal{O}_V + 3 \frac{G_V g^2}{8\pi^2 \Lambda^2} \mathcal{O}_{V_2}.$$

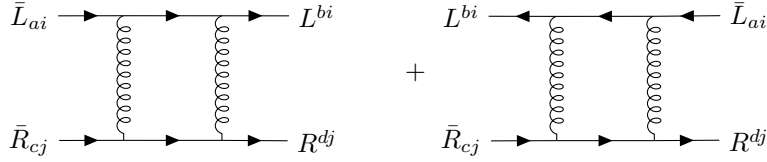
Three diagrams of the second type are proportional to  $g_{V_2} \alpha_g$  and contribute to the beta functions of  $G_V$  and  $G_{V_2}$ :



The first and third evaluate to 0, while the second is evaluated as

$$-\frac{3}{N_c} \frac{G_{V_2} g^2}{8\pi^2 \Lambda^2} \mathcal{O}_{V_2} + 3 \frac{G_{V_2} g^2}{8\pi^2 \Lambda^2} \mathcal{O}_V.$$

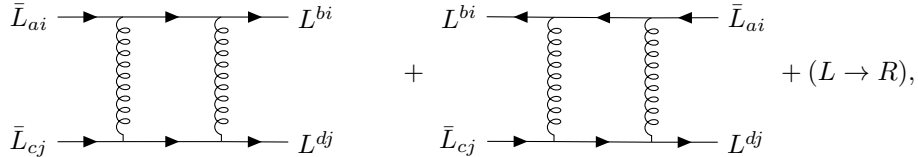
Furthermore, the third type of correction is proportional to  $\alpha_g^2$  and consists of 2 diagrams contributing to the beta functions of  $G_S$  and  $G_{V_1}$ :



which are evaluated as

$$\begin{aligned} & \frac{3}{16} \frac{2}{N_c} \frac{g^4}{8\pi^2 \Lambda^2} \mathcal{O}_S + \frac{3}{32} \left(1 + \frac{1}{N_c^2}\right) \frac{g^4}{8\pi^2 \Lambda^2} \mathcal{O}_{V_1}, \\ & -\frac{9}{16} \left(N_c - \frac{2}{N_c}\right) \frac{g^4}{8\pi^2 \Lambda^2} \mathcal{O}_S + \frac{9}{32} \frac{1}{N_c^2} \frac{g^4}{8\pi^2 \Lambda^2} \mathcal{O}_{V_1}. \end{aligned}$$

and two contributing to the beta functions of  $G_V$  and  $G_{V_2}$ :



which are evaluated as

$$\begin{aligned} & \frac{9}{32} \frac{2}{N_c} \frac{g^4}{8\pi^2 \Lambda^2} \mathcal{O}_V - \frac{9}{32} \left(1 + \frac{1}{N_c^2}\right) \frac{g^4}{8\pi^2 \Lambda^2} \mathcal{O}_{V_2}, \\ & -\frac{3}{32} \left(N_c - \frac{2}{N_c}\right) \frac{g^4}{8\pi^2 \Lambda^2} \mathcal{O}_V - \frac{3}{32} \frac{1}{N_c^2} \frac{g^4}{8\pi^2 \Lambda^2} \mathcal{O}_{V_2}. \end{aligned}$$

## D Beta Functions in a Model with a Yukawa Coupling

When the scalar terms (3.2) are added to the model (2.3), the system of beta functions is changed. As a consequence, new Feynman rules are added:

$$\begin{aligned} \Phi_k^l \text{ --- } \Phi_i^j &\sim \frac{\delta_{ik}\delta^{jl}}{q^2}, \\ \begin{array}{c} \Phi_j^i \\ \downarrow q \\ \begin{array}{ccc} p_1 \nearrow & & \nwarrow p_2 \\ \bar{L}_i & & R^j \end{array} \end{array} &\sim y\delta(p_1 - p_2 + q)\bar{L}_i\Phi_j^iR^j, \\ \begin{array}{c} \Phi_j^i \\ \downarrow q \\ \begin{array}{ccc} p_1 \nearrow & & \nwarrow p_2 \\ \bar{R}_i & & L^j \end{array} \end{array} &\sim y\delta(p_1 - p_2 + q)\bar{R}_i\Phi_j^iL^j, \end{aligned}$$

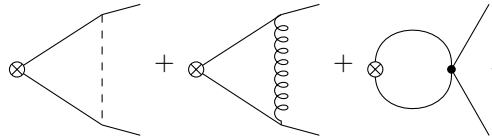
First, we consider the function  $\beta_{\alpha_g}$ . Due to the addition of the scalar field terms, the two loop beta function for  $\beta_{\alpha_g}$  is changed to [39]

$$\beta_g^{[2]} \equiv \Lambda \frac{d\alpha_g}{d\Lambda} = -2b_0\alpha_g^2 - 2b_1\alpha_g^3 - 2N_f^2\alpha_y\alpha_g^2.$$

The additional terms due to the four-fermion interactions can then be added as was done in appendix B. The beta function  $\beta_{\alpha_y}$  is given by [40]

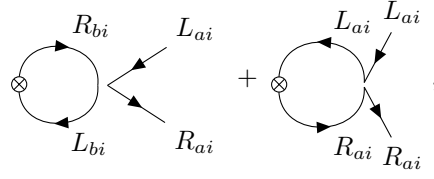
$$\Lambda \frac{d\alpha_y}{d\Lambda} = 2\alpha_y (\gamma_\phi + \gamma_{\bar{\psi}\psi}).$$

The anomalous dimension of the scalar field is given by  $2N_c\alpha_y$  [39]. Using the four-fermi interactions, one can find a non-perturbative approximation to the anomalous dimension of the mass of the fermion field [31] such that we get three contributing diagrams



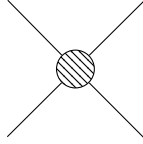
The first two diagrams contribute  $N_f\alpha_y$  and  $-6\frac{N_c^2-1}{2N_c}\alpha_g$ , and two diagrams can be found that give a contribution to the second diagram:



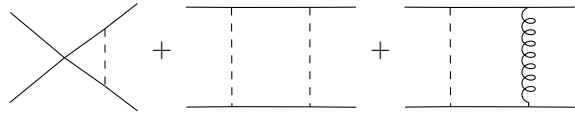


which contribute  $-2N_c g_S$  and  $8g_{V_1}$ .

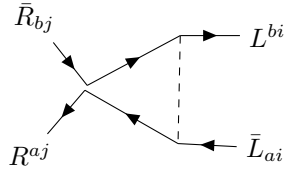
Next, we consider the beta functions for the four-fermi interactions, which are a slight variation of the ones found for the model without scalars in appendix C. The anomalous dimension of the fermion fields is changed due to the presence of the scalar fields to  $\eta = \alpha_y$  [31]. Furthermore, we find additional contributions to



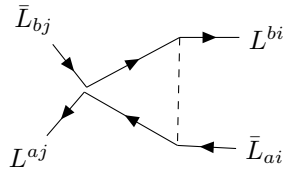
represented by three types of diagrams



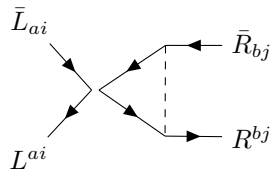
Diagrams represented by the third type all evaluate to 0. For the first type we find four diagrams that each contribute to one of the beta functions of the four-fermi interactions:



contributing  $4g_V \alpha_y$  to  $\beta_{g_S}$ ;

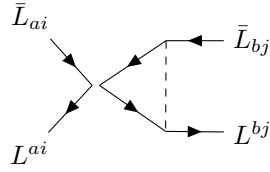


contributing  $g_S \alpha_y$  to  $\beta_{g_V}$ ;



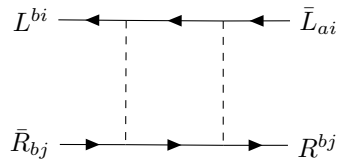
---

contributing  $-2g_{V_2}\alpha_y$  to  $\beta_{g_{V_1}}$  and

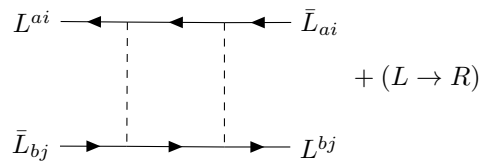


contributing  $-2g_{V_1}\alpha_y$  to  $\beta_{g_{V_2}}$ .

Furthermore, for the second type there are 2 contributing diagrams:



contributing  $2\alpha_y^2$  to  $\beta_{g_{V_1}}$  and



contributing  $2\alpha_y^2$  to  $\beta_{g_{V_2}}$ .

---

## References

- [1] E.C.G. Stueckelberg, A. Petermann, *The renormalization group in quantum theory*, Helv. Phys. Acta **24**, 317-319 - 1951.
- [2] K. G. Wilson, *Renormalization Group and Critical Phenomena. I. Renormalization group and the Kadanoff Scaling Picture*, Phys. Rev. **B4**, 3174 - 1971.
- [3] K.G. Wilson, J. Kogut, *The renormalization group and the  $\epsilon$ -expansion*, Phys. Rep. **12**, 77 - 1974.
- [4] C. Bagnuls, C. Bervillier, *Exact Renormalization Group Equations. An Introductory Review*, arXiv:hep-th/0002034v2 - 2001.
- [5] R. Percacci, *An ERGE primer*, <http://www.percacci.it/roberto/physics/as/erge.html>, retrieved: Oct. 2017.
- [6] C. Wetterich, *Exact evolution equation for the effective potential*, Phys. Lett. **B301**, 90 - 1993.
- [7] M. Brin, G. Stuck, *Introduction to Dynamical Systems*, Cambridge University Press, 1st ed. - 2002.
- [8] T. Morris, *Elements of the Continuous Renormalization Group*, Prog. Theor. Phys. Suppl. **131**, 395 - 1998.
- [9] Y.A. Kuznetsov, *Elements of Applied Bifurcation Theory*, Springer, 3rd ed. - 2004.
- [10] W. Govaerts, et al., *New features of the software MatCont for bifurcation analysis of dynamical systems*, MCMDS, Vol. 14, No. 2, pp 147-175 - 2008.
- [11] K.V.I. Saputra, L. van Veen, G.R.W. Quispel, *The Saddle-Node-Transcritical Bifurcation in a Population Model with Constant Rate Harvesting*, arXiv:1002.4150v1 - 2010.
- [12] E.M. Izhikevich, [http://www.scholarpedia.org/article/Saddle-node\\_bifurcation](http://www.scholarpedia.org/article/Saddle-node_bifurcation), retrieved: 03/04/2018.
- [13] Y.A. Kuznetsov, [http://www.scholarpedia.org/article/Adronov-Hopf\\_bifurcation](http://www.scholarpedia.org/article/Adronov-Hopf_bifurcation), retrieved: 15/06/2018.
- [14] W. Lacarbonara, *Nonlinear Structural Mechanics. Theory, Dynamical Phenomena and Modeling*, Springer, 1st ed. - 2013.
- [15] Y.A. Kuznetsov, [http://www.scholarpedia.org/article/Cusp\\_bifurcation](http://www.scholarpedia.org/article/Cusp_bifurcation), retrieved: 03/04/2018.
- [16] S. Gukov, *RG Flows and Bifurcations*, Nucl. Phys. **B919**, 583 - 2017.
- [17] K. G. Wilson, *Renormalization Group and Strong Interactions*, Phys. Rev. **D3**, 1818 - 1971.
- [18] S.D. Glazek, K.G. Wilson, *Renormalization of overlapping transverse divergences in a model light-front Hamiltonian*, Phys. Rev. **D47**, 4657 - 1993.
- [19] P.F. Bedaque, H.W. Hammer, U. Kolck, *Effective Theory of the Triton*, arXiv:nucl-th/9906032v4 - 2000.
- [20] A. LeClair, J.M. Roman, G. Sierra, *Log-periodic behavior of finite size effects in field theories with RG limit cycles*, arXiv:hep-th/0312141v1 - 2003.
- [21] E. Kiritsis, F. Nitti, L. Silva Pimenta, *Exotic RG Flows from Holography*, arXiv:1611.05493v1 - 2016.

- 
- [22] A. Morozov, A.J. Niemi, *Can Renormalization Group Flow End in a Big Mess*, arXiv:hep-th/0304178v2 - 2003.
- [23] B. Berche, E. Medina, *Classical Yang-Mills theory in condensed matter physics*, Eur. J. Phys. **34**, 161 - 2013.
- [24] A. Abbott, *CERN claims first experimental creation of quark-gluon plasma*, Nature **403**, 581 - 2000.
- [25] S. Gottlieb, *Lattice calculations of the quark-gluon plasma*, J. Phys.: Conf. Ser. **78**, 012023 - 2007.
- [26] T. Banks, A. Zaks, *On the phase structure of vector-like gauge theories with massless fermions*, Nucl. Phys. **B196**, 189 - 1982.
- [27] J. Braun, C.S. Fisher, H. Gies, *Beyond Miransky Scaling*, Phys. Rev. **D84**, 034045 - 2011.
- [28] T. Alho et al., *On finite-temperature holographic QCD in the Veneziano limit*, arXiv:1210.4516v1 - 2012.
- [29] M. Jarvinen, *Holography and the conformal window in the Veneziano limit*, arXiv:1508.00685v1 - 2015.
- [30] D.B. Kaplan, J.W. Lee, D.T. Son, *Conformality lost*, Phys. Rev. **D80**, 125005 - 2009.
- [31] H. Terao, A. Tsuchiya, *Conformal dynamics in gauge theories via non-perturbative renormalization group*, arXiv:hep-ph/0704.3659v2 - 2007.
- [32] Y. Kusafuka, H. Terao, *Fixed point merger in the  $SU(N)$  gauge beta functions*, Phys. Rev. **D84**, 125006 - 2011.
- [33] T. Appelquist, G.T. Fleming, E.T. Neil, *Lattice Study of the Conformal Window in QCD-like Theories*, Phys. Rev. Lett. **100**, 171607 - 2008.
- [34] T. Appelquist, J. Terning, L.C.R. Wijerwardhana, *The Zero Temperature Chiral Phase Transition in  $SU(N)$  Gauge Theories*, Phys. Rev. Lett. **77**, 1214 - 1996.
- [35] J. Ellis, *TikZ-Feynman: Feynman diagrams with TikZ*, arXiv:hep-th/1601.05437v1 - 2016.
- [36] W.E. Caswell, *Asymptotic Behavior of Non-Abelian Gauge Theories to Two-Loop Order*, Phys. Rev. Lett. **33**, 244 - 1974.
- [37] H. Gies, J. Jaeckel, C. Wetterich, *Towards a renormalizable standard model without a fundamental Higgs scalar*, Phys. Rev. **D69**, 105008 - 2004.
- [38] K.I. Aoki et al., *Analysis of the Wilsonian effective potentials in dynamical chiral symmetry breaking*, Phys. Rev. **D61**, 045008 - 2000.
- [39] M.E. Machacek, M.T. Vaughn, *Two-Loop Renormalization Group Equations in a General Quantum Field Theory I. Wave function renormalization*, Nucl. Phys. **B222**, 83 - 1983.
- [40] M.E. Machacek, M.T. Vaughn, *Two-Loop Renormalization Group Equations in a General Quantum Field Theory II. Yukawa couplings*, Nucl. Phys. **B236**, 221 - 1984.